

# ALMA MATER STUDIORUM UNIVERSITÀ DI BOLOGNA

---

---

**DOTTORATO DI RICERCA IN INGEGNERIA  
ELETTRONICA, TELECOMUNICAZIONI E  
TECNOLOGIE DELL'INFORMAZIONE**

**CICLO XXXIII**

Settore concorsuale di afferenza: 09/E3  
Settore scientifico disciplinare: ING-INF/01

## **Energy Autonomous RF Tags for Sensing and UWB Localization Applications**

**Presentata da: Davide Fabbri**

**Coordinatore**

Prof.ssa Alessandra Costanzo

**Supervisore**

Prof. Aldo Romani

Esame finale anno 2021

*This page intentionally left blank.*

*A Giada, futura moglie*

*This page intentionally left blank.*

# Acknowledgements

Part of the activities reported in this thesis have received support from the European Union's Horizon 2020 research and innovation programme under grant agreement No 730957 (ENABLES), from the ECSEL Joint Undertaking (JU) through EU H2020 program and Italy, Germany, The Netherlands, Spain, and Slovakia under Grant Agreement no. 737434 (CONNECT), and from European Space Agency (ESA) under contract number ESA AO 1-8471/15/NL/LvH.

I would like to express my gratitude to my supervisor Prof. Aldo Romani who gave me the possibility to undertake the PhD programme. I appreciate his multidisciplinary scientific experience and constant support to my research activities.

A special thanks to Prof. Davide Dardari, Prof. Alessandra Costanzo and Prof. Diego Masotti for involving me in a "dream team" able to end, with great satisfaction, the ESA-LOST project through the success of a strong collaboration.

*This page intentionally left blank.*

## **Keywords:**

Energy harvesting

Wake-up Radio

RFID

Sensing

UWB localization

*This page intentionally left blank.*

# Abstract

In the new scenarios foreseen by the Internet of Things (IoT), billions of smart devices are worldwide spread and connected to each other to provide sensing information or to detect and locate tagged items with high accuracy using cheap, energy autonomous, and disposable tags. In this context, the use of energy harvesting techniques to supply devices, nowadays, plays an important role in order to create energy autonomous systems able to reduce the use of batteries, by containing the infrastructure maintenance costs, for better environmental safeguard.

Hence, by considering real scenarios in which tags can be placed, where only few  $\mu\text{W}$  are available as input source, low-power design aspects, strategies and policies have to be taken into account during the implementation approach. In order to cover all possible solutions, radio-frequency and light energy harvesting sources are considered to build battery-less nodes.

Thus, PV passive tags for indoor and outdoor environments will be presented, which allows the creation of long range Wireless Sensor Networks (WSNs) used for environmental monitoring.

In harsh scenarios where the presence of obstacles makes energy scavenging operations more critical, radio-frequency sources can be adopted to build battery-less, individually addressable, UHF tags, featuring high-directive behaviour with single-monopole structures or an orientation-independent usage through double-monopole architectures. UWB circuitry for localization purposes will be introduced in both configurations: transmitting and backscattering tag solutions adopting, in the first case, a customized protocol for the UHF link, while in the second one, a RFID integration compliant with European standard, by making this activity more attractive for the market.

*This page intentionally left blank.*

# Contents

<b>Acknowledgements</b>	<b>v</b>
<b>Abstract</b>	<b>ix</b>
<b>1 Introduction</b>	<b>1</b>
1.1 Energy Harvesting for Internet of Things . . . . .	1
1.2 RF nodes classification . . . . .	3
1.3 Energy Autonomous tags for WSN . . . . .	6
1.3.1 UHF based systems . . . . .	7
1.3.2 PV based systems . . . . .	10
1.4 Radio-frequency Localization Systems . . . . .	10
1.4.1 Localization of UHF-RFID Tags . . . . .	12
1.4.2 Localization of UWB-RFID Tags . . . . .	13
1.5 Thesis outline . . . . .	15
<b>2 LP design strategies for UHF passive Tags</b>	<b>17</b>
2.1 UHF Energy Harvesting Front-End . . . . .	17
2.2 Wake-up Radio (WuR) . . . . .	20
2.2.1 Technology . . . . .	21
2.2.2 Frequency usage . . . . .	22
2.2.3 Address decoding . . . . .	22
2.2.4 Modulation techniques . . . . .	24
2.3 Power Management Unit . . . . .	24
2.3.1 Start-up circuit . . . . .	25
2.3.2 Main converter . . . . .	27
2.4 Low-power design strategies . . . . .	29
2.4.1 Duty-cycled operation mode . . . . .	29
2.4.2 Policies for power optimization . . . . .	31
<b>3 PV passive Tags for WSN</b>	<b>35</b>
3.1 Motivations . . . . .	35

3.2	PV Tags hardware architecture . . . . .	36
3.3	Node operation . . . . .	37
3.4	Load current consumption . . . . .	39
3.5	Multi-source PMU . . . . .	40
3.6	Single-source PMU . . . . .	42
3.7	Experimental results . . . . .	44
<b>4</b>	<b>UHF-UWB battery-less Tags for localization</b>	<b>47</b>
4.1	Motivations and Requirements . . . . .	47
4.2	Single monopole Tag design . . . . .	48
4.2.1	UHF front-end . . . . .	49
4.2.2	Tag operation . . . . .	51
4.2.3	Design Trade-off . . . . .	52
4.2.4	Power management unit . . . . .	53
4.2.5	PMU validation test . . . . .	55
4.2.6	Energy budget . . . . .	56
4.3	Orientation-independent Tag design . . . . .	59
4.3.1	Double-monopole rectenna . . . . .	60
4.4	Test bench for measurements . . . . .	62
4.5	Tags performance . . . . .	64
4.5.1	Single-monopole . . . . .	65
4.5.2	Double-monopole . . . . .	66
<b>5</b>	<b>Enhanced RFID with localization capabilities</b>	<b>69</b>
5.1	Motivations . . . . .	69
5.2	UHF-RFID tag implementation . . . . .	69
5.3	Digital base-band Tag operation . . . . .	70
5.4	Power management and Energy budget . . . . .	73
5.5	Tag performance . . . . .	76
5.5.1	Tag duty-cycle and charge time . . . . .	77
5.5.2	Read-rate and environmental sensing . . . . .	78
5.6	UWB-RFID Tag integration . . . . .	80
5.6.1	UWB-RFID backscattering tag design . . . . .	80
<b>6</b>	<b>Localization Results</b>	<b>85</b>
6.1	UHF-UWB transmitting Tag Application . . . . .	85
6.1.1	Signal processing . . . . .	87
6.1.2	Localization performance . . . . .	90
6.2	UWB-RFID backscattering Tag Application . . . . .	94
6.2.1	Basic concepts on signal processing . . . . .	95
6.2.2	Localization performance . . . . .	97

<i>CONTENTS</i>	xiii
<b>7 Conclusion and final remarks</b>	<b>101</b>
List of figures	103
Bibliografy	107



# Chapter 1

## Introduction

### 1.1 Energy Harvesting for Internet of Things

In the last two decades, Energy scavenging solutions have become more relevant, firstly in Research, and secondly in the industrial market. Basically, such kind of systems have the aim to collect, convert and store energy from ambient sources (solar, vibration, thermal, flow-based...) [1] or radio-frequency transmissions [2], in order to energetically sustain several low power applications such as sensing, security, medical and health care, objects localization etc [3][4]. The rapid growth of energy harvesters can be explained through the strong reduction of devices power dissipation, according to the Gene's law [5]. This trend is actually related to processors and memories which have been scaled, during the years [6], but it can be extended, although with lower trends, to all electronics devices. In particular, having smaller transistors require less charge to drive them, which means lower power consumption, besides faster transitions that speed up switching logic performances. On the other hand, the extracted power density from energy harvesters is increased year per year [7], by allowing to fully supply small devices with harvested energy (battery-less solutions), which was not possible in the past, Fig. 1.1. However, for all of those applications which can not be entirely sustained by environmental sources, the energy harvesting systems are useful for recharging batteries (battery-assisted systems). In some cases, batteries are still cheaper compared to energy harvesters (for instance MEMS devices, which require higher production costs) and their storage capability is greater than that of super-capacitors [8].

Fortunately, the worldwide attention on the environmental safeguard, combined with the rapid diffusion of smart Internet of Things (IoT) devices, played an important role on the Energy harvesting systems development. We have observed the birth of a global infrastructure for the information society, in support of decisions and control operations, which enables advanced services by interconnecting

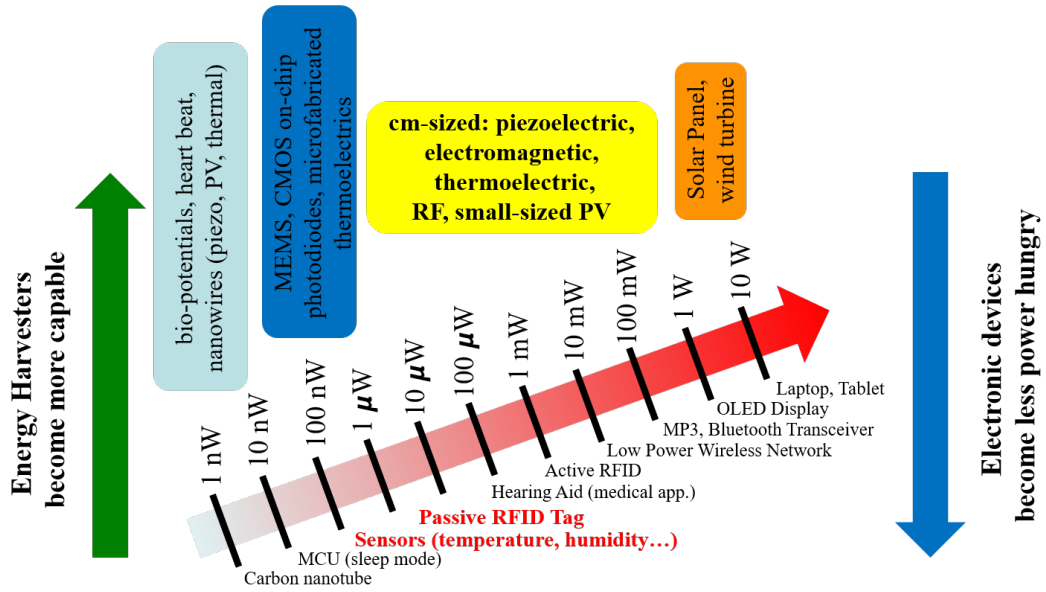


Figure 1.1: Electronic devices powered through Energy Harvesters.

things, based on existing and evolving communication technologies [9]. More than 30 billions IoT devices have already been spread all around the world and the yearly increment is still exponential [10]. Hence, the introduction of *Energy Autonomous Systems (EAS)* for batteries replacement, where it is possible, significantly contributes for decreasing the environmental pollution, reducing the human interventions and infrastructure maintenance costs.

As shown in Fig. 1.1, the solar source represents the most profitable energy harvesting solution which allows to have higher conversion/harvested power compared to other sources. Hence, many energy hungry applications can be supplied through Photo-Voltaic (PV) solar cells where the other available sources are not sufficient. However, a spontaneous light source is not under control and affected by weather condition having a strong impact on the system operation, while artificial light can provide an useful energy to supply continuously the devices.

It is understandable that, radio-frequency communications have a dominant role in the IoT, where objects talk to each other (*wireless Machine to Machine Communication (M2M)* [11]), make decision autonomously, share the information to the cloud and sense the environment in support of humans. This progress has justified the rapid increase of the number of smart devices connected to *Wireless Sensor Networks (WSNs)* whose purpose typically consists in monitoring and transmitting data related to sensed physical quantities. Since autonomous nodes are expected to operate in very dissimilar surroundings, with different energy sources and power densities, the importance of finding efficient ways to exploit available

energy is evident, as in many cases the power available from the environment is in the order of microwatts [1] or less. In this contest, as mentioned before, **PV energy harvesting** is a mature solution for the vast majority of applications. However, even **radio-frequency sources** [12][13] represent a fascinating solution where both environmental data information and energy scavenging can be delivered through the same energy transducer, by reducing the nodes hardware complexity and sizes.

## 1.2 RF nodes classification

In 1973, Mario W. Cardullo released a patent on radio-frequency tags with rewritable memory [14] followed by Charles Walton who presented a RF passive transponder used to unlock doors without keys [15]. These solutions have been declared as the first *Radio-frequency Identification Systems (RFID)* which had the aim to wirelessly identify and control objects, in Non-Line-of-Sight (NLOS) conditions where optical systems failed. RFID quickly became protagonist in the role of bar-code descendants, evolving in new applications and worldwide standardized solutions for a common language.

In order to classify radio-frequency tags the main technical aspects to be considered are related to *power transfer technique, frequency source and node power supply* [25]. The process so called *Wireless Power Transfer (WPT)* [16] is in charge of delivering electrical energy from the power source to the specific node, without using electrical cables. The WPT systems can be divided in three groups depending on the distance between tags and readers:

1. *near-field inductive or capacitive coupling (non radiative)* [17][18][19][20];
2. *far-field directive power beaming (radiative)* [21][22];
3. *far-field non directive power transfer (radiative)* [23][24].

The first approach refers to short range applications, by wirelessly charging devices such as recent mobile phones, by inductive coils. However, the required proximity between tags and readers, needs the presence of an operator to perform the power exchange. On the other side, radiative systems use electromagnetic waves for data and power transmissions, in order to extend the working distances. Within this technique, the far-field directive solution specifically generates power beams, where the transmitted radio-frequency is intentionally sent to the receiver nodes which collects energy from the incoming signal. Instead, far-field non directive exploits electromagnetic energy already present in the environment and generated

from sources not intended for energy harvesting purposes (for instance WiFi and Bluetooth).

The frequency ranges mainly used for WPT purposes are:

- **Low Frequency (LF):** This category operates in the 30 KHz to 300 KHz range [26] (RFID 125-135 kHz, standard ISO/IEC 18000-2 [27]), with a working distance of few centimeters (the node working principle is based on inductive coupling between tag and reader). Hence, this solution is suitable for short-range application (access control, livestock tracking...) in which a high wireless power transfer can be achieved. However, the data-rate for the information exchange is slower compared to other technologies, but due to the low frequency source, such kind of systems have better performances in presence of obstacles (metals, liquids...).
- **High Frequency (HF):** The HF band ranges from 3 MHz to 30 MHz [26], but most of the systems operate at 13.56 MHz [29] (working range up to 1 meter) in which the power transfer is still based on reader to tag inductive coupling. Within these frequencies is collocated the well known Near Field Communication (NFC) [28] commonly used for data exchange between devices or proximity card payment (smart cards) and security systems (ISO/IEC 15693 [30][31][32], ISO/IEC 14443 A, B [33][34][35][36])
- **Ultra-High Frequency (UHF):** The UHF frequency band covers the range from 300 MHz to 3 GHz and it is mainly used for longer range applications, of several meters, compared the solutions described previously. In this case, the communication link between tags and readers is performed through a radiative energy transfer, in the form of electromagnetic waves. Within the range offered by UHF systems, it worth to mention the following widely used working frequencies:
  - *UHF 433 MHz:* this frequency is mainly used for defense applications and allowed only for active tags solutions (ISO/IEC 18000-7 [37]), but not highly recommended for radio-frequency energy harvesting due to the maximum permitted transmission power of 10 mW [38].
  - *UHF 865.6-867.6 MHz (United States 902-928 MHz):* lower restrictions have been allowed for this particular frequency range. The RF transmission can be performed up to 2 W ERP (Europe) or 4 W ERP (US) [39]. Hence, the majority contributions regarding RF energy scavenging come from UHF band here presented, which is suitable for extended working range applications. Within this frequency band, the Auto-ID center, in 2003, developed two air interface protocol (Class 0 and Class 1), the *Electronic Product Code* numbering scheme used for tag identification

and a new architecture for looking up data associated on an RFID tag on the Internet. The technology was licensed and worldwide formalized, through the *EPCGlobal* organization, which is in charge to innovate and develop industry-driven standards to support the use of RFID, allowing a global visibility. By following this purpose, the EPC Generation 2 Class 1 [40] has been released, which contains all information for building interrogators and tags, compliant with the standard.

- *UHF 2.4 GHz*: represents the most common solution for several applications and technologies such as WiFi and Bluetooth, where the main purpose is the consumer data exchange. For this reason, the band is very congested and unfortunately, the regulations have limited the maximum transmitted power to 100 mW [41] by restricting long range applications through radio-frequency energy harvesting, even if in this case, the antennas have smaller dimensions compared to lower frequencies, allowing a miniaturization process of the nodes. RFID rules for readers and tags can be found in ISO/IEC 18000-4 [42]) standard.

As it is possible to notice, all the working frequencies are regulated through European and US standards, which defines not only the allowed emitted power, but also the communication protocols between tags and readers, which have to be followed in order to perform the data exchange, compliant with the rules. The nodes can also be classified according to the power source and defined as:

- **Passive:** All the energy used by the system is harvested from the ambient input source and made available for the load (Energy autonomous node) [43].
- **Semi-Active:** some components of the node (such as encoding, decoding, processing, memories...) require continuous power provided from an external source (battery). Instead, the RF front-end is totally passive and the incoming signal can be used for battery recharging and communications purposes [43].
- **Active:** all the circuits implemented receive a continuous external power supply using battery. The main objective is to increase the tag sensitivity for longer operational range by adopting circuits with an higher power consumption [44][45].

### 1.3 Energy Autonomous tags for WSN

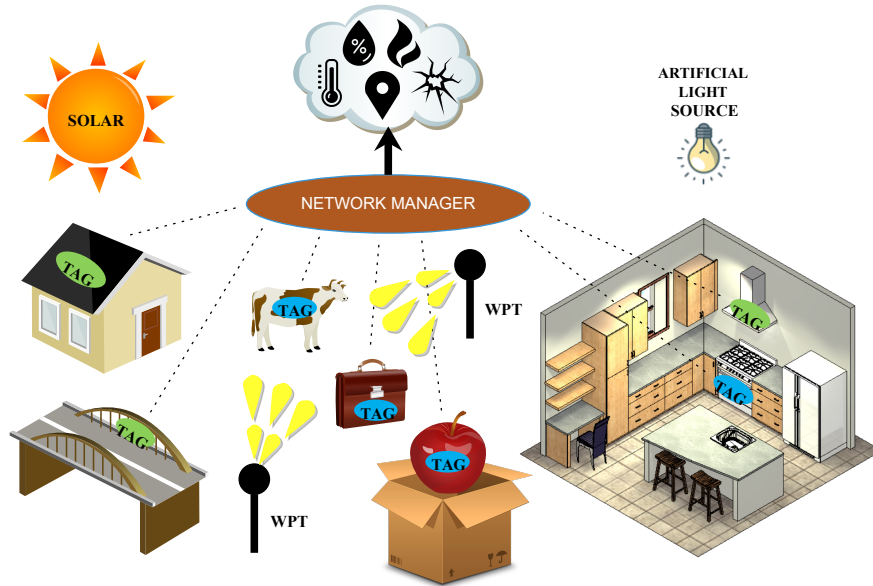


Figure 1.2: General scenario of Radio-Frequency and Ambient Light Energy Autonomous systems.

The thesis work is focused on battery-less tags for Wireless Sensor and Localization Networks using *UHF-868 MHz WPT source*, which represents the most common choice for what regards radio-frequency energy harvesting systems (in part due to the relaxed power emission constraints) and *light sources* as additional solution for all of those applications where it can be easily exploited.

By considering the scenario depicted in Fig. 1.2, UHF based autonomous systems performs the WPT through radio-frequency *energy showers* and the nodes are placed in contact with objects to be monitored, typically working in non-line-of-sight conditions respect to the energy source. Instead, the ambient light energy harvesting, can be computed through solar energy or artificial light emissions for outdoor and indoor solutions. The type of Sensors information depends on the applications (generally temperature, humidity, harmful gases, structural health monitoring for failures...) which can be integrated with the nodes localization, for knowing the correct position where the data have been sent, specially when objects move without a fixed position. Depending on the source availability, for a given type of application, it can be more convenient to use the solar energy, for ultra-exposed outdoor objects monitoring such as sensor nodes (green tags) placed on bridges or buildings. However, in the case of dynamic objects, partially covered

by shaded areas or in the worst case closed in non-metal boxes (goods and livestock tracking, food monitoring...), radio-frequency sources can be easier managed due to the properties of such kind of signals fully working in harsh conditions. As expected by WSN systems, all monitored physical quantities are acquired by the *network manager* and subsequently stored into the *Cloud* for worldwide accessibility.

It is worth to mention that, the energy sources here presented are considered as main contributors for energy autonomous system development, but they can be supported by other sources such as *vibrational* and *thermoelectric* by creating multi-source tags for better energy harvesting performances.

### 1.3.1 UHF based systems

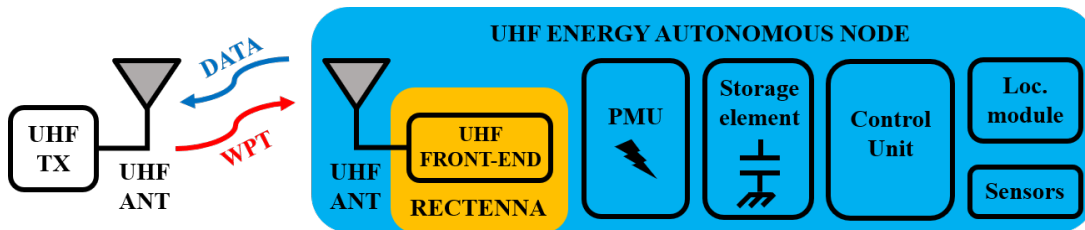


Figure 1.3: Typical hardware architecture of RF Energy Autonomous nodes.

The tag hardware architecture, Fig. 1.3, is based on a *Rectifying Antenna (Rectenna)* which has to manage the incoming UHF signal (RF to DC conversion) used for energy harvesting. Moreover, the reader to tag communication and viceversa besides the sensing data transmission, can be executed with the same antenna, without introducing additional elements. The voltage output of the Rectenna is boosted by a *Power Management Unit (PMU)* up to the voltage levels required by the load. The total amount of energy scavenged is stored in supercapacitors before being available to supply the *Digital Control Unit* which manages the presence of sensors and/or localization modules for not energy-intensive tasks.

The imposed limitation on the UHF emitted power, causing very low voltage (in the order of few hundreds mV) and poor received power levels (few  $\mu W$ ) as the distance from the source increases to several meters. As a matter of fact, the most prohibitive obstacle to the diffusion of RF harvesting nodes is the lack of dedicated power converters able to operate under these conditions. However, simply developing specific power converters or designing more efficient *rectennas* is not sufficient: power management must observe not only obvious requirements in terms of ultra-low power, but also specific policies for adjusting the behavior of the node according to the availability of energy. Active interaction between the power and control modules is integral to achieving this target. Another important aspect

that reinforces the need for such interaction, is the considerable difference between the power profiles of the harvesting source and power required by the smart node; while the former can be considered constant or slowly changeable, the latter is characterized by short peaks consumption, followed by long inactive periods. This mismatch requires a careful sizing of the storage elements, considered as an integral part of optimization policies.

### **State of the Art on Radio-frequency EAS**

J. R. Smith et al [46], in 2005, were the pioneers in passive RFID tags extended with sensing capabilities. They reported the first use of ID modulation to embed environmental information within the EPC standard. The Wireless Identification and Sensing Platform (WISP), built with off-the-shelf component, was improved by P. Sample et al. in 2007 [47] and 2008 [48], by developing the first low-cost battery-free programmable UHF-RFID node with sensors, where the EPC Gen 2 Class 1 protocol is firmware implemented in a microcontroller by making the platform flexible and easily expandable. WISP was able to work up to 4.5 meters from the RF source, using only a single dipole antenna. Starting from these results, in the following years, several contributions in the research field achieved almost the same performances in terms of working distance [49][50]. In 2014, D. De Donno et al [51], presented a RFID augmented module for smart environmental sensing (RAMSES), using the findings of the WISP project, with an improved read-range. The node implements two separated UHF antennas, for RF energy harvesting purposes and wireless sensor data communication, through RFID standard. The system is able to operate up to 10 meters, in a battery-less solution, while the read range is extended to 22 meters, in a battery-assisted configuration. On the other hand, as limitation, the usage of two different antennas makes the prototype expensive in terms of occupied area and the RFID protocol implementation, by an integrated solution ( Monza X-2K [52]), has lower flexibility compared to the firmware one.

Within the PhD activities, a newest micro-power design of UHF battery-free node has been presented in 2018 [53] which fully operates up to 10.80 m with a single monopole antenna. Subsequently, the circuit has been integrated with EPC Gen 2 standard in 2019, through a microcontroller based flexible platform by maintaining the same working distances [54]. The performances of these solutions are affected by the tag orientation with respect to the transmitter, due to the presence of a single linearly-polarized antenna. For this reason, a multi-element antenna was designed in 2019 [55] to facilitate the increase of working distances, for all possible tag orientations and positions, improving the node communication stability and the energy harvesting chain. The base-band circuits designed in [53] has been integrated with a multi-element antenna [55], specifically developed

to overcome issues related to the tag orientations, besides improving the system stability and the rectifier available power for wider working distances up to 22 meters in a battery-free configuration. Moreover, The use of hardware/software policies, as done in [56], can reduce significantly the power consumption of the node, for even longer ranges.

Furthermore, in addition to research activities, many industries are working on integrated UHF-RFID sensory tag solutions. In particular, the most important are *SL900A* chip tag by *Austria Micro System (AMS)* [57], *Easy2Log* tag by *CAEN RFID* [58] and *EVAL01-Fenix-RM* by *Farsens* [59]. However, these solutions present short working distances of few meters, as main drawback. Many flexible solutions are available on the market such as *SPS1M002* by *On Semiconductor* [60], the sensor node *DogBone* by *Smartrac* [61] and others [62]. Several RFID ICs with sensing capabilities have been presented over the years, starting from the work done by Namjun Cho in 2005 [63], who developed one of the first RF passive transponder with an embedded temperature sensor. *RF Micron* have provided a single chip solution called *Magnus S* [64] with sensing capabilities for multiple stimuli such as moisture, temperature, and positioning. One of the most recent company, *Asygn*, came out in 2018 with the products *AS321X series* [65] which implements temperature, ambient light, strain and current sensors. This is the proof that the market is headed towards a full RFID protocol integration with useful commercial applications (as sensing [66][67] and localization [68]). In the literature, both features combined with energy scavenging circuits can not be easily found in a single-chip solution. However, in 2018, it has been designed a new architecture of battery-less CMOS micro-power sensor tag, embedding RF energy harvesting capabilities, a temperature sensor, a generic capacitive sensing interface and a localization sub-system [69]. Such high integration level allows the development of small size nodes, in which all the electronic is represented by one dot. This important achievement facilitates the use of flexible and green materials such as paper [70] and textile [71][72] adopted as tag substrate.

Complementarily, the thesis work aims at demonstrating the feasibility of energy autonomous tags with sensing, identification and localization capabilities based on an optimized design involving off-the-shelf components. More specifically, it will be shown how specific design optimizations grant performances similar to state-of-the-art integrated tags. The use of standard components allows for cost effective and customizable solutions, still in a reasonably small footprint.

### 1.3.2 PV based systems

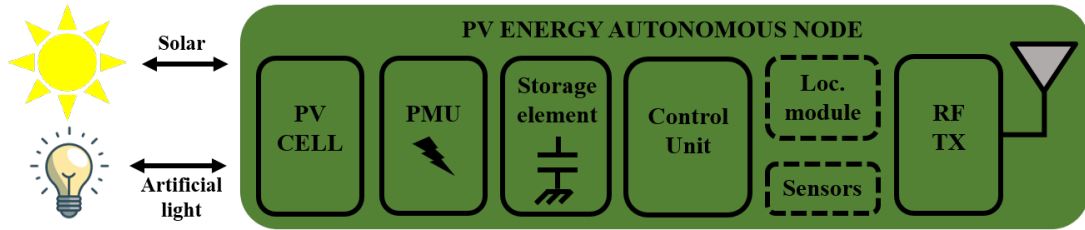


Figure 1.4: Typical hardware architecture of PV Energy Autonomous nodes.

An Ambient light Autonomous node, Fig. 1.4, collects energy from solar source or available artificial lights, through *photoelectric transducers*. They are composed of semiconductor materials or devices, which eject electrons from the photosensitive surface when they are irradiated by the light source. In particular, they can be divided in (i) passive transducers: *photo-emissive*, *photo-conductive* and (ii) active transducer: photo-voltaic cells. PV transducers, combined in a multi-cell configuration, permit to have greater amount of power compared to the other devices, by making this solution an attractive choice for powering smart nodes. Compared to UHF sources, which are based on modulated sinusoidal waveform, the output of a PV cell is represented by a DC voltage ready to be processed through a DC/DC boost converter as power management unit. Moreover, the digital voltage levels available from the photo-electric transducer are typically higher and not as critical as UHF Energy harvesting, allowing to have more relaxed design constraints in terms of low power consumption. Since the tag is intended for wireless sensor networks, a radio-frequency transceiver is placed to deliver sensing data information to receivers, as the input source can not accomplish such required function.

## 1.4 Radio-frequency Localization Systems

The capability to localize in real-time with high-accuracy (a few centimeters) tags pervading the environment would enable unexplored context-aware applications and huge market perspectives, such as in the field of item searching/sorting in logistics, warehouse or shopping mall scenarios. It is possible to envision that in the near future every object will be tagged to be part of augmented reality applications [73], which allow virtual imagery to exactly overlay physical objects in real-time [74]. These perspectives highlight the main limitations in terms of localization accuracy and reliability of actual HF and UHF-RFID technologies, which were initially conceived only for objects identification purposes at larger distances. Even though such limitations have been in part overcome through the

introduction of significant improvements in current standards, it is clear that the above-mentioned requirements cannot be completely fulfilled by the current first- and second-generation RFID.

Regarding high-accuracy localization, the best positioning accuracy, in the order of 10-20 cm, is currently offered by real-time locating systems (RTLS) adopting the impulse radio ultra-wideband (UWB) technology [75]. In fact, the transmission of pulses, with duration in the order of a few nanoseconds, guarantees high localization accuracy thanks to accurate measurements of the signal propagation time and the capability to easily discriminate multi-path components, thus making UWB well suited for hard indoor propagation environments characterized by strong reflections. Unfortunately, all available standards (e.g., IEEE 802.15.4a [76] or 802.15.4f [77]) and commercial solutions are uniquely based on active tags (i.e., equipped with battery and power-hungry transmitters), and not energy-autonomous in power-constrained scenarios. Hence, one of the aim of this thesis is to show the feasibility of UWB battery-less transmitting tags based on energy-efficient UWB transmitters [78] suitable for energy autonomous solutions. Moreover, in order to guarantee high-accuracy localization along with even lower power consumption, an interesting idea is to fuse the advantages of RTLS and RFID. An example is given by the merging of the UWB technology, so far only exploited in active RTLS systems, with the backscatter modulation principle, which is the basis of UHF-RFID [79].

Battery-less tags make the design of such systems very challenging, because of important link budget limitations and of strong constraints in energy availability, thus calling for extremely low-power consumption electronics and dedicated signal protocols. Thus the maximum range of wirelessly powered UWB-RFID tags is critically related to the tag rectifier sensitivity, that is the minimum received power to achieve targeted output voltage, together with the signal-to-noise ratio (SNR) achieved by the tag itself. The communication between the tag and the reference nodes should be performed by modulating the scattering response of the tag to the interrogation signal, which is based on a proper variation in time of the antenna load. The network of readers is coordinated by a central unit, whose purpose is to collect all position-dependent measurements and compute an estimate of the tag's positions.

The accurate localization of passive RF tags placed on objects, in indoor environments, is a challenging issue, mainly because of the effects of multi-path propagation and non-line-of-sight channel conditions. In radio positioning systems, the accuracy in the tag's position estimation mainly depends on: (i) the type and quality of the position-dependent measurements from radio signals, exchanged between tags and reference nodes (ii) the number of available measurements related to the number of reference nodes/antennas and (iii) the geometric configuration of involved nodes (reference and tags), which affects the geometric dilution of precision

(GDOP) [80][81]. Position-dependent measurements can target different kinds of figures of merit such as: the received signal strength (RSS), signal time-of-arrival (TOA) or time-difference-of-arrival (TDOA), signal angle-of-arrival (AOA), signal phase difference. In cluttered environments, such as indoor scenarios, methods based on time/angle/phase measurements can provide, in principle, higher accuracy than RSS based measurements. Moreover, a further distinction can be made on the basis of the use of narrow- or wide-band signals: in the first case, angle/phase measurements take advantage of the high SNR, but might suffer from deep fading (multi-path) or phase ambiguity; in the second-case, especially if UWB signals are involved, time-measurements (e.g., TOA/TDOA) are sufficient to extract all the necessary position/angle/distance information from the received signals. In such a case, the standard deviation of time measurement error is proportional to the inverse of the signal bandwidth and the square root of the SNR: this leads potentially to centimeter-level accuracy. Moreover, the large bandwidth allows to resolve multi-path components, thus making the performance less sensitive to fading caused by indoor environments [75].

### 1.4.1 Localization of UHF-RFID Tags

Even though Gen.2 RFID was not conceived for positioning, localization information can be obtained by exploiting one or a mix of the following signal features: Received Signal Strength Indicator (RSSI) (Fig. 1.5(a)), carrier phase (Fig. 1.5(b)), and AOA (Fig. 1.5(c)) [82].

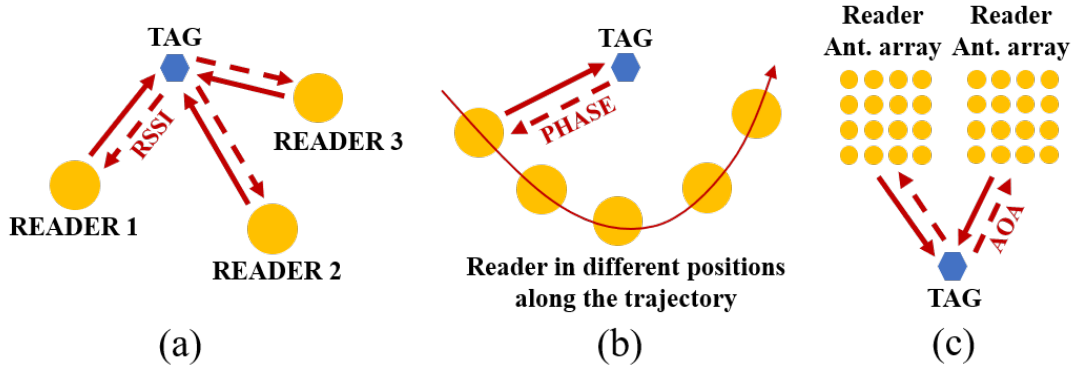


Figure 1.5: Localization techniques for UHF-RFID tags.

RSSI-based solutions rely on the fact that, in ideal conditions, the larger the distance of the tag the smaller is the received power, so multiple RSSI measurements can be combined to infer ranges and, hence, to obtain position information. Despite its simplicity, this method is very sensitive to random signal fluctuations caused by

multi-path that can lower the correlation between RSSI and distance, and thus, decrease the position estimation accuracy by making it extremely unreliable, even if some improvements of the localization accuracy have been obtained [45]. Scherhäufl et al. [83] present a combined RSSI and phase-of-arrival based localization, achieving 2 cm accuracy using 8 standard RFID readers. This is a good solution for certain applications, but its limitations include small area of operation and no capability of localizing multiple tags. Fig. 1.5(b) shows the case in which the reader collects several carrier phase measurements, from different locations, as response of an intended fixed tag. As extension to the phase difference-of-arrival technique, synthetic aperture radar (SAR) methods with a moving antenna can be utilized to take numerous phase measurements. The antenna trajectory must be known with high precision. With this approach both standard and non-standard RFID tags can be localized with a precision of a few cm at short distances ( $< 5$  meters) and in strong LOS conditions [84][85]. These methods offer suitable accuracy in controlled and specific scenarios, but suffer important multi-path and ambiguity issues due to phase periodicity. Consequently, they perform well only in controlled environments with scarce multi-path (strong LOS) and in the presence of some a-priori information on tag position (e.g., pre-determined trajectories) [86][87][88][89]. Other approaches based on multi-tone signaling can be found in [90] and [91]. Precise signal AOA measurements can be obtained using antenna arrays with sufficiently narrow beams (Fig. 1.5(c)). By combining at least 2 AOA measurements or one AOA and one range measurement, it is possible to determine the position of the tag. To achieve high angle resolutions, AOA schemes require large antenna arrays to realize narrow beams with consequent large dimension of readers and high cost of the infrastructure [92]. Accurate AOA estimation requires strong LOS conditions to work properly. In fact, angular errors of the order of two degrees have been reported [93], but in strong multi-path channels, non-relevant directions are often obtained. Spatial smoothing techniques may allow to distinguish the paths of several coherent signals, but this is very difficult to implement in the case of 2D arrays of non-regularly spaced elements [94]. A reduction of errors may be obtained through the use of redundant systems, but the arrays then become quite cumbersome and may not fit in small rooms, in which the issue of multi-path is the most problematic.

### 1.4.2 Localization of UWB-RFID Tags

Summarizing, while rough localization precision can be obtained with current RFID technology, centimeter-level accuracy in harsh environments, with passive tags, requires a technology shift toward signals with extremely large bandwidth. Owing to fine temporal resolution of transmitted signals, UWB-based systems are capable of high ranging accuracy and robustness against multi-path propagation. Given the aforementioned potentialities, the joint use of RFID and UWB technologies

represents a very appealing solution to fuse the advantages of RTLS and RFID.

The envisaged scenario, Fig. 1.6, is composed of: (i) reference nodes, with the dual role of transmitting or receiving UWB signals, which are placed in fixed positions; (ii) RF tags, attached to objects (fixed or slowly moving), are equipped with a rectifying UHF antenna (rectenna) combined with UWB antenna for localization purposes. (iii) Readers, acting as UHF energy providers, i.e., “RF energy showers”, to wirelessly energize the tags.

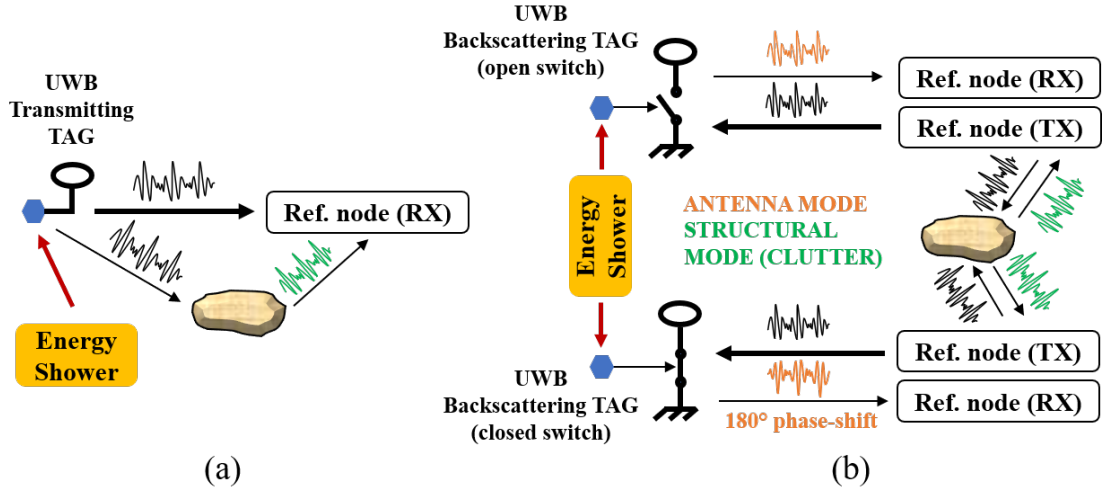


Figure 1.6: UWB tag implementation based on (a) transmitting and (b) backscattering techniques.

Systems proposed so far generally fall into two categories that differ in the tag implementation based on *transmitting tags* (Fig. 1.6(a)) and *backscattering tags* (Fig. 1.6(b)). In the active tag case, the UWB link budget is less critical, due to the fact that the signal only needs to travel one-way, which permits to increase significantly the working distance between tag and readers. On the other hand, in order to achieve this result, the UWB signal is generated directly on the tag side, by increasing the node hardware complexity and power consumption. Solutions based on UWB-RFID energy-autonomous tags with an on-board impulse UWB transmitter implemented on a full custom CMOS integrated circuit (IC) have been proposed [78][95][96][97]. Zou et al. [96] present a solution based on an energy-autonomous custom IC with an on-tag UWB transmitter, and demonstrate its capacity to localize tags with 5.4 cm error in a rather limited area of 1m x 1m. In this context, the design of a full custom IC allows to carefully tailor the circuit consumption to the available energy budget, because of the shrunk parasitics and of the degrees of freedom in the design. The UHF power scavenging circuit in [95] is reported to provide 2.5V and 1.5  $\mu A$  output current with minimum  $-17.1$  dBm

(19.5  $\mu W$ ) input power, which corresponds to 12 meters operation range with 4 W EIRP emission. However, during tag activation the circuit consumes more power: 51  $\mu A$  at 1.8 V supply (91.8  $\mu W$ ) at 10 MHz pulse rate, and 918  $\mu W$  at 100 MHz.

Thus, the strict constraints on energy consumption make solutions based on backscattering tags more efficient as proposed in [79][91][98][99]. In this case, the tag simply integrates a digitally controlled switch in order to modulate the impedance of the UWB antenna. An external reader is in charge of emitting UWB pulses which are backscattered from the tag in phase with the direct incoming signal (when the switch is open) or 180 degrees phase-shifted (inverted signal) when the switch is closed. On the reader side, the received sampled raw-data composed of backscattered tag signal and multi-path contributions due the presence of obstacles, is elaborated through appropriate signal processing algorithm to estimate the node position. Backscattering systems have been validated to combine good localization accuracy, range and power characteristics [79][99]-[104], even if the poor power link budget, because of the double UWB signal path, causes a lower tag to reader working distance, compared with transmitting tags.

To achieve high localization performance, several issues need to be tackled for the design and implementation of the backscatter-based passive UWB localization system. In particular, important challenges lie in the electronic implementation of backscattering tags, as well as in the design of dedicated signal processing schemes. To satisfy the strict power budgets dictated by the need for energy autonomy, it is essential that the intrinsic consumption of tags is aggressively low (a few microwatts), in order to operate at distances of several meters from the power source. This is a very challenging objective, since many custom ASIC implementations presented in literature still fail to achieve this goal, and implementations based on off-the-shelf components have to deal with the much higher parasitics.

## 1.5 Thesis outline

The *Chapter 1* has emphasized many key aspects of the PhD work which will be discussed more in details in the following Chapters. The project started with the study of energy harvesting solutions for wireless sensor networks and IoT based on battery-less devices.

Hence, *Chapter 2* shows hardware and software design criteria adopted to build an energy autonomous tag, following strong low power constrains policies mainly related to UHF radio-frequency and PV sources.

Based on this background, *Chapter 3* presents the hardware implementation of PV passive tags for outdoor and indoor sensing applications.

However, there are applications in which tags are attached to objects, entirely or partially working in Non-Line-Of-Sight (NLOS) conditions respect to WSN

receivers, where electromagnetic energy harvesting sources become an interesting solution to develop Energy Autonomous Tags. For these purposes, the architecture of a battery-free UHF-UWB transmitting tag is discussed in *Chapter 4*. Tag specs and requirements used to define both, hardware and software choices, are related to the ESA-LOST project (funded by the European Space Agency), in which part of this project was developed, with the aim to energize and localize Objects in space through RF passive tags.

Starting from the results achieved within this activity, in the process of extending the functionalities of the presented solution, in *Chapter 5* the node has been integrated with EPC Gen 2 standard (compliant with the current European regulations) by making it more attractive for the market. The advantages of a standardized system, combined with low-power UWB backscattering localization technique, allowed the creation of an hybrid node called UWB-RFID tag, described in *Chapter 6* able to be read and locate in quasi real-time.

It is worth to notice that, the thesis work is the result of a multidisciplinary activity which involves aspects of electromagnetic fields, electronics, telecommunications and computer science. This thesis is mainly related to the electronic design of tags besides system level integration activities in laboratory in order to merge contributions of the research partners, in the other fields, and verify the overall performances.

# Chapter 2

## Low Power design strategies for UHF passive Tags

### 2.1 UHF Energy Harvesting Front-End

The radio-frequency front-end, Fig. 2.1, is typically based on a *rectifying antenna* combined with a *matching network* used to match the antenna impedance with the cascade of *rectifiers*, placed in order to accomplish the RF-to-DC conversion.

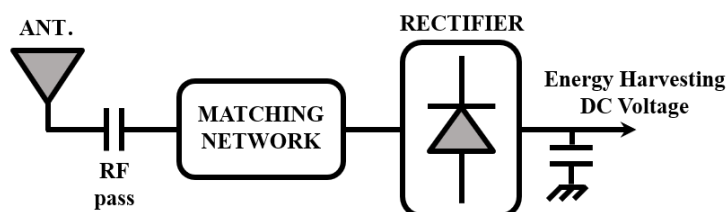


Figure 2.1: Typical radio-frequency front-end for energy harvesting purposes.

The rectifier design has been widely investigated in the last years [105][106]. Different topologies are possible, depending on the specific application scenario. When the available RF power levels are very low, e.g., below  $-20$  dBm, half-wave rectifiers topologies are typically adopted, being able to provide higher conversion efficiencies. If the available RF power is higher, full-wave rectifiers represent the best option. Depending on the specific scenario, the main goal of the rectifier design could be maximizing the output dc voltage or the output dc power. The UHF front-end available in the market and literature, are typically based on Schottky diodes (faster compared to other types of this device family) in both discrete [107][108] and integrated circuits [109] or advanced MOSFETs architectures [110][111][112]. Unfortunately, having improved rectifier sensitivity and efficiencies require low

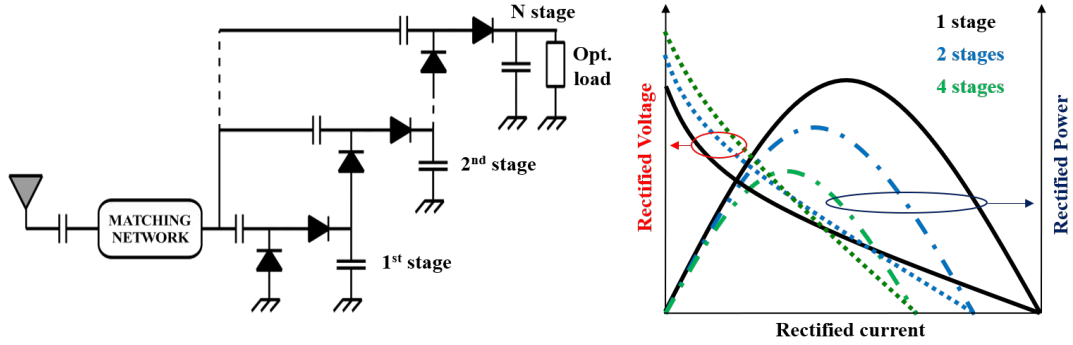


Figure 2.2: Multi-Stage Rectifier topology and performances.

threshold devices. For this reason, many research activities have been dedicated to  $V_{TH}$  cancellation and compensation schemes [113][114]. However, if the rectified voltage plays the predominant role, with respect to the power conversion efficiency, multiple rectifiers can be connected in series, providing voltage multiplication, while keeping the converted dc power unchanged. Obviously, besides voltage multiplication, every additional stage introduces also a voltage drop, due to the intrinsic turn on threshold of every diode, which directly affects the rectified power, and thus the RF-to-DC conversion efficiency, Fig. 2.2. Therefore, the best trade-off can be chosen, accordingly to the requirements of the specific application.

However, there exists an upper limit of the number of stages since the diode losses may have the upper hand over the dc voltage increase: at this point all the advantages of voltage multiplication are lost. As a representative example [115], all these concurrent aspects are considered for the following scenario conditions: a reader, exploited for both energy transfer, is located at 13-meter distance, in free-space conditions; the maximum ERP is 2 W in the European UHF band. The rectenna (rectifying antenna) is a meandered dipole having 1.3 dBi gain at 868 MHz. In the RF link best-case conditions, i.e., with the TX antenna linearly polarized and in perfectly polarization matching condition with the RX dipole, the RF received power at the harvester input is  $-17$  dBm ( $20 \mu\text{W}$ ). By adopting a properly matched, single-stage, full-wave rectifier, employing two Skyworks SMS7630 Schottky diodes, the maximum RF-to-dc conversion efficiency is equal to 28 %, which results in an available dc power equal to  $5.6 \mu\text{W}$ . In order to obtain a higher dc voltage, the rectifier outputs are also monitored for an increasing number of rectifying stages, the results are reported in Tab. 2.1. The gain in terms of voltage multiplication is evident up to the sixth stage, at the expense of a reduced power. It is also possible to observe that, by further increasing the number of stages, diode losses annihilate the advantages of voltage multiplication.

A different approach can be investigated in case raising the available dc voltage

n° of stages	$V_{\text{RECT}}$ (mV)	RF-to-dc efficiency	$P_{\text{RECT}}$ ( $\mu\text{W}$ )
1	211	28 %	5.6
2	322	23.9 %	4.8
4	353	19,9 %	4.0
6	372	13.5 %	2.7
8	280	8.9 %	1.8

Table 2.1: Rectifier number of stages comparison [115].

is a priority specification, with respect to the dc power for activating the tag. In this case, instead of cascading different rectifying stages within a single rectenna, the output of multiple rectennas can be combined [55][116]. By series-connecting the dc outputs of each rectenna, it is possible to obtain a voltage multiplication with respect to the single rectenna case, while preserving the dc output power obtainable from the stand-alone antenna configuration. The main advantage consists in maintaining a constant dc output power. Indeed, by dc-connecting different and equally-excited rectennas at their respective dc outputs, the power converted by each one of them is added, but the corresponding optimum load has typically to be increased by a factor equal to the number of added stages, therefore the overall RF-to-DC efficiency remains constant. Depending on the application, series or parallel connection of the outputs can be adopted for a corresponding voltage or current multiplication, but the entire area allowed for the tag, also imposes serious constraints on antennas location and spacing.

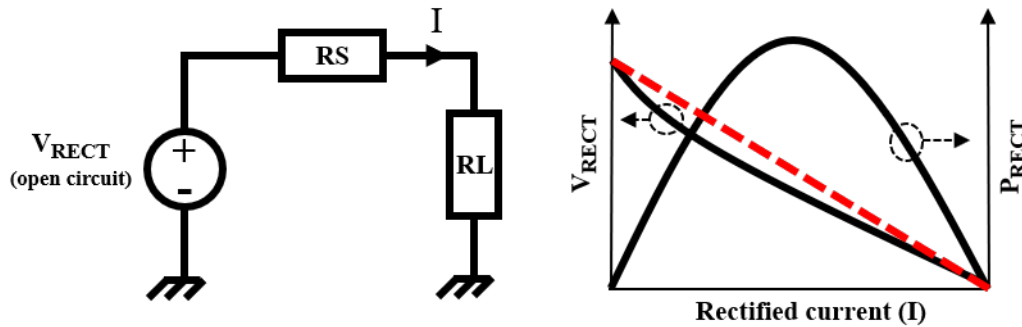


Figure 2.3: Equivalent model of a rectifying antenna.

Moreover, an important role is played by the rectifier output impedance, which has to be managed according to the input impedance of the Power Management Unit (PMU), in order to extract the maximum power. A rectifying antenna can be represented with an equivalent model through a voltage generator followed by a series resistor (typically the output resistance of the rectifiers chain), as shown

in Fig. 2.3, since the non-linear curve of the output voltage, as a function of the output current, has a linear behavior as first approximation. In this particular case, from the maximum power transfer theorem (Jacobi's law), it is possible to state that the resistance of the load (RL) must be equal to the resistance of the source (RL), with typical values of few kOhm.

## 2.2 Wake-up Radio (WuR)

Nowadays, in wireless sensor networks, energy-efficient communication is one of the main concerns. A common approach, for achieving energy efficiency and lower power consumption, is the use of a *Wake-up Radio* circuit, where the node of interest is woken up only on-demand to get the information, while during the steady state operation, it is in listening mode for possible incoming radio communication.

Generally, the WuR implementation is derived directly from the RF front-end circuitry of the rectifying antenna (discussed in the previous Section) used for energy harvesting purposes, Fig. 2.4. In particular, an unbalanced *capacitor divider* based on  $C_{up}$  and  $C_{down}$  delivers most of the energy to the power management path, while a small part of the received signal is dedicated for *Wake-up Radio* capabilities. The latter, has the function to demodulate the incoming RF signal in order to perform the addressing phase used for node identification and awakening from sleepy state.

As shown in Fig. 2.5, the incoming signal are generally filtered and cleaned up through a data-slicing technique, before being processed by an Ultra-low power microcontroller (ULP MCU) or a dedicated correlator. The aim is to generate the wake-up interrupt only when the desired tag has been addressed.

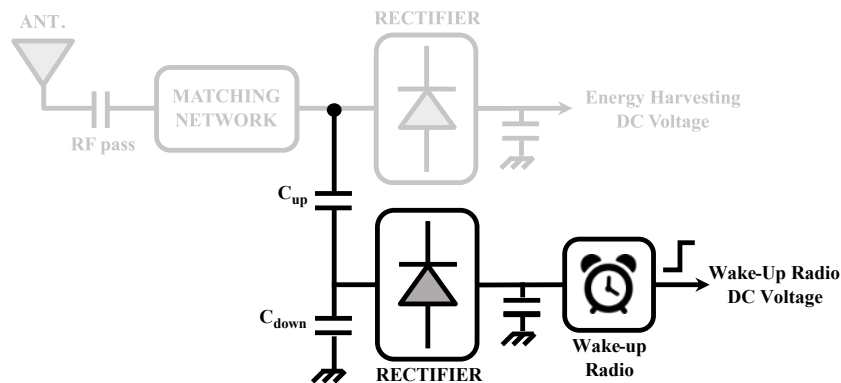


Figure 2.4: General scheme of a Wake-up radio system integrated with an energy harvesting interface.

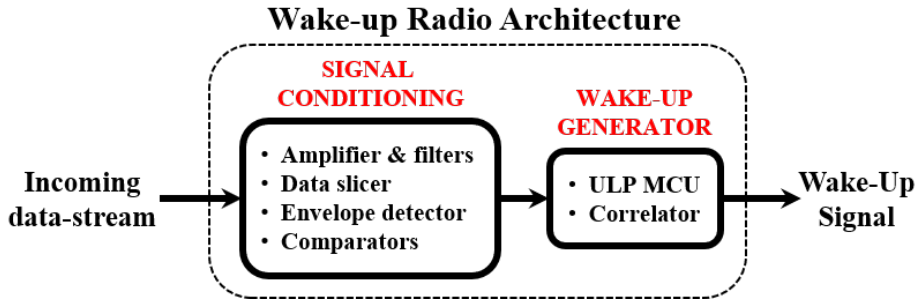


Figure 2.5: Wake-up Radio architecture.

Basically, the WuRs can be divided as function of the power supply source in *passive*, *active* and *semi-active*, as described for RF nodes in Chapter 1.

Within these categories the main classification is focused on the hardware composition of the receivers diversified for *technology*, *frequency source usage*, *address decoding* and *modulation techniques* [117].

### 2.2.1 Technology

WuRs can be implemented in two different approaches by considering discrete schemes based on off-the-shelf components or customized integrated circuit which guarantees lower leakage current consumption compared to the other solutions.

Discrete wake-up radios allow the designers to simplify and speed up prototyping, with low cost and high flexibility systems. Instead, CMOS integrated circuits don't permit a quick implementation though they can reach higher efficiencies and sensitivity, with lower power consumption and smaller sizes, gaining a strong impact on the working distances between the transmitter and the receiver (node).

Technology	References
discrete	[53][54][118]-[126][127]-[130]
CMOS/BiCMOS	[131][132][133][134]-[140]

Table 2.2: WuR categorization based on type of technology.

In Tab. 2.2 are collected the literature contribution divided for hardware architecture type. References have been highlighted in (i) *red* all of those that implements an OOK modulation scheme through a Sub-GHz front-end which is a target of the thesis work and (ii) *green* for contributions referred only to RF front-end circuits (without address decoding).

It worth to mention that, M. Magno et al. [122][125] presented a simple and effective discrete Wake-up receiver, which achieves a power consumption of  $1.2 \mu\text{W}$ ,

with a maximum sensitivity of -55 dBm. The architecture of the WuR, includes a matching network needed to provide maximal power transfer between the antenna and the passive rectifier, which converts the input radio signal into dc signal. A preamble detector is placed to activate a microcontroller, used to decode the received address. Jiang et al. [138] have presented an innovative ultra-low power WuR solution which is able to consume only 4.5 nW, with -69 dBm Sensitivity, in 0.18  $\mu\text{m}$  CMOS SOI process. The system shows a front-end made with High-Q transformer, which provides high passive gain, followed by an envelope detector (20 times larger conversion gain, via active inductor, respect to conventional schemes) and a low noise high-gain regenerative comparator that slices bits at low power. All circuits operate at 0.4 V in order to reduce the overall power consumption.

### 2.2.2 Frequency usage

In Tab. 2.3 WuRs are classified as function of the frequency source usage, by considering Sub-GHz and 2.4 GHz receivers. The choice between them depends on the final application, considering that the operating frequency determines the size of the antenna and the operational range of the system. The increment of the frequency permits to reduce the dimension of the antenna with the disadvantage of more complex circuit scheme and design (as it has been already described in Chapter 1).

Band	References
Sub-GHz	[53][54][118]-[121][124][126][131][132][141]-[146] [133][109][122][123][125][127][134][147][148]
2.4 GHz	[145][149][128][129][135][137][139][140][143][150]-[157]

Table 2.3: WuR categorization based on type of frequency Band.

### 2.2.3 Address decoding

The usage of a low power microcontroller (MCU) is a viable solution to perform the correlation between the received wake up signal and the identification address of the node, providing more flexibility due to the firmware implementation of the digital block. Bdiriet et al. [123], presented a low power wake up radio with the comparison between the Microcontroller MSP430 and the AS3932 receiver, both used in order to accomplish the address decoding phase. However, they declare that the MCU permits to preserve energy, if the duty cycle operation of the node is really low (longer sleep time), because the steady-state current consumption, in low power mode, is smaller respect to AS3932. Instead, when the data communication

rate increases, since the microcontroller goes in active mode each time it receives an address, the current consumption grows up to hundreds of  $\mu\text{A}$ , by dropping the choice to AS3932 whose power consumption is an order of magnitude smaller.

Instead of using MCUs for address decoding, an energy efficient way is to use a *correlator* circuit for address matching, which can lead to lower power consumption. In a correlator circuit, the node address is stored in a reference register (non volatile memory) and the input bits from the *WuS* (*Wake-up Signal*) are correlated against the reference signal. Once a new bit is received, the samples are shifted of one position and so on. If the bits are matched, the system provides a wake-up interrupt, Fig. 2.6. Hambeck et al [131] implemented a complete prototype of WuRx, employing a 64-bit mixed signal correlator for address matching.

At 868 MHz, the receiver has a sensitivity of -71 dBm and an outstanding measured free-space radio link distance of 304 m, at transmission power of 6.4 dBm. At these conditions, the radio dissipates  $2.4 \mu\text{W}$  at supply voltage of 1 V. Other address decoding techniques, Tab. 2.4, using *Bloom filters* [134], *shift registers* [142], *flip-flops*, and *filter banks* [128] have been exploited with worse results in terms of power consumption.

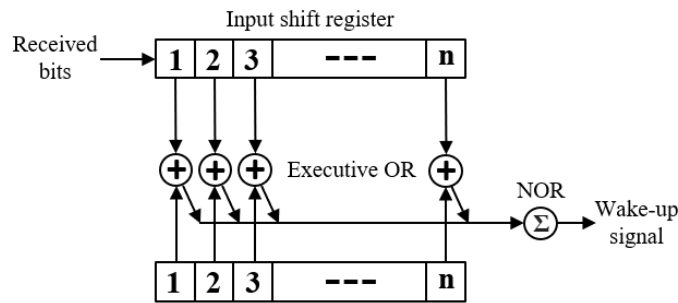


Figure 2.6: Correlator principle scheme.

Technique	References
MCU	[53][54][118][122][123][125][144][145][127][151][157]
Correlator	[119]-[121][126][131][132][141] [143][158][136][129][137]-[140] [148][153][154][156][159]
Others	[142][128][134]

Table 2.4: WuR categorization based on type of address decoding. The *blue* marker refers to digital-based wake-up radio without a RF front-end.

### 2.2.4 Modulation techniques

The digital modulation schemes that can be adopted, Tab. 2.5, are referred to *ASK* (*Amplitude Shift Keying*), *FSK* (*Frequency Shift Keying*) or *OOK* (*On Off Keying*) which have a significant influence on the power consumption and robustness of the data communication. As we can imagine, each of them has different advantages depending on the application required. Typically, for an ultra-low power wake-up radio receiver, used in energy autonomous nodes, an OOK modulation is chosen due to its lower power consumption and simple hardware scheme. In fact, the demodulation circuit has to only distinguish between two states: logic level "1" and "0", in order to recognize the received bit-frame. This function can be satisfied with a low cost solution, through the combination of a *low pass filter* and *comparator* [53][54][122][125].

Modulation	References
OOK	[53][54][118]-[126][131] [132][141][145][146][148] [149][152][136][128][129] [137]-[140][143][144][151] [153]-[155][158][159]
ASK	[109][124][127][134]
FSK	[124][133][148]

Table 2.5: WuR categorization based on type of Modulation.

## 2.3 Power Management Unit

Power management is, in general, a critical issue in this type of applications. Power from RF rectifiers must be converted and managed in highly variable conditions. In particular, as distance from the RF source increases, rectennas produce voltages ranging from several Volts down to few hundreds mV at several meters [160].

The maximum available power can also range from few mW down to few  $\mu$ W [161]. At high distances, since the typical supply voltage of tag circuitry is quite higher, it is necessary to boost the input source. Hence, the overall PMU architecture, depicted in Fig. 2.7, is divided in two main blocks: a *start-up circuit*, based on low-threshold devices used to multiply the low input voltage coming from the applied RF source, and a *main converter* typically built with buck-boost DC/DC converter, in order to efficiently boost the contribution of the cold-start circuit for energizing the load. Moreover, a high power conversion efficiency can be reached through *Maximum Power Point Tracking (MPPT)* algorithms performing

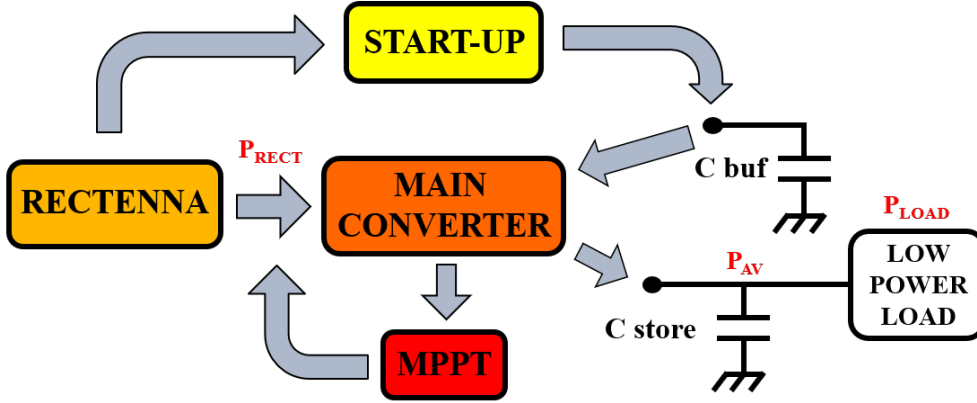


Figure 2.7: Power management unit block scheme.

a *Fractional Open-Circuit Voltage (FOCV)* of the input source. As shown in Fig. 2.2, the maximum power point occurs when the open circuit voltage is reduced by a factor  $k$  according to the input source type. When the start-up circuit is enabled, the small self-supply capacitor  $C_{buf}$  gets charged: this achieves very fast activation times even in the presence of large buffer capacitors on the load port ( $C_{out}$ ). However, in battery-less implementations of tags, step-up switch-mode boost converters or charge pumps do not operate when the input voltage is much lower than the threshold voltage of the adopted power switches. Then, besides power, voltage also represents a potential limitation to the operating distance. Other duties of the power management circuitry include voltage regulation and power distribution to the other sub-sections of the tag, and protection of circuit elements from over-voltages.

### 2.3.1 Start-up circuit

Although, on the RF side, the matching network can contribute to increasing the input voltage for the power management part [160][162], by exploiting resonance with dedicated or on-chip capacitors, the *start-up (SU)* circuit represents a crucial part of the PMU. In literature, several integrated SU circuits operating down to  $-26.3$  dBm are reported [163][164]. They are mainly based on multi-stage threshold-compensated rectifiers. However, a notable sensitivity of  $-32$  dBm at 915 MHz was reported in [165], where tens of rectifier stages operating in the sub-threshold region are cascaded. Power conversion efficiency increases at the expense of system dimensions when switching converters are adopted. As an example, in [166], sustainable operation with an input power of  $1 \mu\text{W}$  ( $-30$  dBm) is demonstrated. Concerning miniature energy autonomous tags performing UWB localization, a notable example is reported in [97], which achieves operation with input power



$$V_{out} = \sum_{i=0}^n (V_{DD} - V_{th}) + V_{DD} \quad (2.1)$$

Typically, the cold start-up phase from a fully discharged state is characterized by a higher intrinsic consumption and lower conversion efficiencies compared to steady-state power conversion.

### 2.3.2 Main converter

It is typically designed with switched-inductor solution, which requires off-chip inductors. The main topology is constituted by a buck-boost converter which can be schematized as shown in Fig. 2.9.

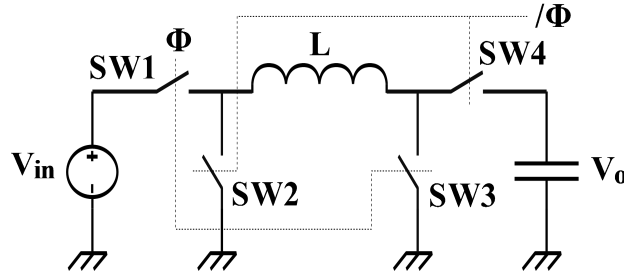


Figure 2.9: Typical Buck-Boost convert scheme.

The presented topology has two switches pairs, which are driven through the signals  $\Phi$  and  $\bar{\Phi}$  according to the desired output voltage. In particular, with the assumption of ideal switches and continuous current mode operation of the converter, the working principle can be studied in two separated timing intervals called  $T_{on}$  and  $T_{off}$ . In the former,  $SW1$  and  $SW3$  are closed while  $SW2$  and  $SW4$  are open, allowing the current flowing from the input source to the inductor. In this phase, the inductor current variation is given by the following equation:

$$\Delta I_{on} = \int_0^{DT} \frac{V_i}{L} dt = \frac{V_i DT}{L} \quad (2.2)$$

where  $D = T_{on}/T_{off}$  is the duty cycle and  $T$  represents the control signals time period. On the other hand, during the  $T_{off}$  mode only switches  $SW2$  and  $SW4$  are closed and the inductor progressively charges the output capacitance. The electric current variation during this working mode can be expressed as follow:

$$\Delta I_{off} = \int_0^{(1-D)T} \frac{V_o}{L} dt = \frac{V_o(1-D)T}{L} \quad (2.3)$$

Hence, since the inductor current variation in a time period  $T$ , within ON and OFF modes, is zero ( $\Delta I_{on} - \Delta I_{off} = 0$ ), by replacing the results of Eq. 2.2 and Eq. 2.3, it is possible to obtain:

$$V_o = \frac{V_i D}{1 - D} \quad (2.4)$$

Thus, it is understandable that, the duty-cycle variation can step-up or step-down the input source  $V_i$  according to the load required policies.

Many contributions have been released based on the presented circuit scheme. On the market side, several power management unit IC (PMIC) are already widely used in commercial sensor node applications, such as TI bq25570 which integrates a start-up circuit from 300 mV and 15  $\mu$ W of input power, an inductor-based buck-boost converter for energy harvesting from different sources, besides MPPT algorithm and voltage monitor for an efficient power conversion. Other products such as SPV1050 from STMicroelectronics and ADP5090 from Analog Devices follow similar design architecture and performances. However, for long range applications, the main bottle-neck is given by the input power requirements needed to end the cold-start operation in order to activate the main converter. For this purpose, significant improvements have been done during the years, observing the birth of devices capable of working at reduced input power conditions. It is the case of E-peas company, which presents several PMIC solutions depending on the type of applied source (for radio-frequency the suggested product is AEM30940) with a strong reduction of input power requirement to operate properly ( $\simeq 3 \mu$ W). Moreover, even in academic field, power management solutions for energy harvesting purposes have been designed in both, discrete [170] and ASIC implementation [171] achieving relevant results as high sensitivity and low power consumption. All the products previously mentioned, are expected to work in both: *continuous conduction mode (CCM)*, when enough incoming power is received and in *discontinuous conduction mode (DCM)* for low input power levels (micro-power).

In some cases, in order to provide a stable supply voltage  $V_{DD}$  on the output stage of the main converter, voltage regulators can be investigated for the tag circuits design. For this purpose, low-dropout regulators represent an effective solution with limited power consumption [172]-[174]. In this type of circuits, the resistance of a switch connected in series with the unregulated voltage, is modulated according to the load current, in order to introduce a suitable voltage drop that causes  $V_{DD}$  to appear after the switch.

## 2.4 Low-power design strategies

The design of a battery-less tags is a critical aspects from the power consumption point of view and so, implementation strategies and policies have to be take into account to create efficient energy autonomous systems [56]. For the consideration done in the previous Sections, it has been assumed that the node can work in *continuous mode* where the received power, from the energy harvesting source, is sufficient in order to accomplish the load tasks and duties. Unfortunately, this assumption does not represents the truth in all possible situations, in the sense that, there are cases in which the harvested power can not satisfy the minimum working condition of the node. In particular, by observing Fig. 2.7, for a continuous mode operation the available power ( $P_{AV}$ ) has to be greater than  $P_{LOAD}$ , otherwise the energy harvested in the storage capacitor is progressively consumed, by lowering the supply voltage and as consequence the node switches off. Thus, in order to preserve energy and not waste it, the node is equipped with circuitry able to work in *duty-cycled mode* in which the load is powered only when the specified operative conditions are respected. It is worth to mention that, if the available power is lower than quiescent power consumption of the power management unit (minimum working condition), the main converter stop to operate and slowly discharges the internal capacitors.

### 2.4.1 Duty-cycled operation mode

The load power gating control is performed through a regulation loop based on monitoring circuits of the storage voltage, as shown in Fig. 2.10.

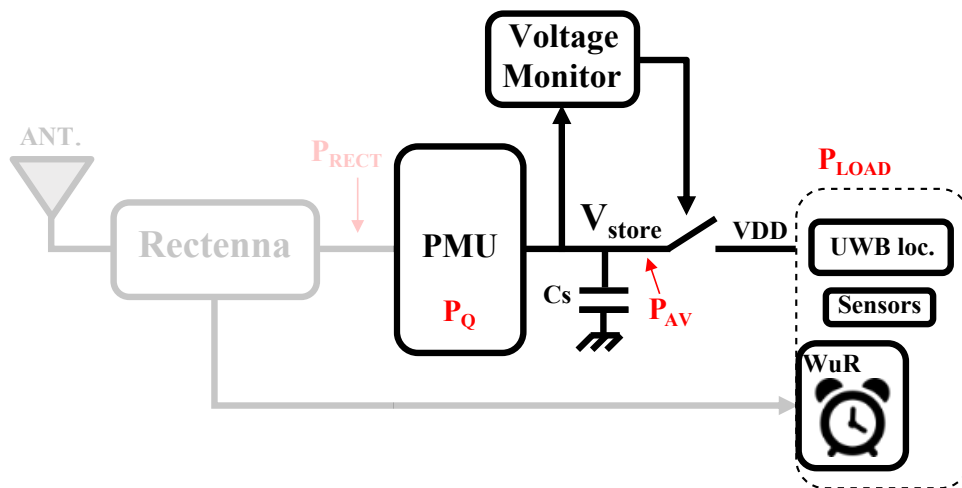


Figure 2.10: RF battery-less architecture with load power gating feature.

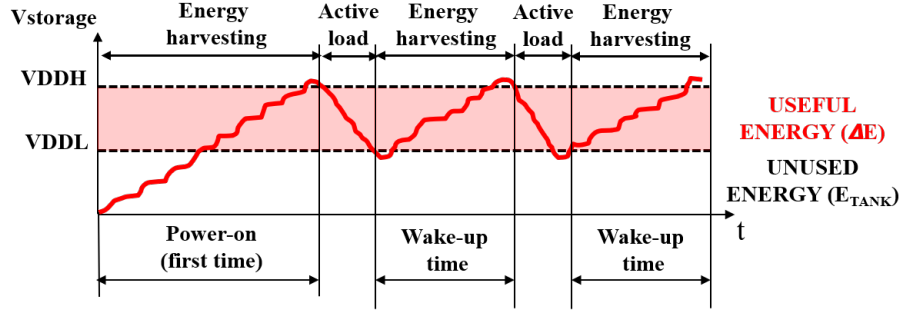


Figure 2.11: Duty-cycled operation mode.

The *Voltage monitor* is in charge of selecting two separated threshold voltages: upper ( $VDDH$ ) and lower ( $VDDL$ ) according to specific constrains. In particular, the unwanted effect is that the load is continuously powered even if the storage voltage is comparable or lower than minimum supply voltage condition. Thus, the lower threshold  $VDDL$  is set slightly greater than minimum power supply required to operate. When  $V_{store} < VDDL$  the unused energy ( $E_{TANK}$ ), contained in the storage element, helps for faster power up time when the load is switched on again, Fig. 2.11. Hence, it is understandable that, after the first power-on, the node operates between *active* and *re-charging* states, where is placed the useful energy ( $\Delta E$ ) of the system, which is expressed as follow:

$$\Delta E = \frac{1}{2}C_s(VDDH^2 - VDDL^2) \quad (2.5)$$

The useful energy is calculated according to the amount of energy needed by the load to perform a specific task. Hence, In order to define the upper threshold, there are different strategies depending on the target application. When fast power-up time, starting from a fully discharge state, represents the main constrain compared to low power design choices,  $VDDH$  is chosen as higher as possible, allowing to have smaller storage capacitance, as can be derived from Eq. 2.5. Instead, if an ultra-low power design is required, the idea is to define  $VDDH$  as small as possible, by working with low supply voltages, as consequence of higher storage capacitance ( $C_s$ ). However, if  $VDDH$  increases, the power consumed increases as well.

Once the threshold voltages have been defined, the voltage monitor can be implemented through the typical architecture of an hysteresis comparator, which is shown in Fig. 2.12. When  $V_{store} > VDDH$  the output of the comparator goes high ( $V_{store}$ ) in order to supply the load. At the same time,  $R3$  becomes in parallel to  $R1$ , carrying higher current to  $R2$  with the effect of increasing the voltage  $V+$ . Thus,  $V_{store}$  has to drop below  $VDDL$  for switching off the load. In this specific case, the resistor  $R3$  back in parallel to  $R2$ , by restoring the upper threshold.

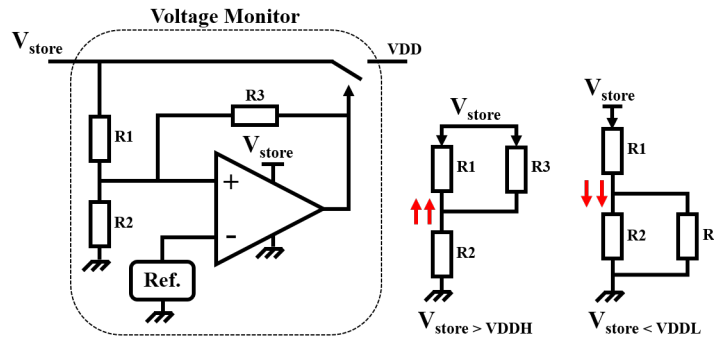


Figure 2.12: Voltage monitor architecture.

### 2.4.2 Policies for power optimization

An active interaction between the power management unit and the load allows to build a smart energy autonomous node able to take decisions based on external events. Hence, optimized policies need to be investigated with a view to exploiting the available energy at its best. In order to achieve the goal of low-power design, from the load point of view, two operating modes can be implemented, based on modern microcontroller architectures: *Stand-by mode* and *Off mode*, Fig. 2.13.

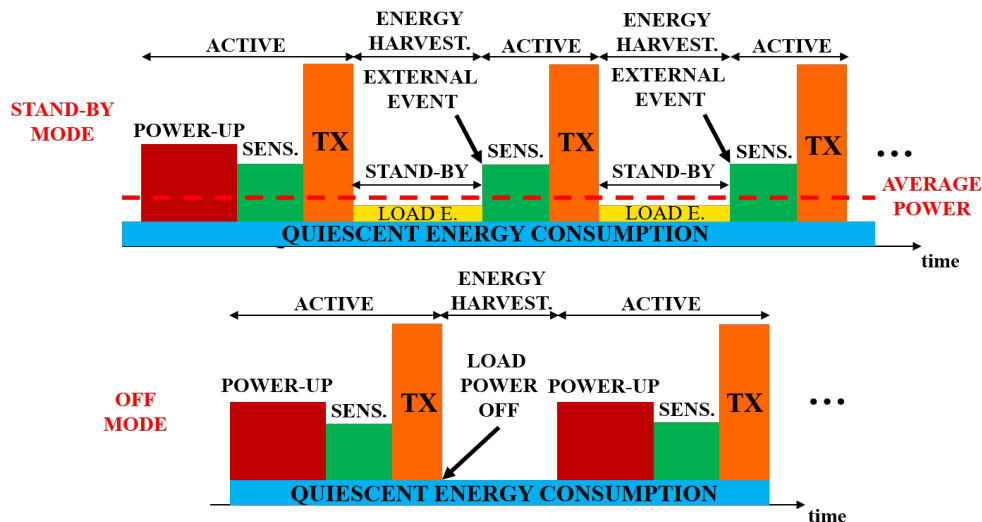


Figure 2.13: Tag operation in Stand-by mode and off mode.

Both solutions, behave in the same way at the first tag power on, when, after the start-up phase, the node acquires data from the sensors and transmits them to the receivers. Afterwards, if *off-mode* is selected, the node generates a signal for the energy harvesting part to inform it that the processing operations have

been completed and the power supply can be switched-off. When power supply is restored, the node will perform a new start-up phase with high in-rush currents, data acquisition and message transmission. On the contrary, if the *stand-by mode* is chosen, after the start-up phase and message transmission, the node enters in deep sleep state in which the current consumption is significantly lower compared to the active state, but higher than in the *off mode*. The tag waits for an external interrupt, generated by an optimized policy circuitry, and subsequently, performs a new data acquisition/transmission. In this case, the node is never powered-off and the overhead consists in constant load power consumption (with wake-up times significantly faster). Instead, in *off mode* the periodic switch-on creates an overhead which becomes relevant for high data acquisition rate. The selection between *off mode* and *stand-by mode* has a significant impact on the power budget.

Thus, which of the two modalities costs less depends on the *frequency of activation*. For frequent activation, the *stand-by mode* consumes less energy. Furthermore, the frequency of activation strictly depends on the amount of harvested power.

For these reasons, specific circuits can be designed which dynamically change the behaviour of the system according to different scenarios of available environmental energy, without human intervention. In Fig. 2.14 the first proposal of smart battery-less node with an adaptive power management system is presented, which scheme has been experimentally validated in [56].

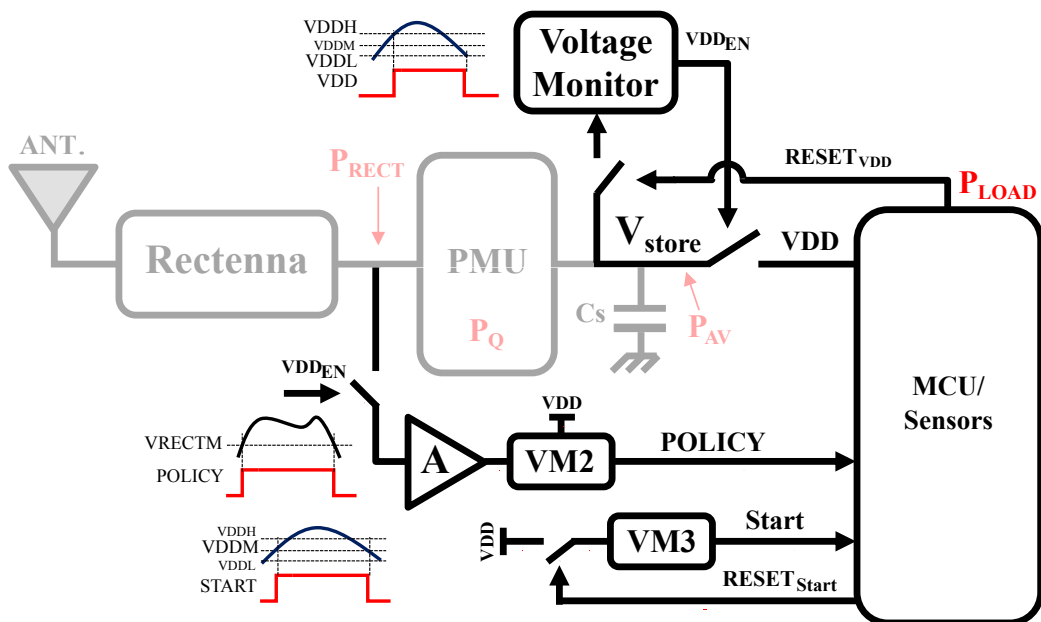


Figure 2.14: Tag hardware architecture with stand-by mode and off mode implementation. The solution is *Tag oriented complexity*.

The interface between PMU and the sensor node is implemented through four control signals (*Policy*,  $Reset_{VDD}$ , *Start*,  $Reset_{start}$ ) which are managed by a micro-controller or dedicated digital blocks. Hence, three control circuits are necessary to implement the policies. The first one is the *Control circuit for off mode*. This block has the task of monitoring the storage voltage on the capacitance  $C_s$  and consequently to provide power supply to the connected load only when the voltage is in the acceptable range ( $VDDL - VDDH$ ) as discussed in the previous Section. During the off-mode, a reset signal ( $Reset_{VDD}$ ) must be issued by the MCU at the end of each transmission stage as auto-kill action, in order to help the PMU for faster re-charge time of the storage capacitance, during the energy harvesting phase. This behaviour ensures that the next transmission occurs only when  $VDD > VDDH$ . The second one is the *Control circuit for stand-by mode*. This block has the aim of controlling the  $VDD$  voltage and providing the start signal only when it is above a certain threshold ( $VDDM$ ) placed in between  $VDDL$  and  $VDDH$ . During *stand-by mode*, the node is always powered and all transmissions are regulated by the *start* signal, which has to be generated only when the available energy is enough to sustain the double task of sensing and data transmission. The minimum transmission period is obtained, in both presented operating modes, due to the fact that a re-transmission is performed when the storage capacitance has recovered the energy lost during the active phase. The *off mode* proves more suitable when the rectified current is relatively low (especially for long working distances between tag and readers), whereas the *stand-by mode* becomes more cost effective at higher rectified currents, where the transmission frequency is much higher. Thus, it is possible to define a rectified current and voltage thresholds ( $VRECTM$ ), depending on the adopted hardware, in which the system has to perform the operating mode exchange. The *Control circuit for policy detection* represents the referee of the system. It is based on a low power non-inverting amplifier stage used to collect and amplify the average rectified voltage, before to be monitored by a voltage detector, which implementation has been already discussed in the previous section. The policy signal generated, determines the current mode that has to be adopted as best low power choice. It is worth to mention that, the reset signals used in this configuration, drive a switch placed to break the path between the signal to be monitored and the voltage detectors, in order to instantaneously get out from the hysteresis. The presented solution can be named as *Tag oriented complexity*, where the node is autonomously able to take decisions in relation to the available energy.

However, another solution could be to move the smart decisions from the tag to the reader for a *Reader oriented complexity*, Fig. 2.15. Basically, the reader energizes and identify the node, in order to perform a RSSI estimation of the tag backscattered signal, to define the correct policy. When the measured received

power gives a poor contribution, the tag is located at high distances from the reader and the best choice falls on the *off mode*. On the contrary, if the RSSI is high, it means that the tag is in the proximity of the reader and the *stand-by mode* gives better results in terms of power consumption. The reader is in charge of communicating the policy choice to the tag, through the Wake-up radio, with the implementation of custom commands, or standardized protocol such as RFID EPC Gen. 2. The reply back tag to reader is performed with a RF switch used to modulate the impedance of the UHF antenna according to the data to be transmitted.

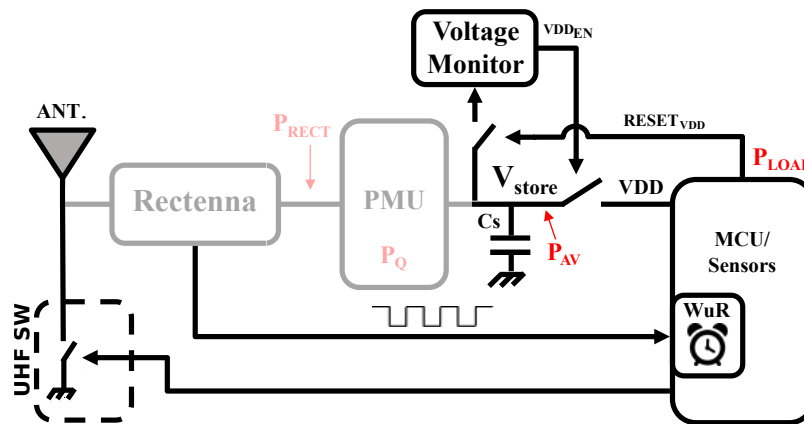


Figure 2.15: Tag hardware architecture for optimized low power policies. The solution is *Reader oriented complexity*.

# Chapter 3

## PV passive Tags for WSN

### 3.1 Motivations

Among the most promising sources for energy harvesting, which permit to have higher extracted power density compared to other type of available solutions, are light sources (natural or artificial). The scenarios in which they can be used in order to build photo-voltaic passive nodes are not necessarily overlapped with radio-frequency energy scavenging applications, due to the different peculiarities of both systems. In fact, if on one side, RF tags are able to work under adverse non-line-of-sight conditions between the nodes and energy source, on the other hand PV tags not require distributed energy showers to properly operates and the infrastructure cost can be significantly lower. The activities presented in this Chapter, arise from the *Horizon 2020* project *CONNECT (ECSEL JU)* [175] and *Convergence (ERANET)* [176]. In particular, *CONNECT* aims to provide concepts, technologies and components that support enhanced integration of renewables and storage combined with intelligent management of the energy flow. This requires ubiquitous sensing nodes. Similar approaches can be found in *Convergence*: the main project strategy is centred on proofs-of-concepts related to energy efficient sensor networks for future wearables, exploiting the *convergence* of multi-parameter biosensors and environmental sensors on an autonomous system technology platform, serving data fusion for preventive life-style and healthcare. One again, energy autonomous sensing is is the enabling technology.

## 3.2 PV Tags hardware architecture

Fig. 3.1 presents the hardware implementation of the PV Tags discussed in this Section.

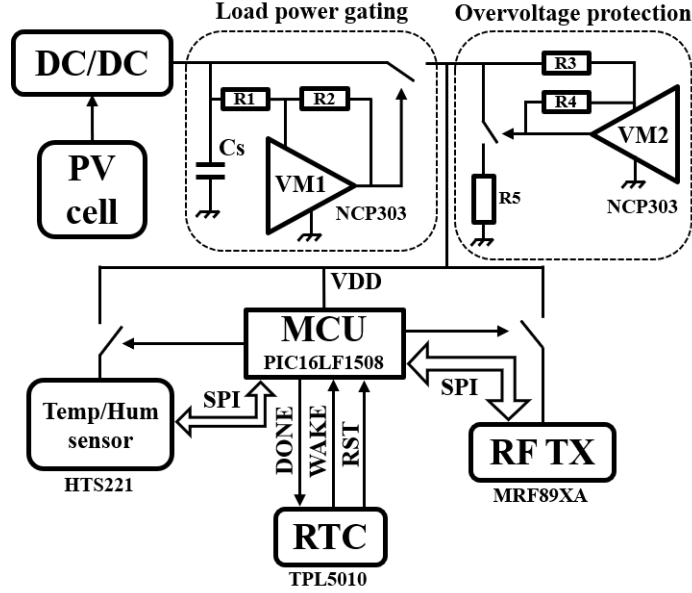


Figure 3.1: PV Tag hardware architecture for Wireless Sensor Networks.

They are based on a low power micro-controller unit (Microchip PIC16LF1508) used to collect the temperature/humidity (STm HTS221) information from the environment and store them in a non-volatile memory as data-logger. The presence of the UHF transceiver (Microchip MRF89XA) permits to deliver all data to a client making them available for users. Energy harvesting is performed, through the usage of PV cells, for both outdoor or indoor applications, as energy source, which is managed by the dc/dc converter unit. It is in charge of collecting energy in a capacitor and make it available to the load when sufficient to supply the overall system. Moreover, a voltage monitor (ONsemi NCP303) has to perform the load power gating to not waste energy when the storage voltage is lower than minimum required supply voltage of the load. Since the output of the main converter [166][171] is free to operate up to 9 V, an *over-voltage protection circuit* is mandatory to avoid the load damage due to the presence of high input voltages. Hence, the voltage clipping circuit can be done with a simple solution based on Zener diodes, but they are not suitable for low power applications due to their high leakage current even when operates not close to the breakdown voltage. For a sharper I-V characteristic curve a low-power optimized circuit has been used which can guarantee low current consumption of few nA during the node operation.

The working principle is to modulate the current flowing to ground through a switch and the resistor R5, in order to have a high current absorption when the storage voltage reaches the over-voltage threshold. When the available energy is enough for a continuous node operation, an external low power timer (TPL5010) regulates the data-acquisition time of the sensors which can start from few seconds up to two hours depending on the type of application and needed. The sensor and RF transceiver are periodically turned on/off through low power switches (STm AS11P2TLR), according to active and sleeping periods of the node, as low-power strategy, in order to consume a small amount of current during steady-state operation. According to the load properties, it is switched on only when the storage voltage rises over a certain threshold ( $VH = 2.65$  V) and disconnected under the lower threshold ( $VL = 2.1$  V). The external resistor sizing of the voltage monitor can be done through the following equations:

$$VL = \left( \frac{R1}{R_{IN}} + 1 \right) V_{DET-} \quad (3.1)$$

$$VH = \left( \frac{R2}{R_{IN} // RL} + 1 \right) (V_{DET-} + V_{HYST}) \quad (3.2)$$

Where, the NCP303 internal resistance  $R_{IN}$  is  $10 \text{ M}\Omega$ ,  $V_{DET-} = 2$  V represents the reference voltage embedded in the voltage detector and defines the lower bound in which is possible to set VL, while  $V_{HYST} = VH - VL = 0.55$  V. Thus, starting from Eq. 3.1, R1 is calculated to be  $500 \text{ k}\Omega$ . Hence, by substituting the obtain parameters,  $R2 = 10 \text{ M}\Omega$  is computed from Eq. 3.2. The same considerations can be done for the over-voltage circuit protection, in which the maximum allowed power supply is  $V_{OV} = 3.3$  V. In this case, the voltage hysteresis has to be chosen as small as possible in order to have only one-threshold voltage ( $V_{OV}$ ) without wasting energy during the normal operation mode.

### 3.3 Node operation

In reference to Fig. 3.1 and 3.2, the MCU manages the system operation by alternating both active and sleep phases. Once the first start-up is ended, the microcontroller is set in sleep mode waiting the release of the power-on reset (RST) from the external timer. Subsequently, after the RF transceiver and sensor initialization, the latter starts to acquire the first temperature and humidity.

When the data are ready, the MCU is externally woken-up (*DRDY*) in order to read the sensing information before being transmitted. If the available power is enough to accomplish other one-shot measurements, the node goes into a loop in which the periodic data acquisition/transmission is regulated through the *WAKE*

signal, issued by the external real-time clock (timings from a few seconds up to hours). Many physical quantities to be monitored have a slow temporal variation as the case here reported. For this reason, in some applications, the node wake-up time for sensing can be relaxed, allowing to have greater waiting period compared to active one, which has less impact on the overall energy consumption. In Fig. 3.3 is reported the SPI data exchange between MCU, sensor and transceiver before the packets transmission, in which most of the energy is extracted from the storage capacitor  $C_s$ .

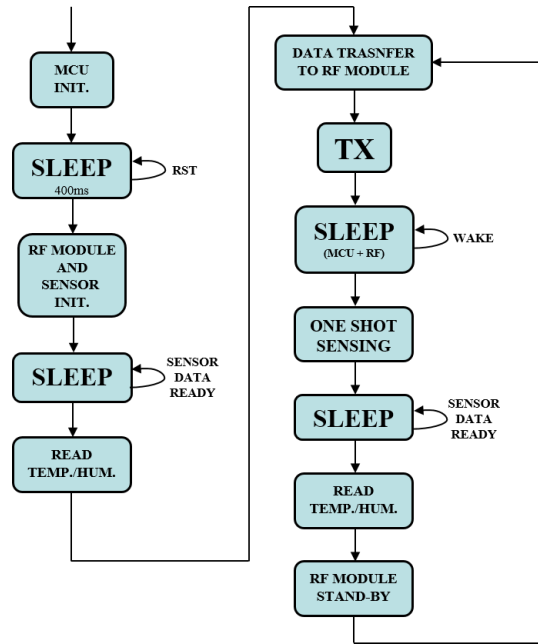


Figure 3.2: Microcontroller firmware operation.

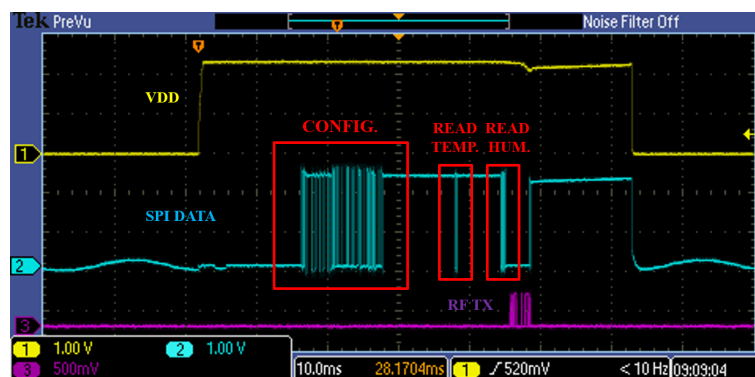


Figure 3.3: SPI data exchange followed by the RF packet transmission.

### 3.4 Load current consumption

As first test stand, It has been evaluated the current consumption of the load according to the tasks discussed in the previous Section. In particular, the measurement has been performed through a *power monitoring board (STDES-ERH001D)*, which breaks the voltage supply path for current sensing. In Fig. 3.4, the measured current consumption curve emphasizes an ultra-low current consumption (less than  $1 \mu\text{A}$ ) during deep sleep state of the MCU and the RF transceiver, allowing to store almost the overall incoming energy.

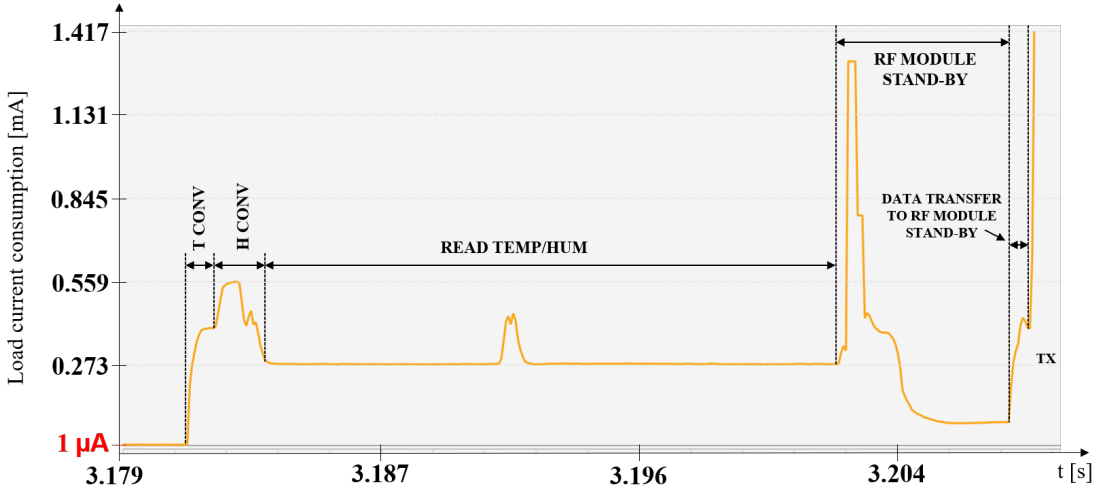


Figure 3.4: Measured load current consumption during the operation phases.

Temperature and Humidity conversion requires a high current to operate due to the acquisition circuit based on ADC converters. Higher conversion times can bring to lower current consumption and vice-versa, but from the energy budget point of view the current extracted is almost the same in both cases. The read period covers a large timing window, firstly, dedicated to SPI communication between sensor and MCU and secondly, for data processing required to get the current temperature and humidity. However, during the radio-frequency transmission the node consumes most of the energy (peak current up to 25 mA), where the storage capacitance is rapidly discharged. For this reason, it has to be calculated in order to end at least one transmission before dying, according to the total amount of energy required:

$$\Delta E = V_{DD}[(I_{TCONV}t_{TCONV} + I_{HCONV}t_{HCONV} + I_{READ}t_{READ} + I_{STB}t_{STB} + I_{TX}t_{TX})] \quad (3.3)$$

Where:

- $V_{DD}$  is set to 2.65 V as worst case;
- *Temperature conversion*,  $I_{TCONV} = 387 \mu\text{A}$  in  $t_{HCONV} = 1 \text{ ms}$ ;
- *Hyidity conversion*,  $I_{HCONV} = 559 \mu\text{A}$  in  $t_{HCONV} = 1.5 \text{ ms}$ ;
- *Reading and data processing*,  $I_{READ} = 273 \mu\text{A}$  in  $t_{READ} = 19.5\text{ms}$ ;
- *RF transceiver stand-by*,  $I_{STB} = 80 \mu\text{A}$  in  $t_{STB} = 4 \text{ ms}$ ;
- *RF transmission mode*,  $I_{TX} = 13 \text{ mA}$  (average current) and  $t_{TX} = 7 \text{ ms}$ .

Hence, the total amount of energy is  $\Delta E = 97.8 \mu\text{J}$ , while the storage capacitance required to satisfy the node operation can be computed as:

$$C_s = \frac{2\Delta E}{(V_H - V_L)^2} = 646 \mu\text{F} \quad (3.4)$$

### 3.5 Multi-source PMU

The heterogeneous multi-source energy harvesting based on buck-boost converter [171], Fig. 3.5, provides up to 9 independent input channels, of which 5 are specific for Piezoelectric transducers with Synchronous Electric Charge Extraction (SECE) interface, 2 low-voltage (LV) DC sources (100 mV to 1 V) and 2 “high-voltage” (HV) DC sources (1 V to 5 V) with a dynamic schedule based on source priority.

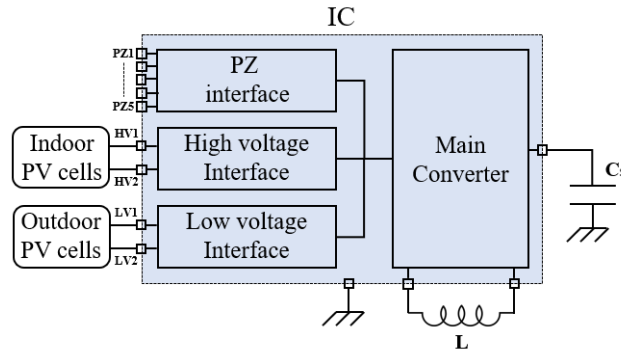


Figure 3.5: Multi energy harvesting source power conversion unit.

Moreover, the device implements the maximum power point tracking (MPPT) of the input sources, for more efficient energy extraction which is given by 65 % with LV interface and 75 % for HV interface. The main converter is able to operate,

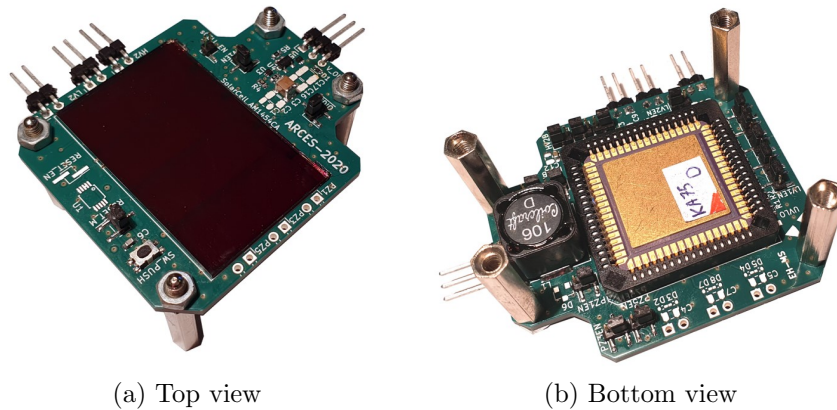


Figure 3.6: PCB design of the PV multi-source PMU with indoor solar cell.

starting from a fully discharge state of the capacitors, with a minimum input power of 770 nW provided in a single port of the low voltage (LV) interface while the output is in open circuit. However, for demanding loads, more energy harvesting sources can be applied at the same time, whose contributions are added together for higher available power and better stability.

Hence, starting from the existing multi-source converter [171], the PMU board shown in Fig. 3.6, has been designed and tested within the Thesis activities. It has been equipped with the amorphous silicon solar cell Amorton AM-1454, connected to HV DC port, which has a good response in terms of spectral sensitivity for fluorescent light in indoor environments. Amorphous-silicon (a-Si) cells provides light-sensing capabilities similar to human eyes (wavelength of 400-700 nm) and the reciprocal action between photons and silicon atoms occurs more frequently in such kind of materials rather than in crystalline silicon (c-Si), allowing more light to be absorbed.

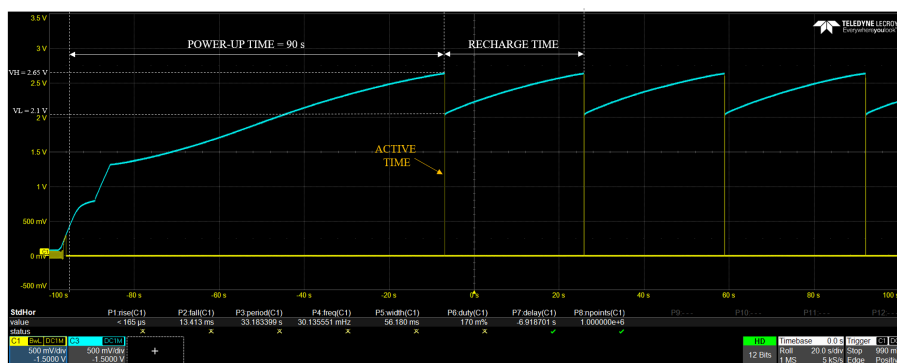


Figure 3.7: PMU Start-up and duty-cycle operation with 200 Lux of light exposure.

The node has been characterized with different light exposures, loads and storage capacitors. In particular, Fig. 3.7 highlights the start-up phase and the load power gating effect, when the tag is irradiated by 200 Lux of indoor artificial light. It is worth to notice, a power-up time of 90 s (through a storage capacitor of 646  $\mu\text{F}$  calculated in the previous Section) followed by active and re-charge periods in which the node is loaded with the circuit described in Fig. 3.1.

### 3.6 Single-source PMU

The single source DC/DC converter features an ultra-low power buck-boost converter designed in STMicroelectronics 0.32  $\mu\text{m}$  CMOS microelectronic technology [166]. The overall architecture can be divided into two main blocks: a *start-up circuit*, which allows for IC bootstrap with input sources typically providing low voltages, and the *main DC/DC converter* which also provides a fractional open-circuit voltage (FOCV) MPPT algorithm in order to adapt to the best power transfer condition. The IC dynamically decides whether to route power to the load or to a small self-supply capacitor  $C_{\text{conv}}$ : this achieves very fast activation times even in the presence of large buffer capacitors at the load output port.

When  $C_{\text{conv}}$  is sufficiently charged, all power is routed to the load. If  $C_{\text{conv}}$  get excessively discharged, all power is routed here to replenish it before the IC fails. A block diagram of the circuit IC is reported in Fig. 3.8.

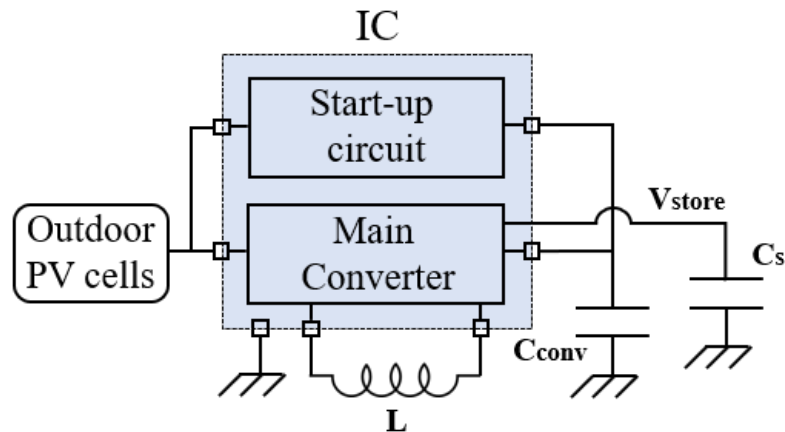


Figure 3.8: Single energy harvesting source power conversion unit.

The start-up module consists of a 16-stage charge pump implemented with low-threshold MOSFETs and driven by an internal oscillator. A minimum voltage of approximately 250 mV from the input source, is required to keep it operating.

During the start-up phase, if the minimum input voltage is guaranteed, the charge pump circuit starts working, and the output voltage on the self-supply capacitor  $C_{conv}$  is boosted. However, internal devices are not fully switched on until the output voltage gets to 600 mV, so that the output charging rate is initially limited by the sub-threshold state of the system. As soon as the generated voltage reaches 0.6 V, the start-up circuit becomes fully operational and the charge pump improves its charging rate until the output exceeds 1.36 V, which is the minimum operating voltage of the main DC/DC converter. At this point the charge pump is disabled and power conversion occurs through the buck-boost DC/DC converter. Although, the overall efficiency of the start-up stage settles between 5 % and 15 %, its sole purpose is to initially bootstrap the main DC/DC converter, so that its impact on operative efficiency can be considered negligible. Once the 1.36 V threshold is reached, an in-rush current of about 11  $\mu$ A is absorbed from the energy source by the module, for a short time to complete bootstrapping the converter functionalities. After this stage, the module can be sustained with an input power of just 935 nW showing a quiescent current of 121 nA. It is worth recalling that these values refer to the voltage on the self-supply capacitor  $V_{conv}$ . In order to extract the maximum power from the PV source, the IC adopts an FOCV MPPT technique. The input source is kept at 75 % of the open-circuit voltage of the PV cell, which actually represents the maximum power transfer condition for photo-voltaic systems. The open-circuit voltage is sampled for 2  $\mu$ s every 8 conversion cycles of the DC/DC converter. The buck-boost DC/DC converter operates in discontinuous current conduction mode and is switched when the source voltage crosses the reference MPPT voltage. The overall efficiency, highly affected by source impedance, grows from 35 % up to 75 % (respectively starting from few hundreds mV up to 1.4 V of open circuit voltage).

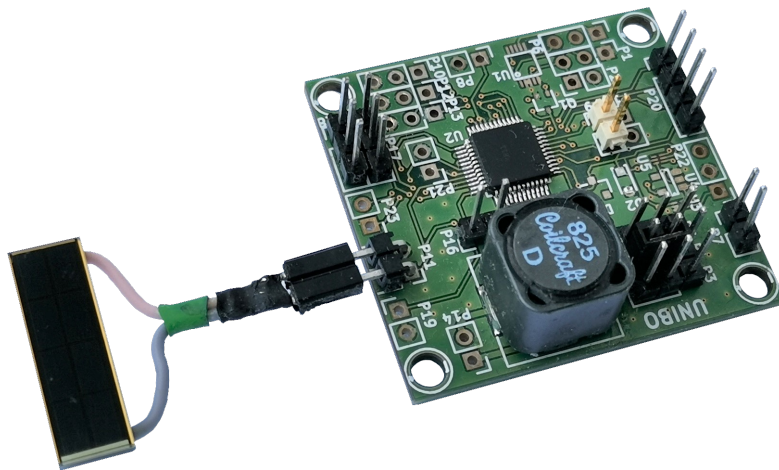


Figure 3.9: PCB design of the PV single-source PMU with outdoor solar cell.

The prototype of the single-source energy-harvesting PMU has been implemented in 4 layer FR4 PCB technology (starting from the existing single-source converter [166]) and shown in Fig. 3.9. It is equipped with a crystalline silicon solar cell (Ixys KXOB22-12X1) which has a wide spectrum sensitivity, with a peak typically located at 1000 nm of wavelength. This type of material has a lower band-gap compared to a-Si cells, allowing to have, at the same time, lower open circuit voltage (600 mV) which is perfectly matched with the adopted low-voltage input interface of the single-source main converter.

### 3.7 Experimental results

The scenario, depicted in Fig. 3.10, shows a wireless sensor network based on the presented PV battery-less tags, for both indoor and outdoor applications. The receiver chain is composed of the same transceiver placed in transmission (MRF89XA), working at 868 MHz of carrier frequency, which is driven by a Raspberry Pi 4 in charge of collecting sensing data information to make them available locally or in the cloud. The maximum working range between tags and receiver, in open field communication, is 750 m due to the high sensitivity of the RF modules (up to -113 dBm) which falls down to 80 m in indoor environments, with the presence of obstacles and walls [177]. In Fig. 3.11 an outdoor measurement campaign has been performed to evaluate the temperature and humidity during the day, where the outdoor tag solution is exposed to the natural light of the sun.

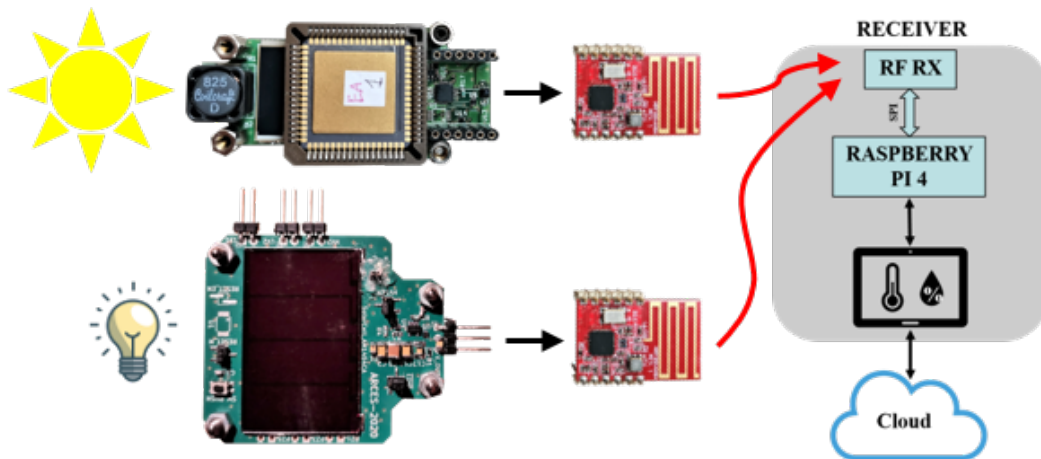


Figure 3.10: Wireless sensor network of PV passive Tags for outdoor (Top) and indoor (Bottom) applications.

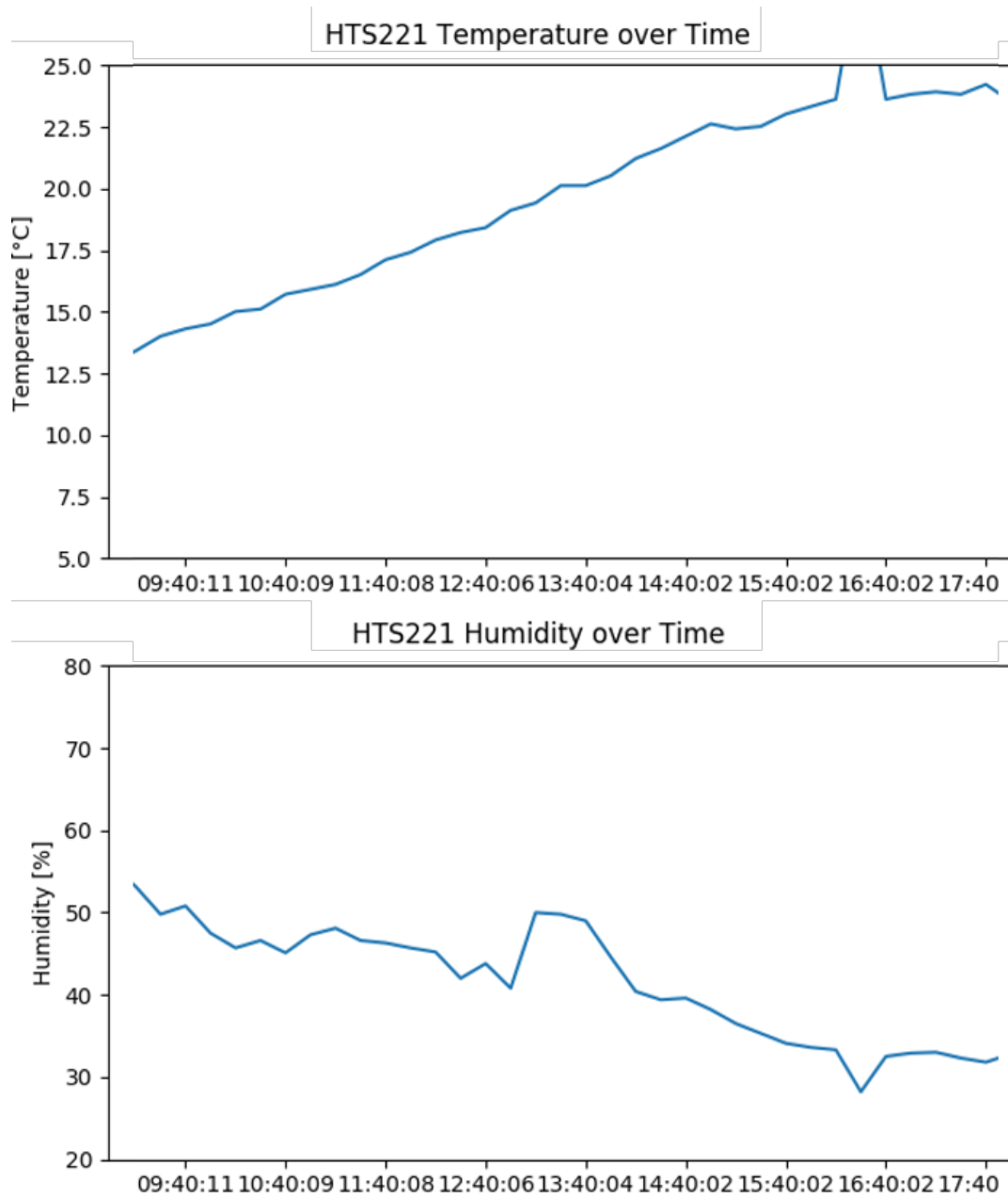


Figure 3.11: Outdoor measured temperature and humidity.



# Chapter 4

## UHF-UWB battery-less Tags for localization

### 4.1 Motivations and Requirements

The international space station represents the objective scenario by *European Space Agency (ESA)*. Due to its orbit in free fall towards the Earth, the objects fluctuate and can be easily lost. The search operations conducted by the Astronauts of subsequent missions, may even take a few hours of work to retrieve tools.

Since, the space mission costs are in the order of hundreds of millions of Euros, it is easy to imagine that the astronaut hourly cost is significantly greater compared to the human hourly cost on Earth. This fact, led ESA to request a system able to localize objects in space with precise real time positioning. They started with the use of optical systems, which have the advantage of defining the objects position accurately, but they fail with the presence of obstacles (non-line-of-sight conditions). Hence, the radio-frequency technology used for both, energy harvesting and 2D localization, has covered an important role due to its properties and abilities to work in harsh environments. Within these concepts ESA funded the project called *LOST - "Localization of Objects in Space through radio-frequency Tags"* in which the University of Bologna and the Université Catholique de Louvain, jointly participated to achieve the required objectives.

The system design starting from the tag up to the localization engine have followed the main requirements fixed by the European Space Agency which are:

- *RF tag operation in a covered area of  $10 \times 10 \text{ m}^2$  where the UHF energy showers are placed in the corners;*
- *Localization in a comparable area with centimeter level accuracy;*
- *Presence of multiple Tags;*

- High Tag read-out rate for *quasi real-time positioning*.

The presented project specifications have been very challenging, by requiring a particular attention on the implementation choices. A centimeter level accuracy for the positioning engine, can be reached through UWB-based systems which are capable of high ranging accuracy and robustness against multi-path propagation, due to the fine temporal resolution and spectral properties of UWB signals, as discussed in Section 1.4.2. On the other hand, long range tag to reader distances are satisfied only with a *micro-power Tag design* with an ultra-low power consumption, by applying the policies shown in Chapter 3. The node *minimization of energy per operation* permits to have a lower re-charge time of the storage capacitor (in a duty-cycle mode) allowing a *High refresh-rate of the position*. Moreover, the possibility to manage the *presence of multiple tags* constitutes a primary constraints. Thus, an *addressing circuitry* better defined as Wake-up Radio, is required in order to individually select the nodes. From the UWB localization point of view, the tag implementation can be based on *transmitting* or *backscattering* techniques. Since the latter has a reduced power link-budget due to the double path of the UWB signal, the usage of transmitting tag represents a good choice when large areas have to be covered, as in this particular case.

## 4.2 Single monopole Tag design

The architecture of the proposed micro-power tag is shown in Fig. 4.1 [53].

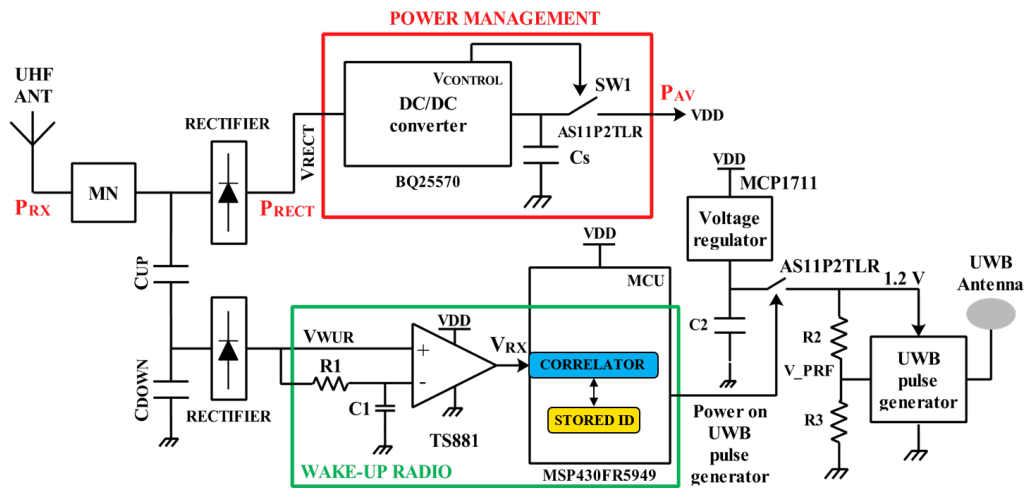


Figure 4.1: UHF battery-less transmitting tag.

The node is equipped with a single UHF monopole [178] used for both RF energy harvesting and Wake-up radio capabilities, and an UWB antenna, placed for localization purposes. The UHF path is split in two different parts, through a capacitive divider, in order to deliver most of the energy to the power management unit. The Rectenna has been developed by the group of Electromagnetic fields and used for the integration activities with the base-band circuitry, designed in this Thesis. Power incoming from the UHF port is rectified and converted into a DC form, which is managed by the on-board regulated DC/DC converter (TI bq25570), which supplies tag circuitry when sufficient power is available and performs the maximum power point tracking (MPPT) of the RF source. A small part of the rectified voltage coming from UHF link is also sent through a data slicer inspired by [125], which demodulates an on-off keying (OOK) sequence, actuated by the RF source on the UHF carrier during the addressing phase, and provides a digital version of the received address. An ultra-low power microcontroller unit (MCU) is used for basic processing, for comparing the received bit stream with the locally stored individual tag address, and for generating control signals to drive the pulses generation module. A voltage monitor, integrated in the DC/DC converter, provides and cuts power to the MCU when the harvested energy is not sufficient to sustain an entire addressing phase and UWB transmission. Moreover, additional switches are used to turn off external components in order to reduce unnecessary quiescent power consumption.

### 4.2.1 UHF front-end

A single rectenna (rectifying antenna), composed of a UHF meandered monopole (1.8 dBi of gain), is designed and tuned in the European RFID band 865-868 MHz combined with a matching network and rectifiers, Fig. 4.2.

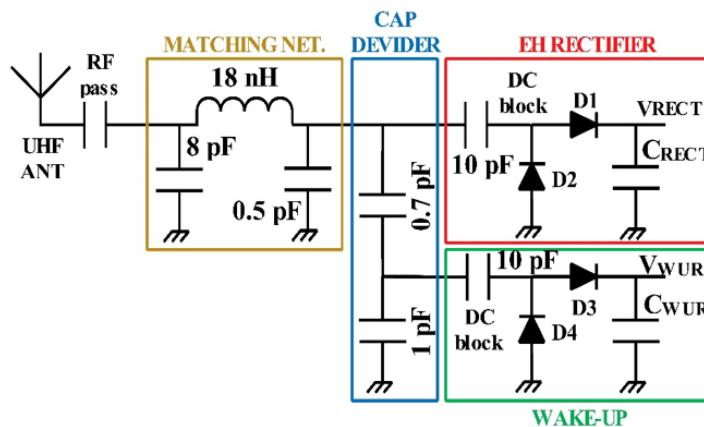


Figure 4.2: UHF dual path rectenna.

The rectenna features also a wake-up radio (WUR) implementation, without recurring to a dedicated second antenna and therefore reducing the overall tag dimensions. The input for the WUR implementation has therefore to be derived from the UHF received signal. To this extent, the most obvious solution would be that of providing an input for the WUR by splitting the dc voltage at the output of the rectifier with a conventional resistive divider. However, this solution is by definition lossy, as it involves lossy components. Given the extremely low values of power available at the high distances foreseen for the system, losing even only few  $\mu\text{W}$  of power is not acceptable. For this reason, it has been resorted to the solution presented in [116] and [178] where the voltage is split at RF level, by means of a capacitive divider. In this way, only reactive components are involved, resulting in almost no losses, except for the parasitic ones due to the non-ideal capacitors.

Through the capacitor divider, only a small portion of the received power is delivered to the WUR side, where tens of mV are enough to decode the data received. This choice, makes the entire network unbalanced to the power conversion side for more efficient energy harvesting. The rectifiers stages are based on Skyworks SMS7630-079LF Schottky diodes, with threshold voltages lower than 240 mV, specifically designed for these purposes. The dual-path rectenna has been co-designed by means of EM/nonlinear simulation in order to account for different incoming power levels and the dispersive behavior of the antenna itself [179].

In Fig. 4.3, the rectenna numerical and experimental performance are compared in terms of both the conversion efficiency and the realized DC voltage at the rectifiers outputs. In a real case scenario, in which the node is placed at several meters from the transmitter, a received power on the tag side, can be easily lower than -15 dBm by providing a rectified voltage of 800 mV besides a conversion efficiency of 30 %.

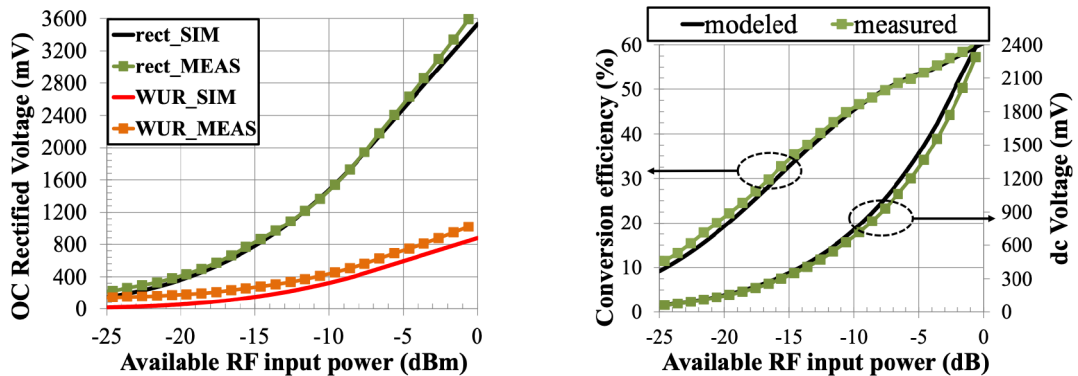


Figure 4.3: Rectenna conversion efficiency and rectified voltage as function of the received power.

### 4.2.2 Tag operation

The heart of the tag is the low power MCU (TI MSP430) that manages the modes of operation of the entire circuit. In particular, the MCU starts in a *LISTENING phase*, in which it works with a very-low-power low-frequency internal oscillator (VLO) and waits for the wake-up address to be sent by the UHF source. In this phase, the CPU is off and only the on-chip peripherals are clocked by the VLO, in order to save power. The bit-stream received from the UHF antenna is filtered and converted to digital voltage levels by the data slicer circuit, before being processed by the on-chip UART module of the MCU. When all the serial bits are received (8 data bits, 1 start bit and 1 stop bit with a data rate of 2.2 bit/sec), the CPU is woken up by an interrupt issued by the UART peripheral (*ADDRESSING phase*), and the address is software-decoded and compared with the tag address stored in the Flash memory of the MCU. The bits can also include redundancy for increased robustness. During this phase the mode of operation changes into *active mode* and a higher-frequency internal clock (DCO - Digitally Controlled Oscillator) is enabled, which makes the MCU more responsive.

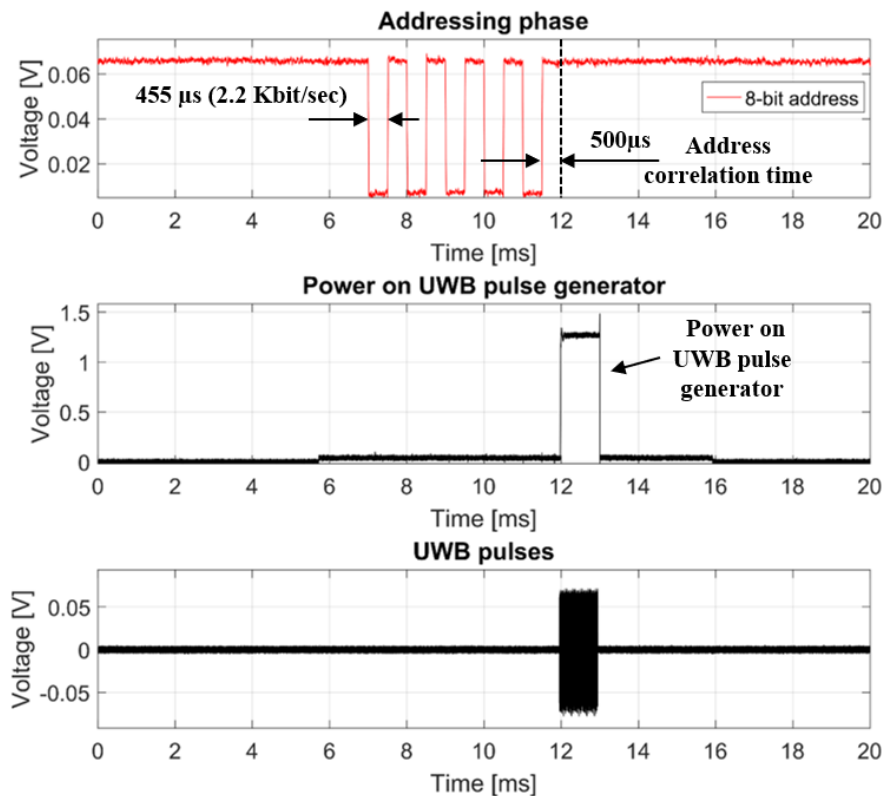


Figure 4.4: UHF-UWB passive Tag operation.

Once the tag address is recognized, the microcontroller provides the signals used to power on the external UWB module to generate a pulses sequence (*UWB LOCALIZATION phase*) before entering in LISTENING phase for the next interrogation, Fig. 4.4.

The UWB pulses generator is supplied at 1.2 V by a linear regulator enabled by the MCU through an analog switch. The voltage  $V_{PRF}$ , tunable with a resistive divider, modulates the UWB pulse repetition frequency. The IC [78] is based on a 65 nm CMOS technology and includes a voltage controlled ring oscillator, a buffer and a pulse shaping filter.

### 4.2.3 Design Trade-off

The best trade-offs with performance and low power consumption were pursued. The possibility to choose between different low-power modes and clock sources made the TI MSP430 microcontroller a reasonable choice. In particular, during the addressing phase a *slow data processing* has been implemented. The MCU works in deep sleep LPM4 (Low Power Mode 4) which consumes only 400 nA due to the VLO oscillator of 10 KHz used to serve the Universal Asynchronous Receiver/transceiver Peripheral (UART). In this solution, the very low power comparator TI TLV3691, with 75 nA of quiescent current, is suitable to process a slow data stream at few Kbit/sec. The data-rate has to be chosen according to the maximum propagation delay offered by the comparator (45  $\mu$ s), thus, lower than 20 KHz as upper bound. Moreover, since the UART module of the MCU is clocked with a time period of 100  $\mu$ s, the peripheral interface can process only data with a frequency smaller than 5 Kbit/sec. Hence, a complete address acquisition can be reached in 4.55 ms (with 2.2 Kbit/sec). The comparison of the address bits is executed in *ACTIVE* mode at a frequency of 1 MHz (DCO) in order to reduce the computation time. Concerning the application, this solution represents a good choice for very low power consumption. Where a higher data rate is required, in order to waste as little energy as possible, a *fast data processing* can be chosen and all operation are performed at higher MCU frequency, by considering a comparator with lower propagation delay as LPV7215 from TI. Hence, the higher power consumption of the last solution can be partially compensated with a smaller computational time, for an almost constant Energy budget. Moreover, a MCU offers greater flexibility with respect to custom logic and, most importantly, still a significantly lower energy consumption compared to available dedicated wake-up Radios (as AS3930 from AMS). A technique for further reducing system power consumption consists in switching off all unnecessary devices during their idle time. Hence, it becomes convenient to use analog switches to turn off the UWB pulse generator when not used.

#### 4.2.4 Power management unit

The rectified voltage of the UHF antenna is provided as input of the DC/DC converter TI bq25570, which is specifically designed to efficiently acquire and manage the micro-watts of power generated from a variety of DC source, Fig. 4.5.

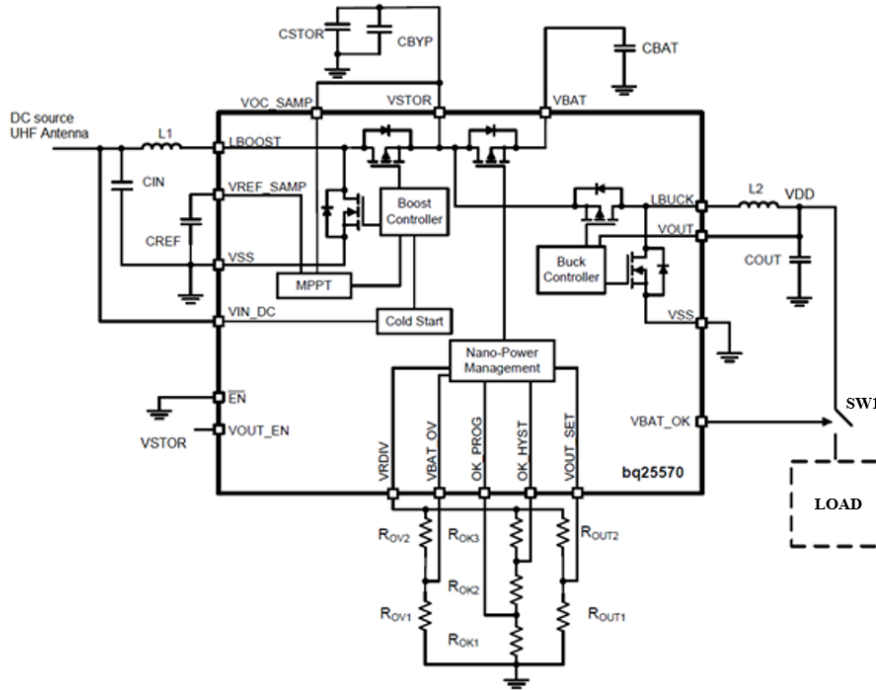


Figure 4.5: TI bq25570 power management unit configuration scheme.

Basically, the energy harvesting starts with a low efficient and unregulated charge pump, where the minimum voltage of 330 mV is required as input in order to get 1.8 V on *CSTOR* capacitance. After the cold-start phase, the *VSTOR* is in short circuit with *VBAT* and the main boost converter is enabled to increase it until the over-voltage protection, which is chosen to be  $VBAT_{OV} = 2.8$  V. Subsequently, a buck converter has to provide a regulated output voltage at the desired value ( $V_{out} = 2.3$  V), which is set externally. A maximum power point tracking is implemented in order to maximize the power extracted from the energy harvesting source. In particular, the boost charger indirectly modulates the input impedance of the main converter by regulating the input voltage. It is sensed by the *VIN\_DC* pin and the sampled reference voltage is stored on the *VREF\_SAMP* pin. The MPPT circuit obtains a new reference voltage every 16 s, by periodically disabling the charger for 256 ms and sampling a fraction of the open-circuit voltage (for radio-frequency sources the maximum power point is typically 50 % of the  $V_{oc}$ ). The power supply to the load is controlled by the *VBAT\_OK* signal which is

high when the  $V_{BAT}$  voltage is in a certain range defined by the lower threshold  $V_{BAT_{LOW}} = 2.2$  V and upper threshold  $V_{BAT_{HIGH}} = 2.4$  V. The voltage monitor behaviour and all thresholds can be set and modified through external resistors dividers. In particular, to properly set the over-voltage threshold, the resistors  $R_{OV1}$  and  $R_{OV2}$  are calculated, according to  $RSUM_{OV} = R_{OV1} + R_{OV2} = 10$  M $\Omega$ , through the following expression:

$$R_{OV1} = \frac{3}{2} \frac{RSUM_{OV} V_{BIAS}}{V_{BAT_{OV}}} = 6.48 \text{ M}\Omega \quad (4.1)$$

Where  $V_{BIAS} = 1.21$  V is the internal reference for the programmable threshold voltages. Hence,  $R_{OV2} = RSUM_{OV} - R_{OV1} = 3.52$  M $\Omega$ . In order to evaluate the  $V_{BAT}$  hysteresis, the total resistance to ground is set to be  $RSUM_{OK} = R_{OK1} + R_{OK2} + R_{OK3} = 10$  M $\Omega$ , while:

$$R_{OK1} = \frac{V_{BIAS} RSUM_{OK}}{V_{BAT_{HIGH}}} = 5.04 \text{ M}\Omega \quad (4.2)$$

$$R_{OK2} = \left( \frac{V_{BAT_{LOW}}}{V_{BIAS}} - 1 \right) R_{OK1} = 4.3 \text{ M}\Omega \quad (4.3)$$

Thus,  $R_{OK3} = RSUM_{OK} - R_{OK1} - R_{OK2} = 625$  k $\Omega$ . On the other hand, the resistors used to set the output voltage can be computed, by knowing the sum of resistors  $RSUM_{OUT} = R_{OUT1} + R_{OUT2}$ , as:

$$R_{OUT1} = \frac{V_{BIAS}}{V_{OUT}} RSUM_{OUT} = 5.26 \text{ M}\Omega \quad (4.4)$$

And so,  $R_{OUT2} = 4.74$  M $\Omega$ .

No MPPT resistors are required, because  $VOC_{SAMP}$  can be tied to ground, to obtain the 50 % of the open circuit rectified voltage. It worth to mention that, some of the calculated values have been modified by considering a variation of 1 % according to the commercial components available in the markets. As best trade-off between fast charge time, during the cold start, and correct implementation of the MPPT, the input capacitance is selected to be the minimum recommended value of 4.7  $\mu$ F. Since the main converter is used for battery-less applications, on the  $V_{BAT}$  port, the absence of a battery, is compensated with the presence of a capacitor of 15  $\mu$ F, slightly higher than the storage capacitor on  $V_{STOR}$  ( $C_{STOR} = 4.7$   $\mu$ F). The current through the LBOOST inductor (L1) is controlled with an internal current sense circuit and incremented in order to maintain high efficiency of the charger across a wide input current range. The inductor's saturation current should be at least 25 % higher than the expected peak currents recommended. Hence, in the case of the boost charger, an inductor  $L1 = 22$   $\mu$ H has been chosen to have a peak current greater than 300 mA. Instead, for the buck converter the peak current capability should be greater than 200 mA, achievable with an inductor  $L2 = 10$   $\mu$ H.

### 4.2.5 PMU validation test

The power management unit has been evaluated with the test bench proposed in Fig. 4.6, in which the rectenna is modeled through a voltage generator in order to represent its open circuit voltage, followed by a series resistance of  $10\text{ k}\Omega$  defined to be the output resistance of the rectifier stage.

As it is possible to notice in Fig. 4.7, when a sufficient rectified voltage is applied, the charge pump stage starts slowly to increment the storage voltage  $V_{storage}$  up to  $1.8\text{ V}$  (with a minimum input power of  $15\text{ }\mu\text{W}$ ) where the main converter starts to operate following the MPPT of the input source, Fig. 4.8.

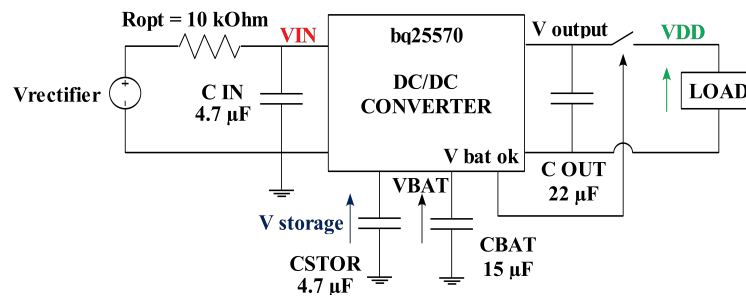


Figure 4.6: Test scheme for power management unit characterization.

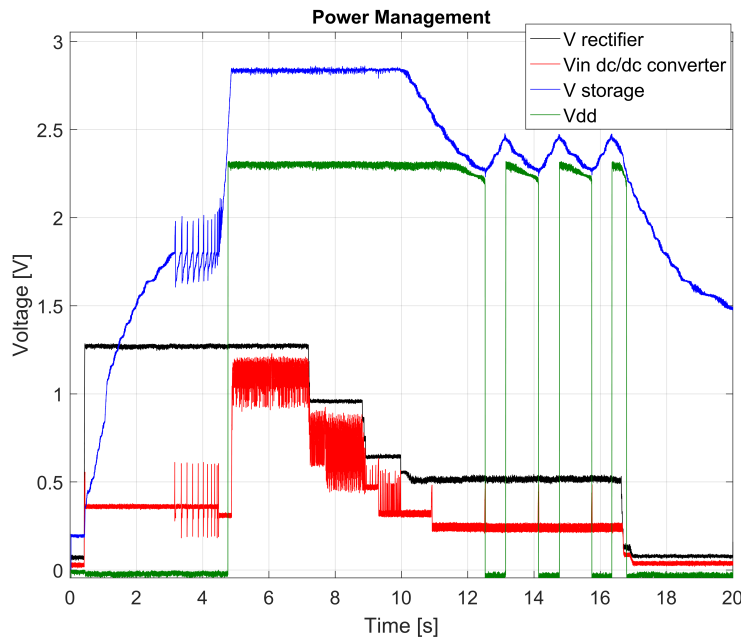


Figure 4.7: TI bq25570 PMU operation.

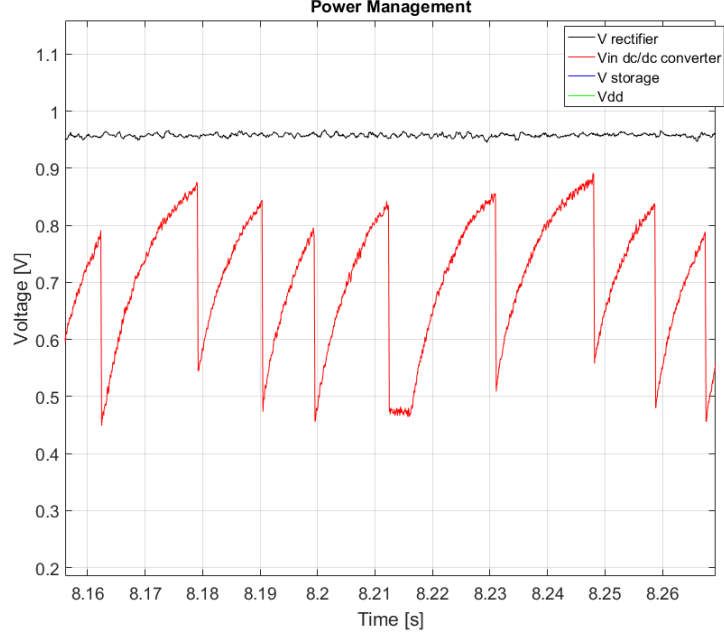


Figure 4.8: Maximum power point tracking (MPPT) of 50% of the input source, represented with a *red* color, while the rectified voltage is in *black*.

Then,  $V_{rectifier}$  has been decreased down to the duty-cycle operation of the node in which the load power is controlled by  $VBAT_{OK}$  signal, within the defined upper and lower threshold voltages.

#### 4.2.6 Energy budget

The tag operation is the direct consequence of the power management choices, according to the energy consumption [115]. The available power on the load side ( $P_{AV}$ ), represented in Fig. 4.1, can be computed as:

$$P_{AV} = \alpha P_{RECT} \quad (4.5)$$

where  $P_{RECT} = \eta P_{RX}$  is the input power of the DC/DC converter ( $\alpha$  its efficiency) while  $\eta$  is the rectified efficiency.  $P_{RX}$  represents the incoming power received by the node. It can be easily computed through the Friis formula extrapolation which is a good approximation in free space environments. The total amount of energy spent for a single interrogation can be defined as:

$$\Delta E = E_{START} + E_{IDLE} + E_{UART} + E_{DEC} + E_{PULSE} \quad (4.6)$$

in which:

- $E_{START} = 391 \text{ nJ}$  is the power-up energy;
- $E_{IDLE}$  is the energy required in waiting mode for an addressing phase;
- $E_{UART}$  is the energy spent during the address acquisition;
- $E_{DEC}$  is the energy lost during the address decoding;
- $E_{PULSE}$  represents the energy for the pulses generation sequence.

The explanation of the all parameters used for Energy-budget considerations are listed in Tab. 4.1. The energy spent by the UART interface to collect the incoming data is calculated to be  $E_{UART} = V_{DD}I_{UART}N_{BIT}T_{BIT} = 570 \text{ pJ}$  which contribution is significantly lower compared to the others, and can be neglected. When the identification number has been received, the MCU goes into ACTIVE state for the addressing comparison procedure, where the energy is:

$$E_{DEC} = V_{DD} T_{DEC} (I_{COMP} + I_{ACT}) = 115 \text{ nJ} \quad (4.7)$$

If the local address of the tag matches with the received one, Fig. 4.9, the UWB transmission is activated. The generator's energy consumption is close to 1.5 pJ per pulse with a typical PRF of approximately 200 MHz for a current consumption around 160  $\mu\text{A}$ . The energy used during this phase is given by:

$$E_{PULSE} = T_{PULSE}[V_{DD}(I_{COMP} + I_{ACT} + I_{REG}) + V_{REG}I_{PULSE}] = 424 \text{ nJ} \quad (4.8)$$

After the first power-up, the node is in IDLE mode waiting for an addressing phase. For a scenario based on one Tag operating in continuous mode, with an interrogation frequency of  $f_{READ} = 1 \text{ Hz}$ , the energy used in the listening phase is:

$$E_{IDLE} = V_{DD}(I_{COMP} + I_{SLEEP})\left(\frac{1}{f_{READ} - N_{BIT}T_{BIT} - T_{DEC}}\right) = 1.1 \text{ uJ} \quad (4.9)$$

It worth to mention that, the power management unit has an intrinsic quiescent power consumption given by  $P_Q = V_{STOR}(I_Q + I_{SW}) = 1.5 \text{ }\mu\text{W}$  which has to be guaranteed in order to keep the tag energized. In the case of unidentified tags, Fig. 4.10, only the address decoding phase is performed before to get back in sleep mode. Starting from the calculated energy  $\Delta E = 2.03 \text{ }\mu\text{J}$ , the minimum recommended storage capacitor is given by:



Param.	Value	Explanation
$I_Q$	450 nA	DC/DC quiescent consumpt.
$I_{SW}$	100 nA	SW1 current consumpt.
$I_{COMP}$	75 nA	TLV3691 current consumpt.
$I_{ACT}$	100 $\mu$ A	MSP430 Active mode
$I_{SLEEP}$	400 nA	MSP430 Sleep mode
$I_{PULSE}$	160 $\mu$ A	UWB IC current consumpt.
$I_{UART}$	5.5 $\mu$ A/MHz	UART interface current consumpt.
$T_{DEC}$	500 $\mu$ s	Address decoding time
$T_{PULSE}$	1 ms	Pulses generation time
$V_{DD}$	2.3 V	Load power supply
$V_{STORE}$	2.8 V	Voltage on $C_{STOR}$ capacitor

Table 4.1: Main parameters for power management considerations.

### 4.3 Orientation-independent Tag design

The aim of this activity is to integrate the base-band circuit designed in [53][54] with the multi-element antenna presented in [55], for an enhanced hardware architecture, specifically developed to overcome issues related to the tag orientations, besides improving the system stability and the rectifier available power for wider working distances. The scheme of the proposed passive tag is depicted in Fig. 4.11 [180].

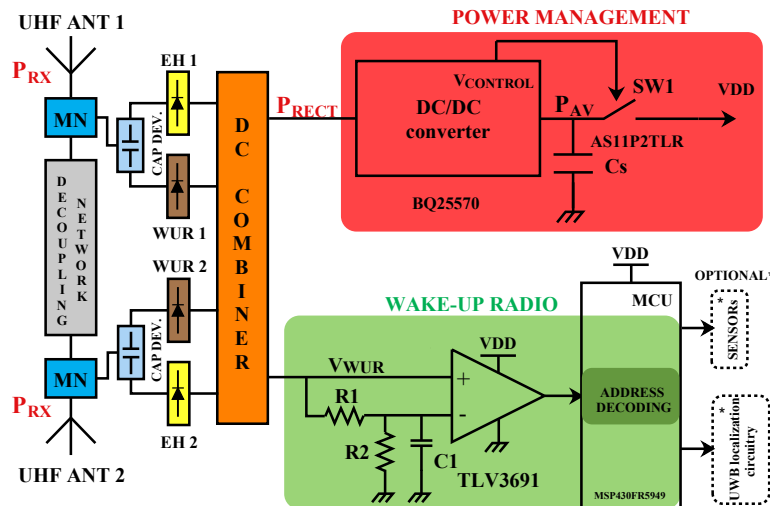


Figure 4.11: Double-monopole Tag hardware architecture [180].

It is based on two UHF meandered monopoles, combined with a matching and decoupling network studied to maximize the rectified power, firstly, for energy harvesting and secondly for Wake-up radio purposes. Even in this case, the double-monopole rectenna has been developed by the group of Electromagnetic fields, subsequently used for the integration activities with a power management unit, Wake-up radio and localization circuits.

### 4.3.1 Double-monopole rectenna

The rectifying antenna (rectenna) part of the tag is a delicate design task, especially if UHF frequency is involved, thus forcing large footprint to the radiating section. This is true for tags that usually need for compact size, in particular when the number of adopted antennas is greater than one, where an orientation-independent behavior of the rectenna is envisaged [55]. Fig. 4.12 shows the schematic view of the double rectenna architecture: two meandered monopoles with orthogonal orientation are used as receiving antennas, hence able to capture any polarized incoming field.

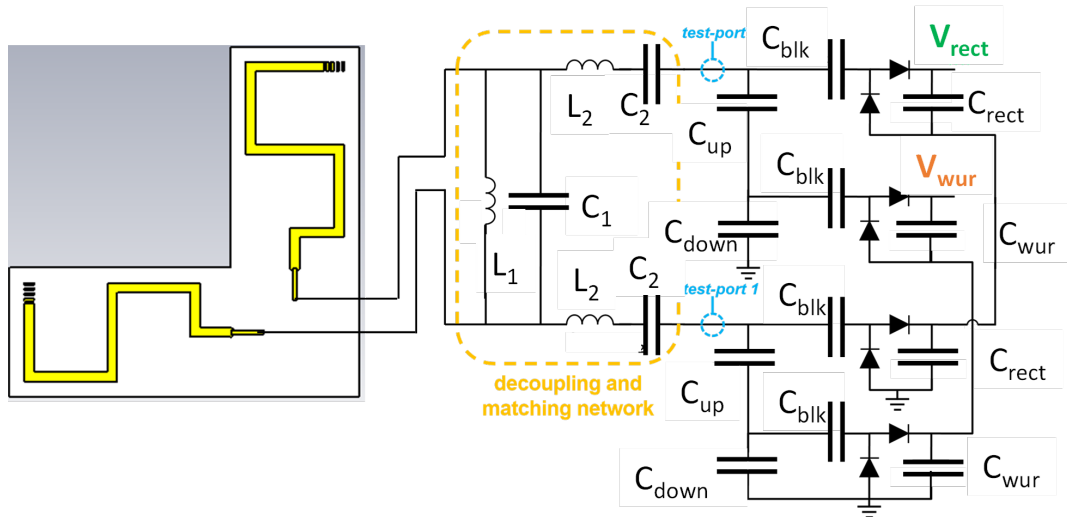


Figure 4.12: Schematic view of the double-monopole rectenna [180].

$L_1$	56 nH	$C_1$	2.8 pF
$L_2$	27 nH	$C_2$	39 pF
$C_{up}$	0.7 pF	$C_{down}$	1 pF
$C_{blk}, C_{rect}, C_{wur}$	10 pF		

Table 4.2: Lumped components values.

The most interesting feature of the radiating part relies on the close proximity of the two antennas ( in order to maintain the overall tag dimension within  $9.5 \times 9.2 \text{ cm}^2$ ): for energy harvesting purposes, it is important to guarantee an omnidirectional behavior of the two rectennas, and this is obtained by including a lumped element network, in between antennas and rectifiers, acting both as a matching and as a decoupling network. The effectiveness of the decoupling network is numerically demonstrated in Fig. 4.13, where the radiation pattern of the horizontal monopole is shown, in absence (Fig. 4.13(a)) and in presence (Fig. 4.13(b)) of the decoupling network: in the second case, the radiation pattern is almost undistorted, showing that the monopole is radiating as if it were isolated from the other monopole. Moreover, the effects of the electromagnetic coupling are not only related to the radiation properties (shown in Fig. 4.13), but also to the signal distribution in the circuit, which is definitely unpredictable.

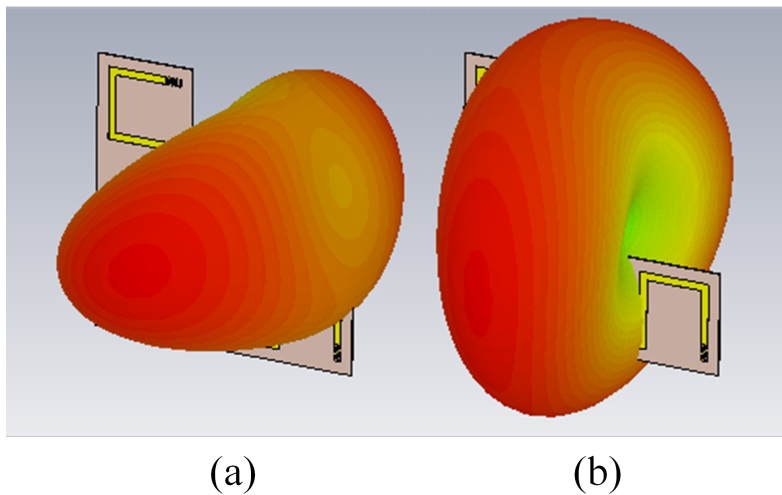


Figure 4.13: Radiation pattern of the horizontal monopole: (a) in absence, (b) in presence of the decoupling network [180].

Another distinctive feature of the tag under test is represented by the dual path rectifying section (for both antennas). There are two voltage doublers (with Skyworks SMS7630 Schottky diodes) derived in parallel from the decoupling network path: one provides the main rectifying operation, the other spills a small portion of the signal for WUR operation. The signal splitting is made more effective by resorting to a fully-reactive partition network (with  $C_{up}$  and  $C_{down}$  capacitors) that guarantees almost no losses if compared to a resistive one. The two rectenna outputs are then combined in series to maximize the overall rectified voltage. Tab. 4.2 reports the values of the lumped components of the schematic shown in Fig. 4.12.

The main goal when designing the rectifying section has been to maintain the

highest main rectified voltage ( $V_{rect}$ ) when changing, as in real operating conditions, the load offered by the WUR: if the available input power provided to a single-monopole is -13 dBm and the WUR load changes from 0.1 to 100 k $\Omega$ ,  $V_{rect}$  remains around 900 mV.

## 4.4 Test bench for measurements

In order to evaluate the performance of the tags presented in this Chapter, a test bench for measurements has been prepared mainly for managing the *wireless power transfer (Energy shower)* and *addressing phases* of the nodes, Fig. 4.14.



Figure 4.14: Test bench for measurements.

It includes a *control interface (CI)* which defines all protocol timings and digital data used in order to issue the OOK base-band signal used for the addressing phase. The control interface has been implemented through a Raspberry Pi 3 embedded platform in which is run a C++ code in charge to define:

1. the *address data-rate and timings* according to the user choice;
2. enables the *continuous wave* transmission used to energize the nodes;
3. issues external *triggers* for localization purposes and tests

Hence, all the outputs are released through the GPIOs ports, with a temporal jitter lower than 400 ns, making this platform suitable even for fine synchronization of external boards. For a simplified system control operation, a custom Graphical User Interface (GUI) has been developed in MATLAB, Fig. 4.15. It communicates with the *Control Interface* through Undefined Datagram Protocol (UDP) packets based on API commands for setting:

1. the tags *identification number*;
2. transmission *data-rate*;
3. *parameters* for localization purposes.

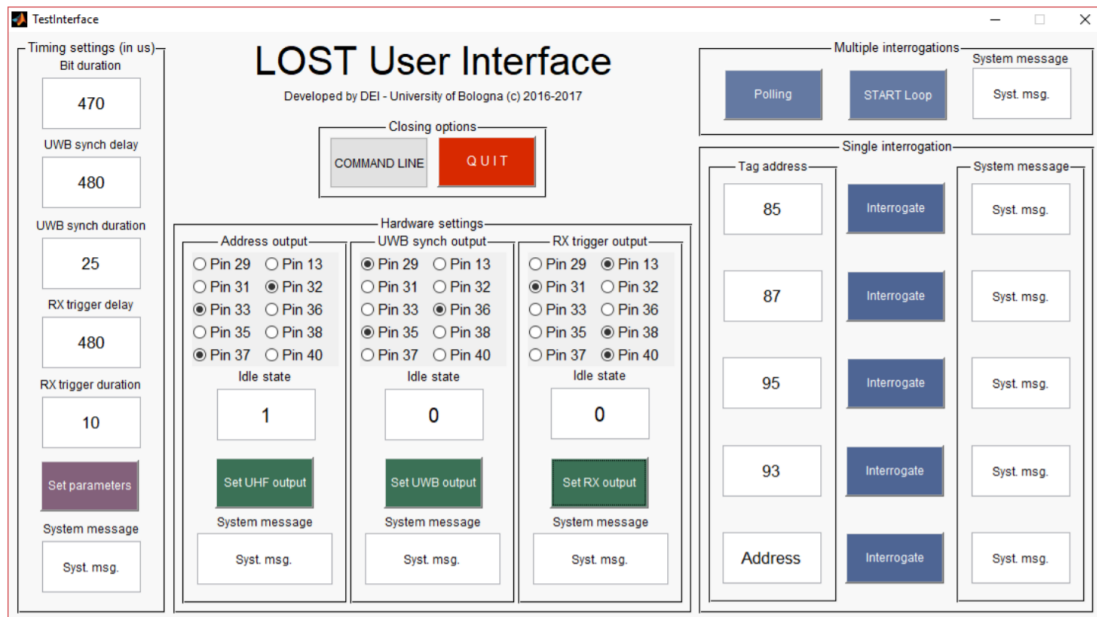


Figure 4.15: Graphical User Interface for Tag identification.

Moreover, it is possible to set a tag interrogation loop which periodically identify the nodes in order to evaluate the maximum read-out rate as a function of the distance from the transmitter.

The baseband OOK signal, coming from the Control Interface, is connected to the modulation input of the *Wireless Power Transfer Unit* (realized with the collaboration of UCLouvain) shown in Fig. 4.16 and 4.17.

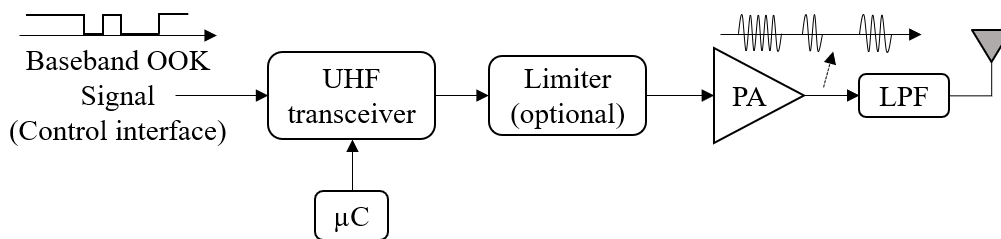


Figure 4.16: Wireless power transfer hardware scheme.

The first block is represented by the *UHF generator* which can be implemented with the RFM23BP board from HOPERF Electronic or the well known STM SPIRIT 1 embedded in STEVAL-IKR002V4D board. In order to avoid harmonic distortion coming from the UHF generator, the transmission power was set to (+10 dBm). A *microcontroller unit* (Nucleo board STM32F303F8T6) permits to configure the UHF transmission parameters in terms of frequency modulation and

power range. Hence, an optional limiter has been introduced after the generator to prevent damage to the power amplifier input (RF6886 from RFMD), which is in charge to increase the power according to the UHF antenna gain. Then a low pass filter insures harmonic rejection coming from both UHF generator and power amplifier. Finally, the signal reaches the antenna (ARRSN5 or ARRTN5 from Abracon Technology). Those antennas were chosen for their low directivity and circular polarization, ensuring the proper Energy Shower functionality. The resulting signal is a 2 Watt Effective Radiated Power (ERP) signal at 868 MHz, considering that the gain of the antenna balances the cable and filter losses.

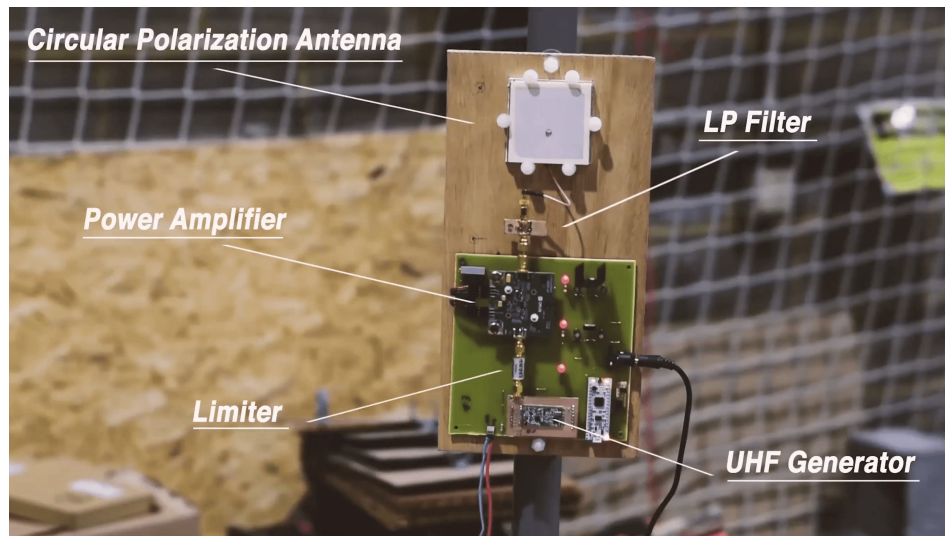


Figure 4.17: UHF wireless power transfer PCB board (realized within the collaboration activity with UCLouvain).

## 4.5 Tags performance

The characterization of the presented RF-based Energy Autonomous tags, executed with the test bench depicted in Fig. 4.14, is performed, firstly, by evaluating the achievable *working distances* between the nodes and the UHF transmitting source and secondly, the performance parameters defined as:

- *Node sensitivity*: It is the minimum received power which guarantee the first start-up of the node in order to accomplish both, energy harvesting and demodulation of the incoming identification bits.
- *False ID-rates*: It represents the number of identifications that occur when the received address does not match with the tag identifier.

- *Missed ID-rates*: It defines the number of identification lost, even if an addressing phase has been performed by the radio-frequency source.
- *Maximum ID-rate*: It is the maximum number of identifications that can be managed by the node (expressed as a function of seconds or minutes.)

### 4.5.1 Single-monopole

The prototype board has been built-in a low-losses 0.5 mm Rogers RO4350B RF substrate with 4 layers PCB technology, Fig. 4.18, which represents a compact-sized solution with all hardware blocks presented in Fig. 4.1.

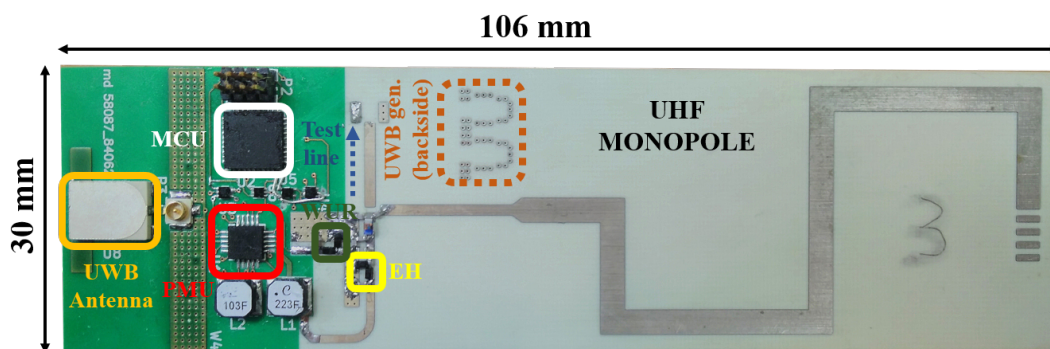


Figure 4.18: PCB design of the single-monopole tag.

As shown in Fig. 4.19, at the first power-up, the tag was brought in a fully discharged state of the storage capacitors, at high distances from the energy shower, and was slowly moved closer towards the UHF source, until it was able to complete in 2 minutes its power-up sequence at 9,7 m, as *first activation*, with a *sensitivity* of -13 dBm.

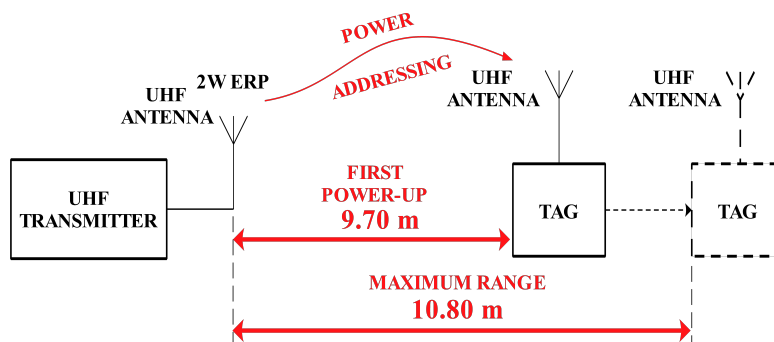


Figure 4.19: Working distances of the UHF single monopole tag.

In the same position, the performance ensures a maximum activation rate of 8 Hz and a missed activation rate of 7 %. At this stage, the distance was increased again until the tag stopped operating where no sufficient power is received, in order to energetically sustain the load (10.8 m as *maximum working distance*).

However, due to the linear polarization of the rectenna, the capability to efficiently receive just a portion of the incoming signal is limited. Hence, the tests have been conducted in the best case with a perfect alignment between tags and UHF source.

### 4.5.2 Double-monopole

As a preliminary test the double-monopole tag (low losses Rogers RO4350B PCB design shown in Fig. 4.20), has been compared with the single-monopole one by measuring the open-circuit rectified voltage at their dc output ports.

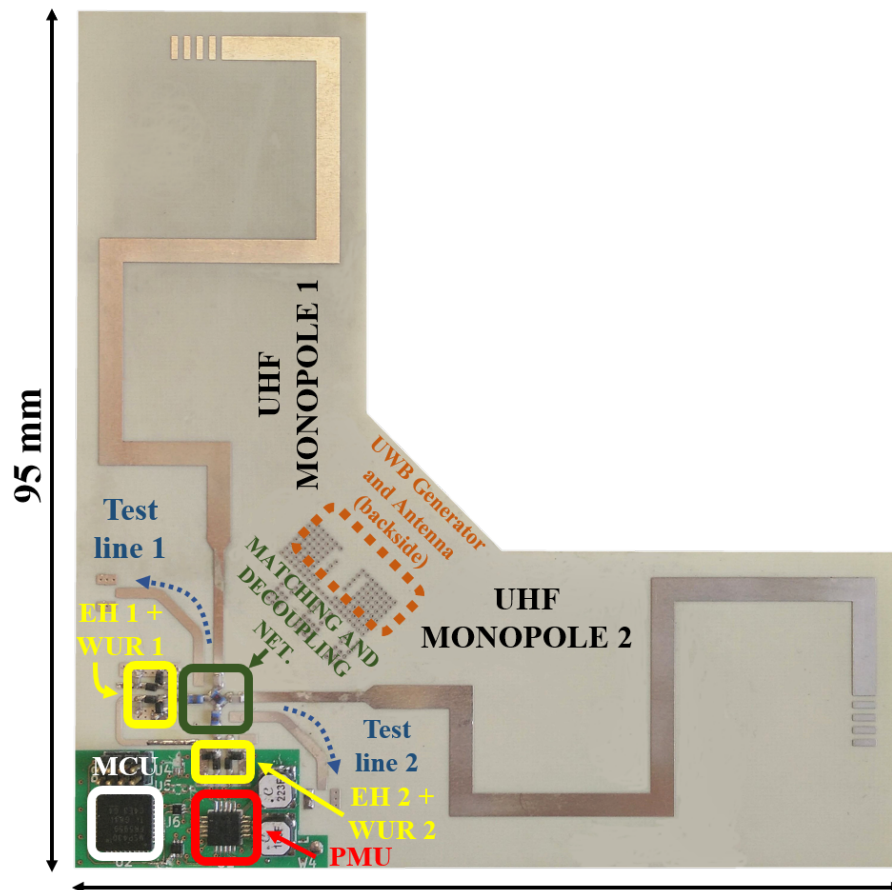


Figure 4.20: PCB design of the double-monopole tag.

A circularly-polarized patch antenna sends a UHF power corresponding to -13 dBm in the rectennas location: in this way, each monopole receives -16 dBm. The rectified voltages for two representative orientations are: 400 mV in a vertical orientation for the single-monopole and 930 mV for one of the double-monopole case (V), an oblique orientation corresponding to a 45° right rotation brings to have respectively 320 mV and 915 mV (O). More than double rectification is achieved in both cases by the multi-rectenna architecture.

Even in this case, to characterize the tag performances the double-monopole battery-less node is placed away from the transmitter and progressively closer and closer until the main energy converter is powered up, starting from a fully discharge state (first activation at 12 m). Once activated, the node can operate at higher distances up to 21.9 m (with an activation rate of 2 times per minute) as maximum distance from which the DC/DC converter has not enough input power to operate.

The activation rate, reported in Tab. 4.3, decreases with the square of the distance (as Friis formula) and shows a saturation up to 6 m of 198 wake-up per second. Since an addressing phase is ended in 5.05 ms (address acquisition and computational time), the data-rate of 2.2 Kbit/sec adopted to identify a tag sets the limit on the maximum number of activations per second.

The tag has been tested in different orientations, with steps of 45°, where no significant performance differences have been recorded, by confirming an orientation-independent behavior of the node in the reported results. A comparison between the single and double-monopole tags solution is presented in Fig. 4.21. The rectified power, obtained with Friis formula extrapolation, as a function of the distance, confirms the wider range of the double-monopole. Since the real measurements of the working distances are taken in indoor environment, they are affected by multipath propagation of the RF signals. Hence, the extrapolated received power, on the activation and max range tag positions, in addition of being an approximation, it can be slightly different compared with the real received one during the measurement, due to the indoor channel properties.

<b>D[m]</b>	<b>2</b>	<b>4</b>	<b>6</b>	<b>8</b>	<b>10</b>	<b>12</b>
<b># act</b>	198/sec	198/sec	198/sec	152/sec	92/sec	56/sec
<b>D[m]</b>	<b>14</b>	<b>16</b>	<b>18</b>	<b>20</b>	<b>21.9</b>	<b>22</b>
<b># act</b>	30/sec	16/sec	8/sec	3/sec	2/min	

Table 4.3: Tag activation rate as a function of the distance.

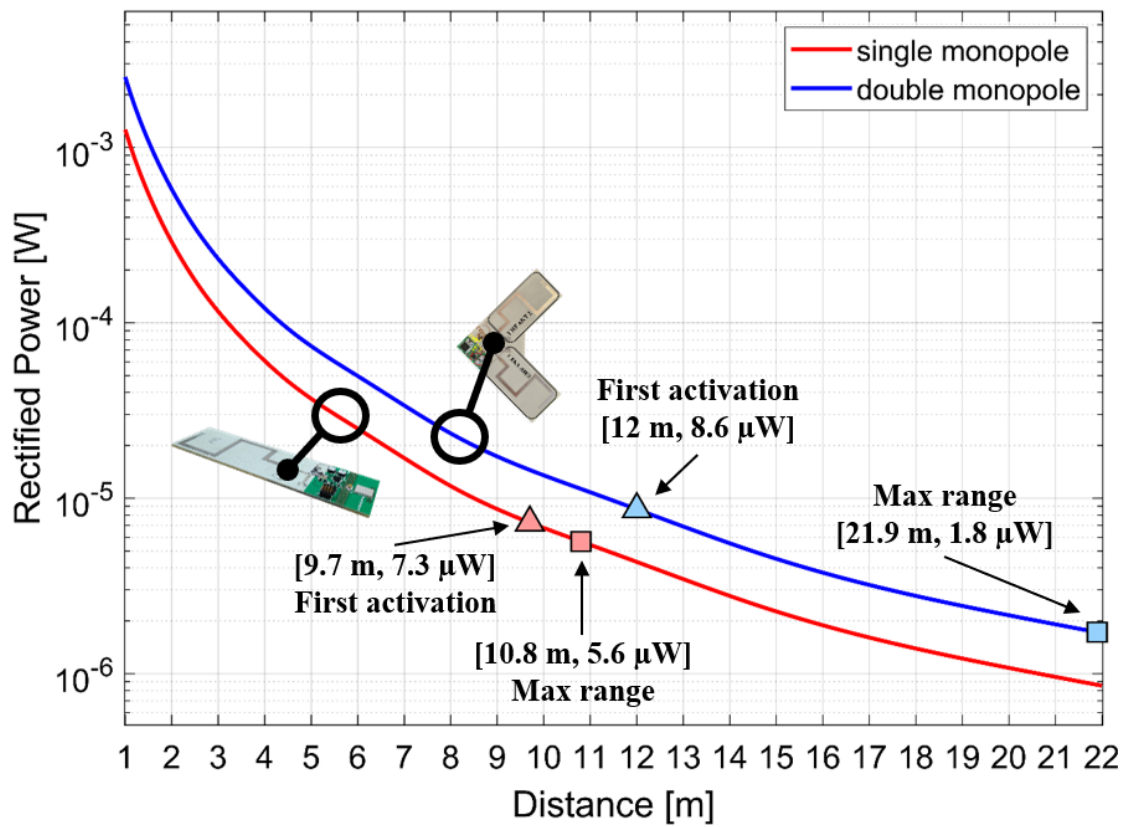


Figure 4.21: Comparison between single and double-monopole working distances.

# Chapter 5

## Enhanced RFID with localization capabilities

### 5.1 Motivations

The solutions presented in the previous Chapter are based on an OOK custom protocol for UHF reader to tag communications, which provides good performances in terms of node power consumption, but it is not compliant with the current standards, by reducing the possibility of its usage in the market. Hence, this Chapter presents the design updates based on [53] in a new solution [54] able to operate at long read-range distances compliant with the EPC Gen. 2 Class 1 regulation, provided by the European Telecommunication Standard Institute (ETSI) and fully working within 865-868 MHz frequency band. The obtained performances are comparable with integrated solutions available in the market and in academy, albeit the RFID protocol is still firmware implemented in a microcontroller as it has been in the WISP project [181]. The system is easily programmable and maintains high flexibility, allowing operation at a low level within the execution of the protocol phases.

### 5.2 UHF-RFID tag implementation

The hardware architecture of the proposed passive sensor tag is depicted in Fig. 5.1. The node is based on a single UHF monopole rectenna, presented in the previous Chapter, used for both RF energy harvesting and Wake-up radio capabilities. On the RF side, a very limited part of the incoming power is rectified to provide wake-up signals to a microcontroller unit (MCU) placed for the firmware implementation of the EPC Gen. 2 Class 1 protocol, which is based on the open-source version provided by the WISP project [47][48]. With respect to a standard tag, the MCU

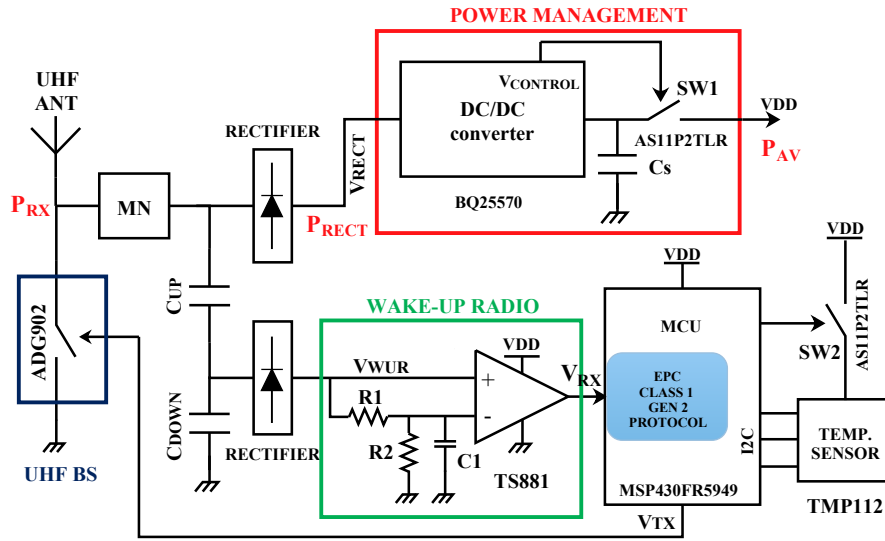


Figure 5.1: UHF-RFID tag hardware scheme [54].

attaches the temperature data information to the EPC frame during the standard communication exchange. The backscattering signal issued by the MCU, and sent back to the reader through the UHF link, is modulated by the ADG902 switch (Analog Devices) which has good RF performance up to 1 GHz and low quiescent current consumption to operate. In order to perform the UHF backscattering procedure, the switch changes the antenna impedance by switching between ground short circuit and matched states offered by the matching network. Since the power consumption of the overall system plays an important role for the performance evaluation, an additional switch (SW2) is used to turn off the external sensor during inactivity periods, in order to reduce unnecessary quiescent current consumption.

### 5.3 Digital base-band Tag operation

Once the node is energized and circuits are powered, it goes in an idle state waiting for the wake-up signal coming up by the reader. The received modulated forward link signal is cleaned with a data slicer, Fig. 5.1, based on an ultra-low power comparator (TS881 by STMicroelectronics) which brings the input weak signal to correct digital voltages used by the microcontroller. It worth to mention that  $R_1$ ,  $R_2$  and  $C_1$  have to be properly chosen in order to filter out the unwanted wake-up requests. In particular, the MPPT practiced by the DC/DC converter influences the correct detection of the wake-up signal and commutates the comparator output. The filter is placed with a resistive divider of  $R_1 = R_2 = 1 \text{ M}\Omega$ , so that the

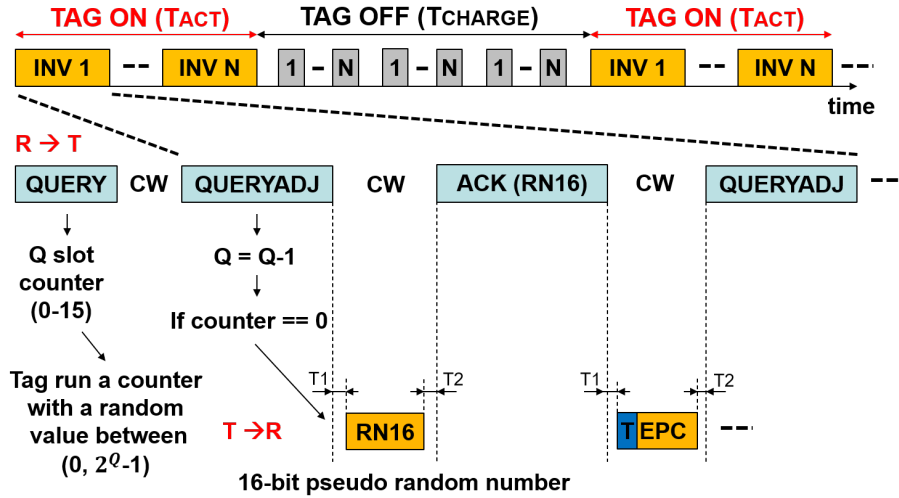


Figure 5.2: RFID Tag protocol operation.

comparator negative input is the half of the positive one in order to deal fast signal changes. The capacitance value of  $C_1 = 10$  nF is chosen accordingly to the forward link communication data-rate of 128 Kbps. Hence, the data frame is ready to be processed by the microcontroller which is in charge of implementing the EPC Class 1 Gen 2 standard protocol and adapted to work with European standards.

The interrogator manages the Tag population using the *Select* command to define a specific group of nodes, then it starts an inventory-round (Fig. 5.2 and Fig. 5.3) with a *Query* command which contains the slot counter number  $Q$  (defined between 0 to 15). This number is used to run a counter with a random value between 0 to  $2^Q - 1$ . Through *QueryAdjust* commands, the  $Q$  number can be brought to zero to speed-up the inventory-round enabling the node to send back the 16-bit random number RN16. The RN16 allows to have a random access to the channel and it is followed by an acknowledge command, in which the same value is placed.

Finally, to end the inventory-round, the tag replies with the Electronic Product Code (EPC) used as Tag identification. During the forward link communication, the MCU sets its internal fast clock of 16 MHz to detect the pin changes on the receive channel, in a real-time configuration, and classifies the commands in order to define the next operation. If a reply is expected, the reverse link communication is managed with a 8 MHz clock frequency, for lower power consumption, since it is not time critical as the previous phase. The WISP project, initially, was intended for United States readers, where the constrains in terms of transmitted power and link frequencies are different from European versions (4W EIRP in 902-928 MHz frequency band). For this reason, significant changes have been done to adjust the firmware for operation with European readers. Tab. 5.1 and Fig. 5.4, summarizes

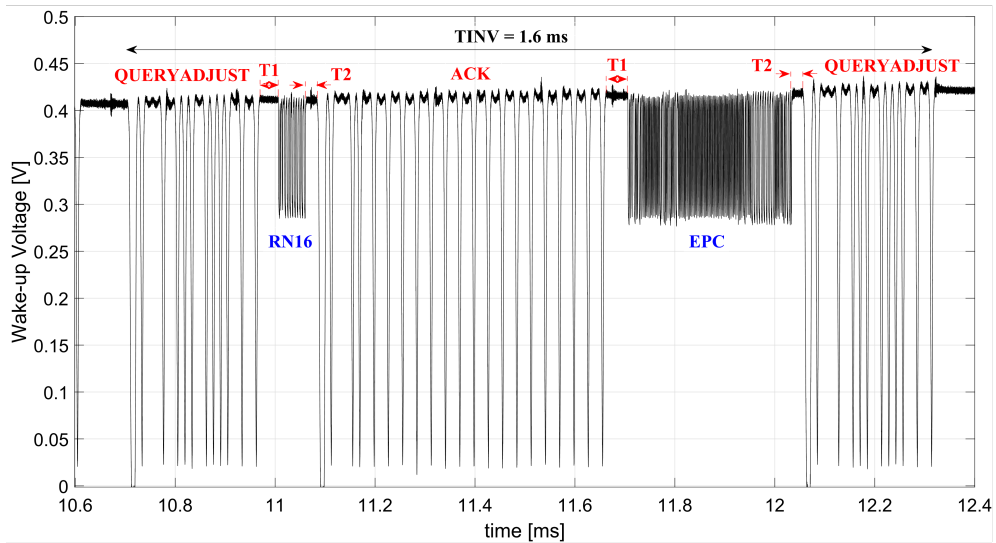


Figure 5.3: Tag Inventory-round with  $Q = 0$ , and Tag population set to 1, since there is only one node to identify [54].

all set of parameters used to interact with a European reader. In particular, the timing  $T_1$  and  $T_2$ , shown in Fig. 5.3 and Tab. 5.1, are protocol defined and have been properly set, on the Tag side, to make it operate correctly. In addition, the EPC, by design choice, contains two bytes with the temperature sensor data information from TI TMP112. When the tag is powered-up the sensor requires 35 ms, in the worst condition, to have an updated version of the temperature data. It is subsequently sent, through the I2C interface, to the MCU and stored (interrupt managed in few  $\mu s$ ), in its non-volatile memory, within the RFID protocol phases. Since the inventory-round time (1.6 ms) is significantly lower compared to the temperature conversion time, the Electronic Product Codes contain a temperature value previously stored (older of few tens of ms). Hence, the sensor conversion time defines the minimum Tag Activation time ( $T_{ACT}$ ).

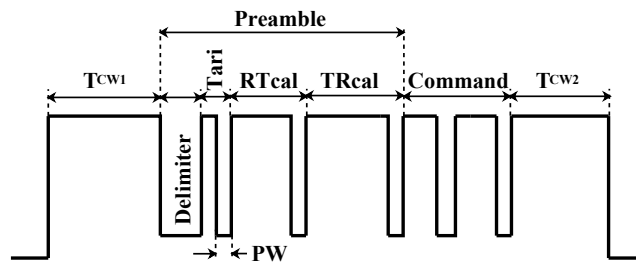


Figure 5.4: Reader to Tag communication parameters [54].

Name	Value	Explanation
$T_{CW1}$	3.8 ms	Continuous wave
<b>Delimiter</b>	12.5 $\mu s$	Start of frame
<b>Tari</b>	16.67 $\mu s$	Modulation depth
<b>PW</b>	8.335 $\mu s$	"0" bit duration
$RT_{CAL}$	41.7 $\mu s$ - 50 $\mu s$	Pulsewidth
$TR_{CAL}$	45.8 $\mu s$ - 150 $\mu s$	"0" + "1" duration
$T_{CW2}$	undefined	Tag backscatter phase
<b>BLF</b>	436 Kbps	Backscattering link frequency
<b>DR</b>	128 Kbps	Forward link frequency
<b>Rev. mod.</b>	FM0	Reverse signal coding
$T_1$ $RT_{CAL}$ : 41.6 $\mu s$ $RT_{CAL}$ : 50 $\mu s$	30.5 $\mu s$ - 52.8 $\mu s$ 37 $\mu s$ - 63 $\mu s$	Time from interrogator transmission to Tag
$T_2$	7.5 $\mu s$ - 50 $\mu s$	Time from Tag replay to Interrogator transmission

Table 5.1: Main UHF-RFID configuration parameters [54].

## 5.4 Power management and Energy budget

In Fig. 5.5, the load is activated when the storage capacitor  $C_s$  reaches the high threshold voltage  $VH = 2.2 V$  and subsequently switched off once it falls down to the low threshold voltage  $VL = 1.85 V$  (chosen by considering the MCU minimum voltage supply of 1.80 V). The stored energy from a fully discharge state is given by  $E_{ON} = 1/2C_sVH^2$ , collected in  $T_{ON} = E_{ON}/P_{AV}$ . In this particular case, the available power to the load is slightly different compared to the presented solution in Section 4.2.6, and is given by:

$$P_{AV} = D_{CW}\eta\alpha P_{RX} \quad (5.1)$$

Starting from the UHF antenna received power ( $P_{RX}$ ),  $\eta$  and  $\alpha$  are the efficiencies of the rectifier stage and power management unit respectively. In a real scenario, both efficiencies depend on the received power with a non-linear behaviour. To simplify the model, the values taken into account are referred, as worst case, to the lower  $P_{RX}$  necessary to ensure the Tag start-up ( $\eta = 28 \%$ ,  $\alpha = 65 \%$ ). Moreover, the value of continuous wave duty-cycle ( $D_{CW} = 66 \%$ ) has been used to consider the periodic RFID standard-defined power holes, performed by the interrogator during the communication exchange with the tag. Hence, the storage capacitor

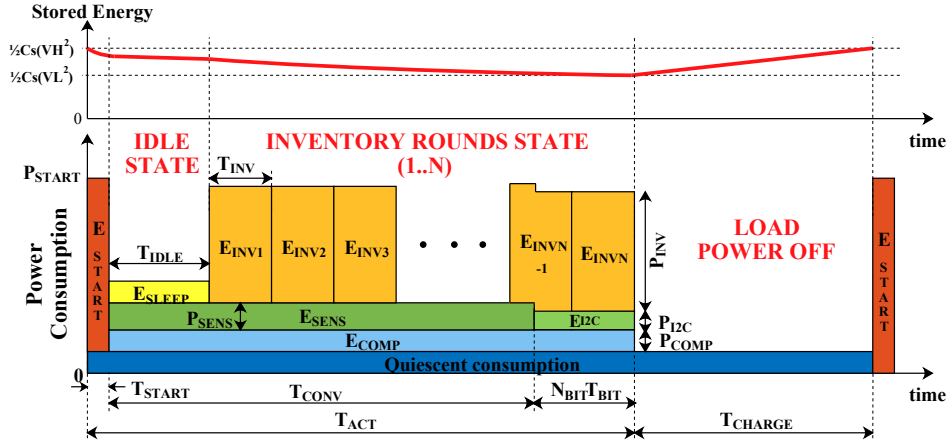


Figure 5.5: Tag energy consumption profile. It has been supposed that the reader performs a Single Target Inventory in Session 0 [54].

$C_s$  has to be defined according to the Tag active time ( $T_{ACT}$ ) required in order to accomplish the inventory-rounds and store the temperature sensor information. For this reason, from the energy budget point of view, the  $T_{ACT}$  must be:

$$T_{ACT} \geq T_{START} + T_{CONV} + N_{BIT}T_{BIT} = 35.57 \text{ ms} \quad (5.2)$$

in order to store a new temperature value.

All parameters in terms of devices current consumption and timings are illustrated in Tab. 5.2. When the  $T_{ACT}$  is ended, the tag load is switched off while only the power management unit is still working to harvest the energy. Therefore, the minimum available power required to charge the storage capacitor is  $P_{AVmin} > P_{DCDC} + P_{SW} = 1.5 \mu \text{ W}$  which represents the quiescent power consumption. To simplify the following considerations, it has been assumed the pejorative approximation for the storage capacitor voltage ( $V_S = V_H$ ). The total amount of energy used for tag operation in  $T_{ACT}$  is defined in three different states as:

$$\Delta E = E_{START} + E_{IDLE} + E_{INV1,N} \quad (5.3)$$

where:

- $E_{START}$ : load power-up state energy;
- $E_{IDLE}$ : idle state energy;
- $E_{INV1,N}$ : inventory-rounds state energy;
- $N = (T_{ACT} - T_{IDLE} - T_{START}) / T_{INV}$  number of inventory-rounds per  $T_{ACT}$

Once the MCU is activated ( $E_{START} = 391$  nJ), it goes into low power mode 4 (LPM4) and the Tag energy consumed ( $E_{IDLE}$ ) is calculated as follow:

$$E_{IDLE} = V_H T_{IDLE} [I_{SLEEP} + I_{CONV} + I_{COMP}] = 893 \text{ nJ} \quad (5.4)$$

$T_{IDLE}$  is not well predictable, because it depends on where the load power-up instant falls, during the reader interrogation. The time between two inventory-rounds cycle (10ms), defined by the protocol, determines the worst case for  $T_{IDLE}$ . Subsequently, the reader starts the inventory-rounds and the node goes into the most energy-intensive state ( $E_{INV1,N}$ ), where it consumes:

$$E_{INV1,N} = V_H [I_{COMP} T_{ACT} + I_{CONV} (T_{CONV} - T_{IDLE}) + I_{I2C} N_{BIT} T_{BIT} + N I_{INV} T_{INV}] = 68.4 \text{ } \mu\text{J} \quad (5.5)$$

The energy consumption of SW2 during  $T_{INV}$  has been neglected since it is hundreds times lower compared to other contributions. Hence, the overall Energy consumed by the tag in one activation period is  $\Delta E = 69.7 \text{ } \mu\text{J}$ . The impact of the idle state and start-up are negligible if compared to the inventory-rounds state where the tag is read N times consecutively. The energy information has been collected in order to define the appropriate storage capacitor for the system:

$$C_S = \frac{2\Delta E}{V_H^2 - V_L^2} = 98.3 \text{ } \mu\text{F} \quad (5.6)$$

A capacitor of  $100 \text{ } \mu\text{F}$  has been chosen according to the consideration over reported. Now, it is possible to calculate the tag charge time as a function of the available power:

$$T_{CHARGE} = \frac{\Delta E}{P_{AV} - P_{DCDC} - P_{SW}} \quad (5.7)$$

which is used to evaluate the performance of the energy harvesting blocks by introducing the duty-cycle parameter:

$$D_{ACT} = \frac{T_{ACT}}{T_{ACT} - T_{CHARGE}} \quad (5.8)$$

Increasing the storage capacitor  $C_S$ , enlarge the active time period and consequently the inventory-rounds per cycle (N). However, the charge time rises in the same way without affecting the duty-cycle and the number of tags read per time unit. Therefore, the idea is to set the minimum capacitance value to accomplish the required tasks during the active period, in order to have readings well distributed in time. The number of reads per second can be computed as follow:

$$\text{Number of Reads/sec} = \frac{N}{T_{ACT} + T_{CHARGE}} \quad (5.9)$$

All parameters used to evaluate the RF energy-harvesting performance of the tag [182], in terms of duty-cycle operation and read-range are discussed in the next Section, with the comparison between theoretical and experimental results.

Param.	Value	Explanation
$T_{ACT}$	35.57 ms	Tag Activation time
$T_{INV}$	1.6 ms	Inventory-Round time
$I_{INV}$	1.2 mA	MCU average current consumpt.
$T_{IDLE}$	10 ms	Max Tag idle time
$I_{COMP}$	210 nA	TS881 current consumption
$I_{SLEEP}$	400 nA	MCU current consumption in LPM4
$P_{DCDC}$	1.3 $\mu$ A	DC/DC power consumption
$P_{SW}$	200 nW	SW1 power consumption
$T_{CONV}$	35 ms	TMP112 cinversion time
$I_{CONV}$	40 $\mu$ A	TMP112 temp. conversion current
$I_{I2C}$	15 $\mu$ A	TMP112 I2C current consumption
$T_{BIT}$	2.5 $\mu$ s	I2C bit time (@ 400 Kbps)
$N_{BIT}$	28	1 byte address + 2 bytes data

Table 5.2: Main UHF-RFID energy-budget parameters [54].

## 5.5 Tag performance

The test bench for measurements used in indoor environment is shown in Fig. 5.6. It is based on the reader Speedway R420 by Impinj connected to the antenna Far Field (8.5 dBi of gain) of the same company, jointly with the Impinj Item Test software used for Tag Inventory and Access. To be ETSI compliant, the maximum transmitted power of 2 W ERP has been used. The reader is configured to perform Inventory-rounds with Single Tag Inventory mode in Session 0, which represents the maximum reading throughput.

As measurement approach [182], in order to evaluate the first activation range, the platform has been placed at 10 m of distance from the reader and moved closer it until the node has been powered-up ( $T_{ON} = 23$  s at 7 m). Then, starting from the same position, the distance has been increased with incremental step of 1 m up to the maximum distance (9.70 m) where the tag stopped operating due to insufficient incoming power. In the battery-less configuration, the tag has a

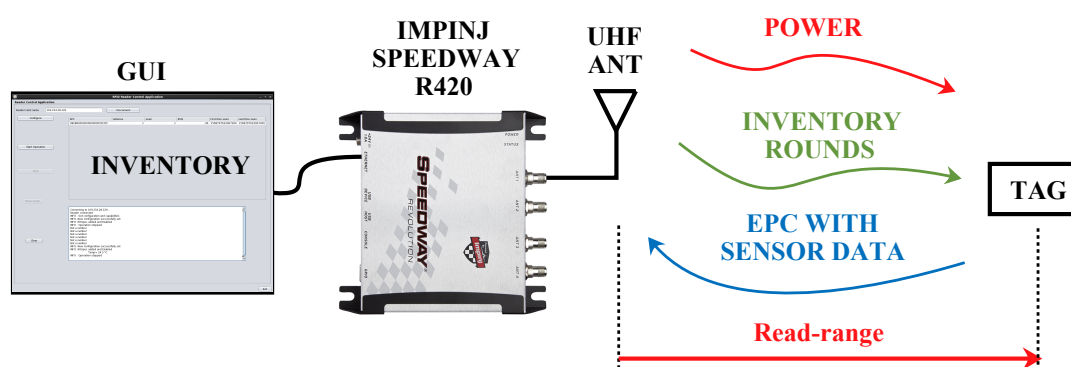


Figure 5.6: Test bench for the UHF-RFID tag performance measurements [54].

sensitivity of  $-16$  dBm with a read-range of  $9.70$  m, which is limited by the forward power transfer. If an on-board battery is present (battery-assisted configuration) the sensitivity, considered only for the data link communication, falls to  $-17.8$  dBm with a maximum read-range of  $15$  m. In this case, the limitation is given by the reverse link, where few mV of received voltage on the wake-up radio, are not sufficient to demodulate the data stream. Moreover, on the reader side, the power incoming from the backscattered signal is weak and close to the interrogator sensitivity of  $-70$  dBm which represents another limit on the read-range.

### 5.5.1 Tag duty-cycle and charge time

A set of inventory-rounds have been run, for all tag positions starting from  $1$  m up to  $9.70$  m, to collect the timestamps of all acquisitions in order to evaluate the charge time and subsequently the duty-cycle. All measurements are reported in Fig. 5.7 and compared with analytical results of Eq. 5.7 and Eq. 5.8. The measured results are consistent, compared with the analytical ones, except slight differences due to the multi-path effects on the transmitted signal which is reflected by the obstacles. On the tag side, the multi-path contributions can be added in phase, by increasing the received power (this is the case between  $7$  m to  $9.70$  m), or out of phase by lowering the received power with the consequence of slower charge time (starting from  $1$  m up to  $7$  m). In the worst condition, at  $9.7$  meters, once the node is powered, the re-charge phase is performed in less than  $20$  s.

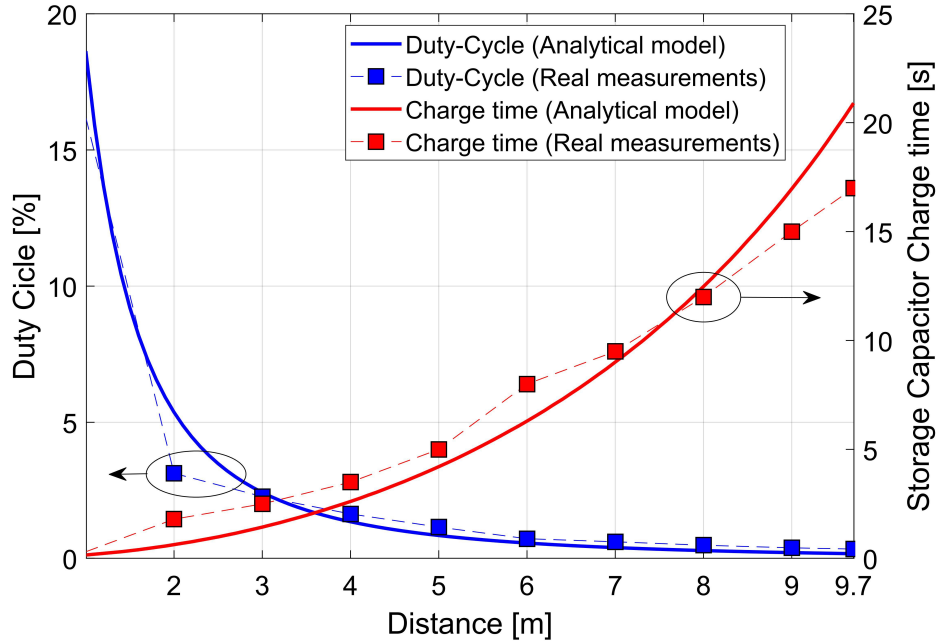


Figure 5.7: Comparison between modelled and measured Tag duty-cycle and charge time [54].

### 5.5.2 Read-rate and environmental sensing

In all RFID applications, during the requirements definition, one of the most popular parameters is the read-rate, which is the number of tags read per time unit. The presented battery-less sensor Tag has a read-rate of 2908 reads per minute at 1 m decreasing down to 48 reads per minute at 9.70 m, Fig. 5.8.

The read-rate can rise up to 725 tags per second if the node is equipped with an on-board battery, without limitation given by the wireless power transfer. The EPC contains the sampled temperature data, which is updated every  $T_{ACT}$  period where one temperature conversion is performed and stored. So, all inventory-rounds (N) executed during  $T_{ACT}$  contains the previous temperature recorded in  $T_{ACT-1}$  in order to preserve the energy consumption for faster re-activation.

In Fig. 5.9, 1 h of recorded temperature is shown, where several external disturbances have been applied to test the sensor. After 10 minutes a window has been open and subsequently closed at minute 30, with a temperature variation of about 1.5 °C. Then, a hot air machine has brought the room temperature to 26 °C in few minutes.

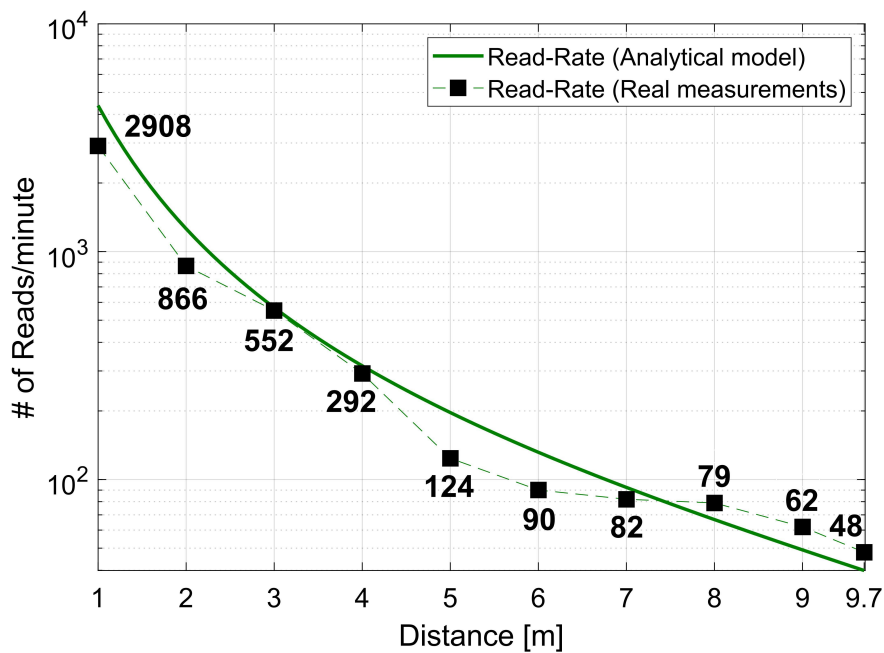


Figure 5.8: Comparison between measured and modelled battery-less tag read-rate as a function of the distance from the reader [54].

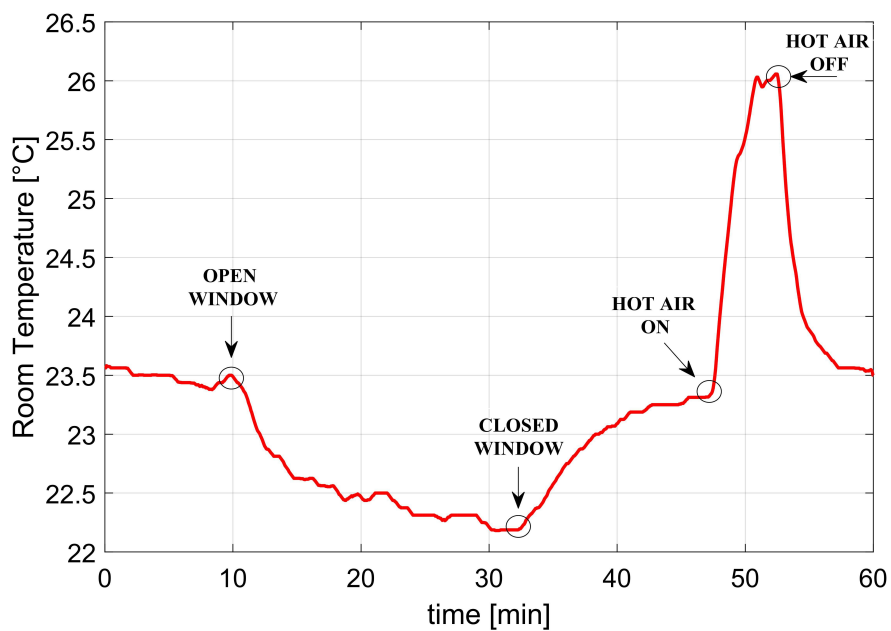


Figure 5.9: Room temperature recording with UHF-RFID tag [54].

## 5.6 UWB-RFID Tag integration

Stand-alone RFID systems without localization engine, Fig. 5.10(a), can not distinguish the presence of objects in a defined area, causing unwanted reads. Hence, RFID can implement the RSSI-based localization (Fig. 5.10(b)), but it has low accuracy in terms of positioning. As discussed in Section 1.4, the introduction of UWB sub-circuits is strictly related to localization purposes. The idea is to build a hybrid tag solution called UWB-RFID tag which is capable of *high ranging accuracy* and robustness against multipath propagation, due to the fine temporal resolution and spectral properties of UWB signals, Fig. 5.10(c). In Chapter 4 UHF-UWB tags have been developed and designed following the transmitting principle based on generation of UWB pulses on-board. On the other hand, in this Section, It has been used the backscattering technology for UWB localization in order to compare both solutions and provides application scenarios in which they can be adopted. In particular, this kind of systems, has a relevant impact on limited-range applications such as item counting, baggage handling etc.

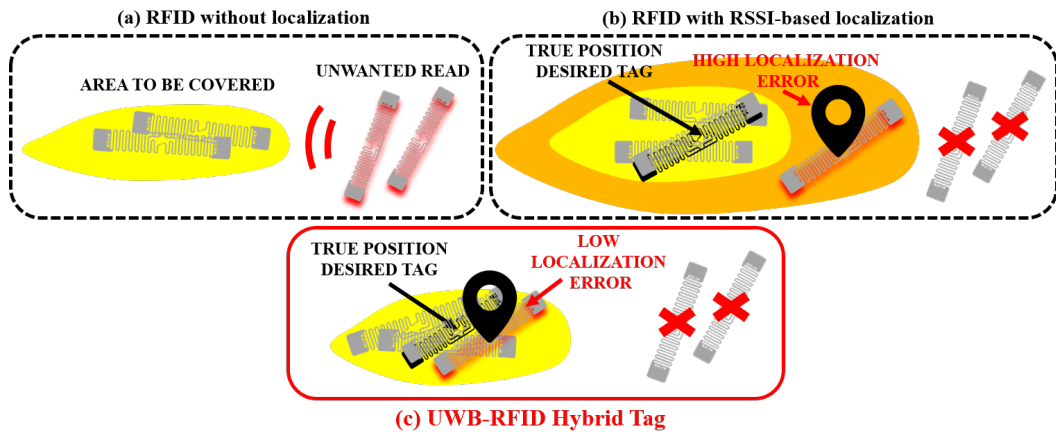


Figure 5.10: Typical scenarios of RFID tags confined in a certain area (a) without localization (b) with RSSI-based localization and (c) with UWB-based localization.

### 5.6.1 UWB-RFID backscattering tag design

The choice of the components and of their configuration, can have a significant impact on the overall energy budget for every activation and on the figures of merit related to UWB localization. Fig. 5.11 reports three possible configurations for backscattering tag circuits, based on different sets of off-the-shelf components. In configuration (a) of Fig. 5.11, the lowest energy per operation is pursued. A very

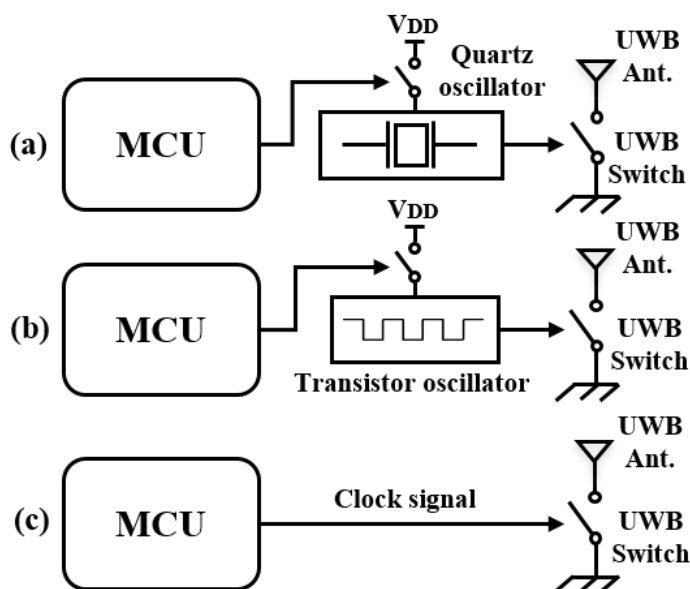


Figure 5.11: Micro-power architectures for backscattering subsections of the tag based on (a) quartz oscillator (b) transistor oscillator and (c) MCU clock generation.

precise quartz oscillator is powered-up through a MCU and used to control UWB backscattering: the OV-0100-C7 from Micro Crystal offers excellent frequency stability of 20 ppm and a worst-case current consumption of 750 nA. The main drawback consists in an initial settling time, in the order of several hundred ms, which limits the activation rate of the tag in case it is disabled at the end of the backscattering phase. Keeping the oscillator enabled would increase tag background consumption of few  $\mu\text{W}$ , which could impact negatively in operation at several meters from the UHF power source, when the harvested power is comparable. On the other side, the excellent frequency stability allows to drastically reduce the computational load at the reader side, where coherent signal acquisition (which is a challenging task in case of poor clock stability) is necessary to detect the weak signal of a tag, thus relaxing hardware specifications.

In configuration (b) of Fig. 5.11, faster activation times and better performances of components are pursued. A LT6906 transistor oscillator with a very fast start-up time ( $< 1$  ms) is adopted for backscattering, but at the cost of lower frequency accuracy ( $< 0.65\%$ ), a  $0.03\%$  timing jitter on clock edges, and a higher current consumption of  $12\ \mu\text{A}$  at 100 kHz. The lower accuracy with respect to quartz oscillators increases computational requirements in readers, since multiple parallel de-spreaders, tuned on different clocks, must be implemented in order to maximize the energy output in case of larger timing errors. As an overall result, the energy consumption of a single activation is increased approximately of one order of mag-

nitude with respect to configuration (a). This reduces, accordingly, the maximum activation rate of tags.

In configuration (c) of Fig. 5.11, the lowest component count is pursued. The backscattering switch is directly driven by the microcontroller. During this phase, the on-chip DCO clock is buffered on an output pin, while the CPU is disabled. Worst-case frequency accuracy is in the order of 3 %, and temperature drift is around 0.01 %/°C.

Although the tag hardware is simplified, extraction of frequency and synchronization at reader side become more complex. In fact, in this case, parallel de-spreading is mandatory, since a mismatch between the frequency driving the backscatter modulator, at tag side, and that accounted for the de-spreading, at reader side, could severely degrade the SNR of the demodulated signal, making time-delay estimation and localization unreliable. To minimize these effects, the receiver architecture must be replicated, tuning each receiver branch on a different tag clock and selecting the output presenting the maximum output energy. Obviously, if latency is not stringent, the processing of the received signal with different timing hypothesis can be conducted in sequence for preserving the overall complexity.

Finally, the backscattering UWB switch choice plays an important role in the system performance. A low-power consumption solution is given by HMC550AE (Analog Devices) UWB backscattering switch. It has a very low on-state current of 200 nA with an insertion-loss lower than -1 dB up to 6 GHz. Moreover, when better performances are required, the SKY13350 UWB switch can be considered, which results in both an increased current consumption (5  $\mu$ A) but also in an improved SNR for the backscattered UWB signal, thanks to the reduced loss on the RF path (insertion loss of -0.6 dB at 6 GHz). Enhanced SNR is beneficial for localization. In fact, the time-delay estimation accuracy, which is the foundation of time-based localization, is determined by the signal bandwidth and the SNR experienced by the received signal.

Hence, according to the considerations previously done, the solution (b) represents the best compromise between power consumption and performance, combined with the HMC550AE switch. Fig. 5.12 shows the hardware architecture discussed in Section 5.2, updated with the UWB backscattering circuitry, which low-losses PCB is reported in Fig. 5.13. It is worth to mention that, the UWB antenna (Molex 146184) is externally connected, for a compact-sized PCB design.

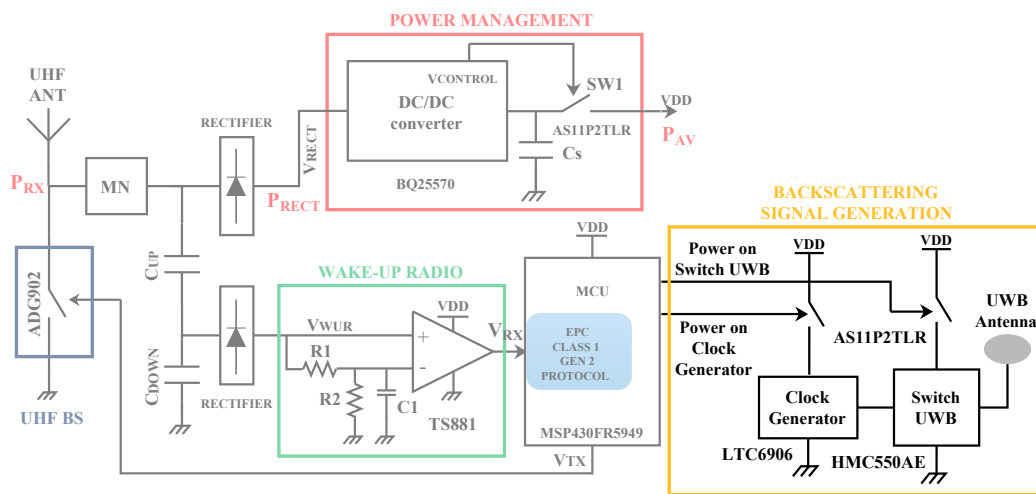


Figure 5.12: UWB-RFID backscattering tag scheme.

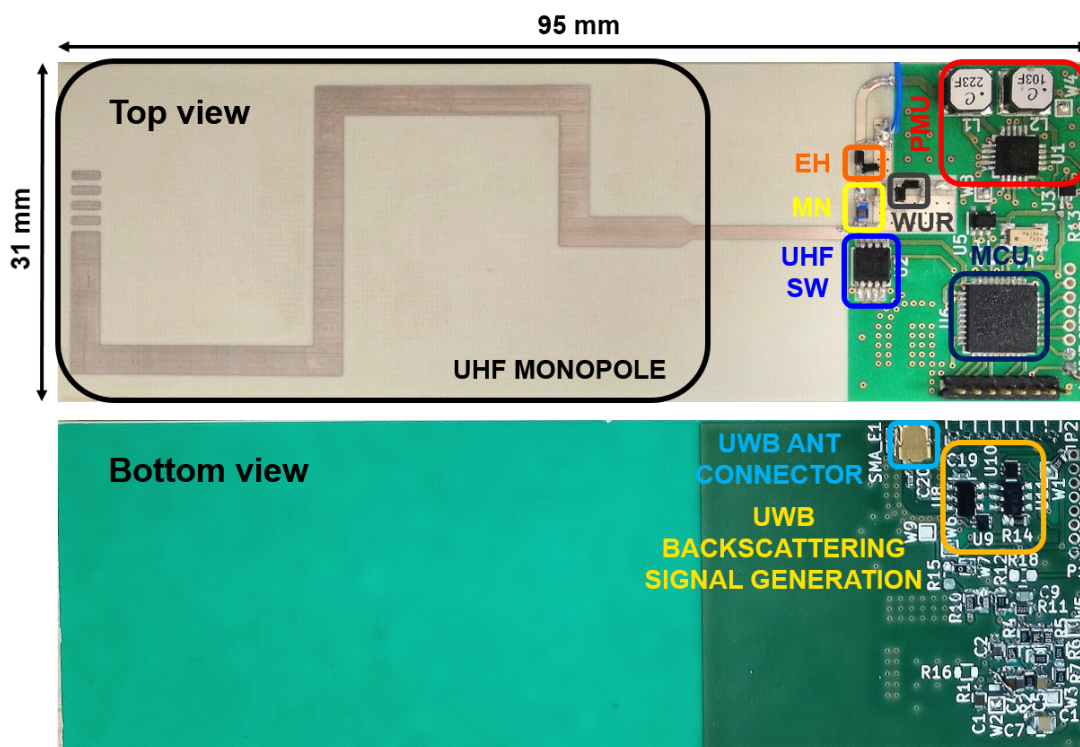


Figure 5.13: UWB-RFID backscattering tag PCB design.



# Chapter 6

## Localization Results

### 6.1 UHF-UWB transmitting Tag Application

Fig. 6.1 illustrates the general system architecture [183][184] that is composed of the following sub-systems:

- *Central Unit (CU)*: It is a software module running on a general-purpose computer. The Central Unit is in charge of: (i) scheduling the addressing of each tag in the area by sending proper commands to the Reference Nodes and the Power Transfer Units; (ii) collecting the time-of-arrival (TOA) measurements from the Reference Nodes; (iii) estimating the position of each tag (localization engine) with signal processing algorithm developed by the Telecommunications group; (iv) managing the entire network (configuration, calibration, diagnostic, etc); (v) providing an application program interface (API) to the user graphical interface. The position estimation and tracking algorithm makes use of a particle filter implementation [81].
- *Graphical User Interface (GUI)*: It is a software module that provides the user with a graphical representation of tag positions through continuous interrogations of the Central Unit. Moreover, It is used to set-up the scenario such as number and position of reference nodes, tags address, and several localization parameters.
- *Power Transfer Unit (“energy shower”)*: It is an RF system designed to transmit RF energy, at the maximum allowed power of 2 W ERP in the UHF-868 MHz band, to all tags in the area. Furthermore, according to the scheduling set by the Central Unit, it sends periodically a specific ON-OFF keying (OOK) modulated signal to address the tags in turn.

- **Control Interface:** The Control Interface is in charge of translating the commands received, from the Control Unit through the network into electrical signals, driving the other blocks of the LOST system. In particular it has to (i) generate the trigger for the fine synchronization of the reference nodes, (ii) enable the UHF power transfer for energy harvesting and addressing phases.
- **Tag:** According to the requirements, the tag is battery-less and harvests the necessary energy from the RF signal emitted by the Power Transfer Units. Once powered and addressed, the tag provides a short-time feedback to the Reference Nodes. In particular, the tag generates a quasi-periodic sequence of UWB pulses (in the transmitting node configuration).
- **Reference nodes:** The UWB sequence generated by the tag is acquired by at least 3 Reference Nodes that forward the data to the Central Unit where the TDOA is estimated through proper algorithms.

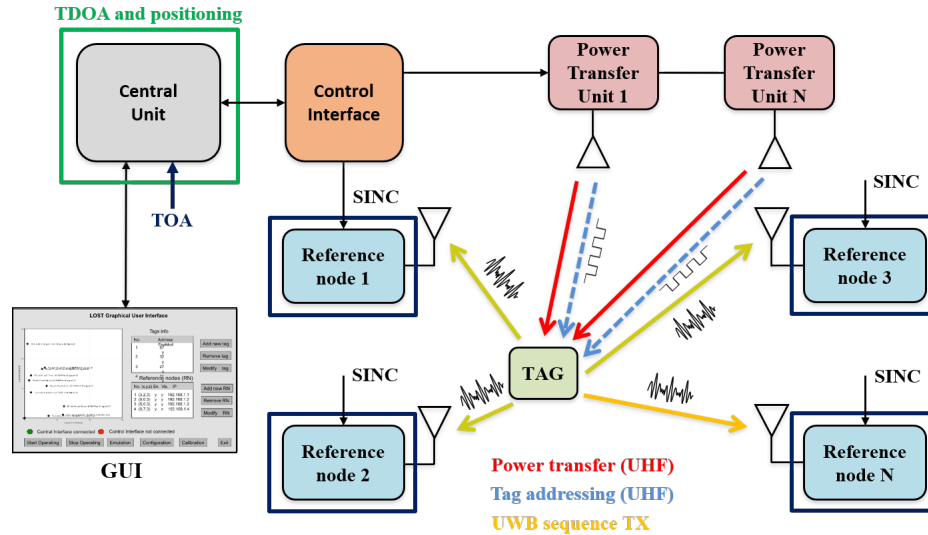


Figure 6.1: ESA-LOST Tags localization scenario.

The area to be monitored is equipped with  $N_{rx}$  receiving reference nodes. Their number is chosen to guarantee a sufficient service coverage in the intended area, in terms of tag detectability and localization accuracy, according to project requirements, from a minimum number of  $N_{rx} = 3$  nodes (which can guarantee a 2D positioning) to a maximum number related to the complexity of the environment (obstacles, shadowed areas, etc.). The LOST system is controlled by the Central Unit that periodically initiates an interrogation cycle in which a specific tag is powered and addressed via the UHF link. Specifically, at the beginning of the

interrogation cycle, the intended tag is addressed (woken up) by sending its ID through the UHF link, modulating the UHF carrier using an OOK scheme. In between each interrogation cycle, a UHF CW (Continuous Wave) signal is emitted by the Power Transfer Units (energy showers) to let all tags in the area collect a sufficient energy to operate. Once woken up, the tag emits a sequence of UWB pulses and returns into a sleep mode, waiting for the next interrogation cycle. During the transmission of the UWB pulses sequence, all Reference Nodes are triggered by the control interface to perform the analog-to-digital conversion and buffering in order to evaluate the time-of-arrival (TOA) of the incoming signals. The received samples are then forwarded to the Central Unit that is in charge of detecting the tag and compute the TDOA among the signal replicas received by different Reference Nodes. The localization engine, running in the Central Unit, combines all TDOA measurements to estimate the position of the tag. The tags present in the area are addressed sequentially through different interrogation cycles. In between one interrogation cycle and the subsequent one, each Reference Node performs the necessary processing tasks of the samples recorded in its buffer. This time interval, where the UHF transmitter provides a continuous-wave, is longer than the interrogation signal, to allow sufficient energy to be transferred to the tags. Therefore the processing speed can be relaxed with respect to a pure real-time implementation.

### 6.1.1 Signal processing

One challenging aspect is how to perform TDOA measurements with high accuracy. In fact, conventional TDOA estimation requires reference nodes to be time synchronized with uncertainty in the order of 33 ps (corresponding to 1 cm distance estimation error as per requirements) via precise calibration and wired interconnections, as in Fig. 6.1. To avoid this issue, such tight synchronization requirement has been relaxed to several microseconds through the introduction of a dedicated *double cross-correlation* algorithm, thus allowing wireless synchronization and easier calibration. The algorithm requires the introduction of an *UWB Sync transmitter* (equipped with the same pulse generator used for the tag [78]) which is in charge to provide a reference synchronization signal. Specifically, from a localization point of view, the receivers (for simplification reasons only two are considered,  $RX_1$  and  $RX_2$  in Fig. 6.2) and the additional transmitting node (i.e.,  $TX_1$ ) are located in known position (i.e., the propagation delays between  $TX_1$  and the two receivers, indicated as  $t_{p11}$  and  $t_{p12}$ , are known a-priori) while only the tag (i.e.,  $TX_2$ ) position is unknown (i.e., the propagation delays indicated as  $t_{p22}$  and  $t_{p21}$  are the unknown). The TDOA to be estimated is given by  $t_{p22} - t_{p21}$ .

With reference to Fig. 6.2,  $t_R$  indicates the unknown offset between  $RX_1$  and  $RX_2$  (in the order of a few microseconds), with  $t_1, t_2$  the unknown transmission

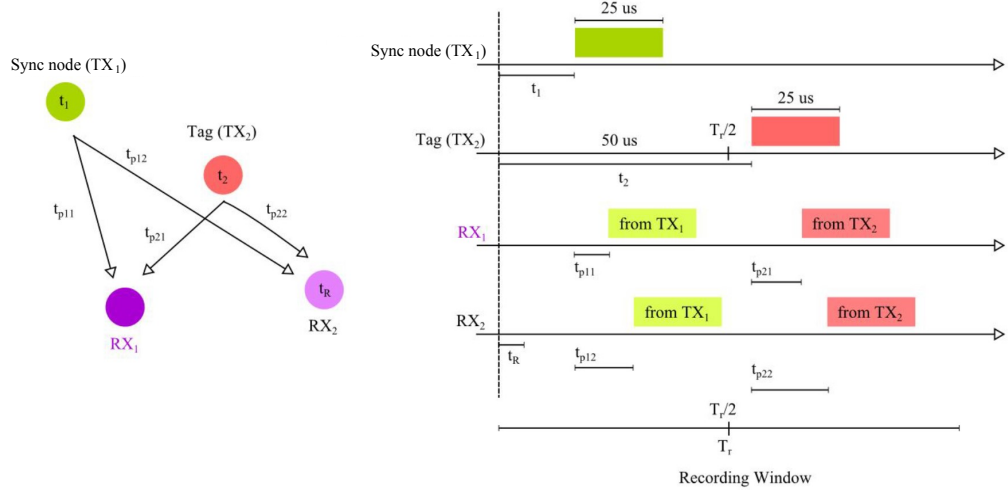


Figure 6.2: The double-correlation synchronization scheme [183][184].

starting instants of  $TX_1$  and  $TX_2$ , and with  $T_r$  the acquisition window of each receiver (in the order of  $100 \mu\text{s}$ ). Moreover, it has been supposed that  $TX_1$  transmits a train of pulses (duration in the order of  $25 \mu\text{s}$ ) within the first half of the receiver acquisition window and the second half, i.e., with  $t_2 > T_r/2$ .

Denote with  $s_1(t)$ ,  $s_2(t)$  the transmitted signals emitted by  $TX_1$  and  $TX_2$ , respectively. Any assumption has been done on their shape apart from their duration that has to be less than  $T_r/2$ . Given this configuration and taking the clock of  $RX_1$  as the reference timeline, the received signals at  $RX_1$  in the first and second half of the recording window, can be expressed respectively as:

$$\begin{aligned} r_{11} &= s_1(t - t_1 - t_{p11}) + n_{11}(t) \\ r_{12} &= s_2(t - t_2 - t_{p21} + T_r/2) + n_{12}(t) \end{aligned} \quad (6.1)$$

where  $t_{p11}$  is the propagation delay from  $TX_1$  to  $RX_1$  (known) and  $t_{p21}$  the propagation delay from  $TX_2$  to  $RX_1$  (unknown). Similarly, the received signals at  $RX_2$  are:

$$\begin{aligned} r_{21}(t) &= s_1(t - t_1 - t_{p12} - t_R) + n_{21}(t) \\ r_{22}(t) &= s_2(t - t_2 - t_{p22} + T_r/2 - t_R) + n_{22}(t) \end{aligned} \quad (6.2)$$

where  $t_{p12}$  is the propagation delay from  $TX_1$  to  $RX_2$  (known) and  $t_{p22}$  the propagation delay from  $TX_2$  to  $RX_2$  (unknown). In both cases  $n_{xy}(t)$  represents the thermal noise. At this point, the cross-correlation functions of the received signals coming from  $TX_1$  and  $TX_2$  is computed within an interrogation window of  $T_w = T_r/2$  seconds, respectively:

$$\begin{aligned}
C_1(t) &= \int_{T_w} r_{11}(\tau)r_{21}(t + \tau)d\tau \\
C_2(t) &= \int_{T_w} r_{12}(\tau)r_{22}(t + \tau)d\tau
\end{aligned} \tag{6.3}$$

It turns out that:

$$\begin{aligned}
C_1(t) &= g_1(t - t_{p12} + t_{p11} - t_R) + w_1(t) \\
C_2(t) &= g_2(t - t_{p22} + t_{p21} - t_R) + w_2(t)
\end{aligned} \tag{6.4}$$

where  $g_1(t)$ ,  $g_2(t)$  are the auto-correlation functions of  $s_1(t)$ ,  $s_2(t)$ , respectively. By neglecting the noise,  $t_1 = t_{p12} - t_{p11} + t_R$ ,  $t_2 = t_{p22} - t_{p21} + t_R$  are the delays at which the peaks of the cross-correlations are located. Taking the difference between these delays it results:

$$\Delta T = t_2 - t_1 = (t_{p22} - t_{p21}) - (t_{p12} - t_{p11}) \tag{6.5}$$

where  $(t_{p12} - t_{p11})$  is known and  $(t_{p22} - t_{p21})$  is the TDOA to estimate. Specifically, the TDOA can be obtained as

$$TDOA = \Delta T + (t_{p12} - t_{p11}) \tag{6.6}$$

Obviously, in the presence of noise, the TDOA estimate will be affected by errors. It is worth to note that, the TDOA in Eq. 6.6 does not depend on the unknown clock offsets  $t_R$ ,  $t_1$ , and  $t_2$ , provided that the received signals fits the two half recording windows of duration  $T_w$  each. Such duration has to be designed as a trade-off between the maximum tolerable synchronization offset, the additional accumulated noise (performance degradation), and the computational complexity. In the implemented system, the maximum tolerable offsets are in the order of several microseconds thus allowing an easy synchronization between receivers, even with standard wireless devices. The overall signal processing scheme is depicted in Fig. 6.3. Large side lobes in the signal cross-correlation function caused by the periodic nature of the generated sequence of UWB pulses, might confuse the peak detection process (ambiguities), therefore a suitable pseudo-noise (PN) modulation of pulses would be required. Fortunately, the signal generated by the UWB chip is characterized by a strong intrinsic jitter so that the double-correlation estimator exhibits approximately the same performance as that using a generator with PN modulated pulses, with the advantage of a lower implementation complexity (no modulation needed). Results indicate that the required accumulated (over 5,000 pulses) signal-to-noise ratio corresponding to a TDOA estimation error of 33 ps (1 cm distance accuracy) is about 37 dB, which differs by only 1 dB from results obtained with a modulated PN sequence.

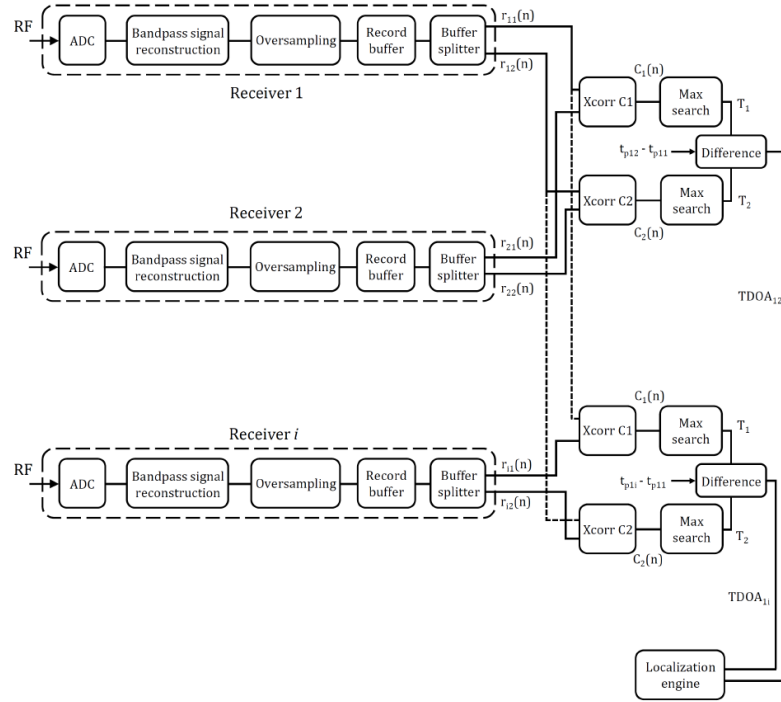


Figure 6.3: Signal processing scheme [183][184].

### 6.1.2 Localization performance

A wide testing campaign to evaluate the localization accuracy has been performed at UCLouvain in Belgium. A room of size  $10 \times 7 \text{ m}^2$ , shown in Fig. 6.4, was used. 2D localization was performed using transmit and receive antennas placed on poles of 2.03 meters high. The receiving antennas were located at the corners of the room and UHF Power Transmit Units were placed at the middle of 3 sides of the room. The exact location of the tags to be localized was recorded using a TOTAL laser station; the accuracy of this measurement is of a few mm. Fig. 6.5 displays the cumulative error (meters, absolute errors in log scale) for different integration times  $T_w$ , ranging from  $0.32 \mu\text{s}$  to  $82 \mu\text{s}$ , by steps of a factor four. Moreover,  $1 \mu\text{s}$  corresponds to an insufficient integration time; integration times larger than  $5 \mu\text{s}$  produce similar results, with a median error very close to 3.5 cm. Good robustness to shadowing has been demonstrated with metallic obstacles having a diameter in the order of 40 cm. Directive antennas (with a gain near 5 dBi) have been quite useful to limit false detection resulting from multiple reflections. Nevertheless further research on multi-path mitigation, using both hardware and software means, is still worthy.

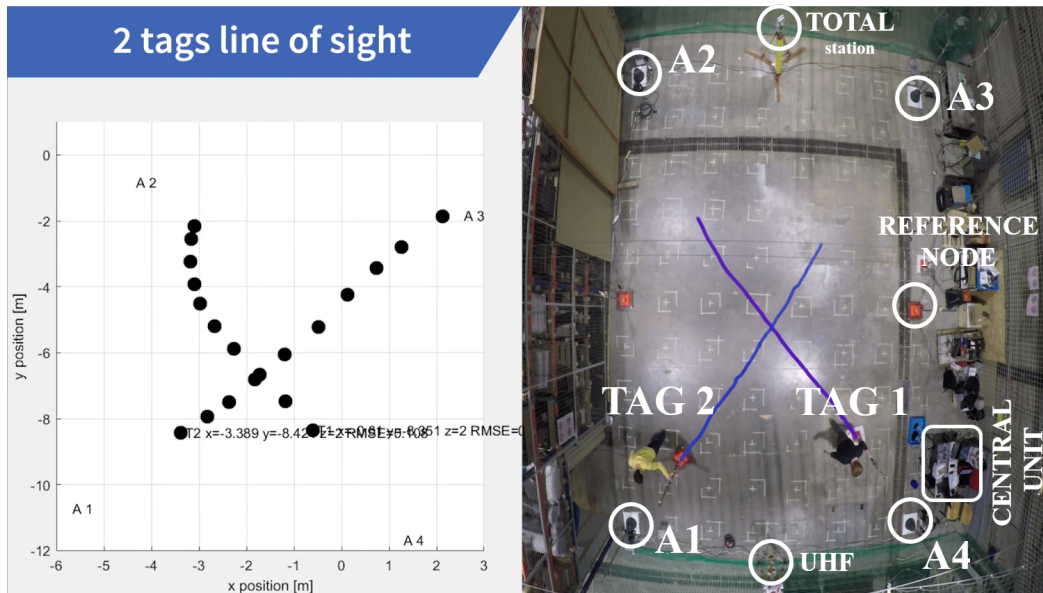


Figure 6.4: Multi-tag quasi-real time localization performed at UCLouvain . In white characters, the main components of the system.

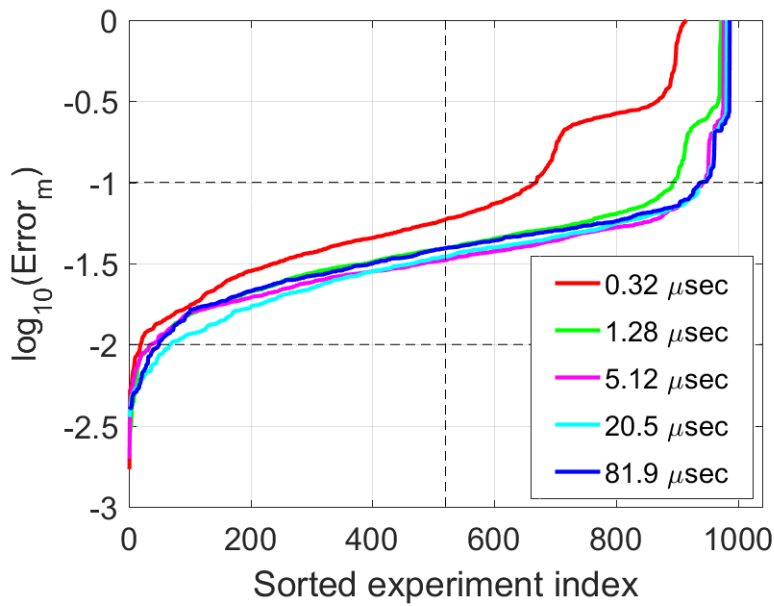


Figure 6.5: Cumulative error versus sorted experiment index for different integration times  $T_w$  [183][184].

A final demonstrator of the LOST project was installed and operated at the ESA/ESTEC Robotics Lab premises (Fig. 6.6). The demo setup consisted of 4 reference nodes deployed at known positions, one UWB reference tag for synchronization, three "energy showers", one tag mounted on top of the Mars Rover prototype, and one tag mounted on a manually handled pole. All nodes were connected to the Control and Central Units, thus resulting in a fully integrated system whose output was visible through the GUI. To assess the performance, we considered 11 tag positions where 100 measurements were taken each time. The global configuration of the system and 11 positions, recorded with a TOTAL station (i.e. with an accuracy of the order of 2 millimeters) are displayed in Fig. 6.7(a). In the following numerical results, we fed the Localization Engine with the measured TDOA data. In the Localization Engine we set the number of location particles to  $30 \times 10^3$ . Due to physical constraints of the demo area, all reference nodes were placed approximately at the same height thus leading to potential large errors in the z-direction. To avoid that such large errors affect the position estimation, we decided to disable the estimation of the tag's height by forcing it to a a-priori value, which was not always exactly corresponding to the actual height because of the non-regular soil. The resulting error was measured to be below 2.6 cm. In a real set up in which reference nodes can be deployed in the area with less constraints, also the height of the tag can be estimated accurately using the same localization engine. Among 100 samples, there is from 0 to 7 outliers, which are generally located very far. Assuming that they can be removed using of dedicated clustering algorithms, the achievable performance is close to the one calculated without outliers. Several approaches can be adopted to detect and cluster the outliers. In the presence of one outlier and more than three TDOA measurements, one can perform consistency checks by grouping measurements in groups of three. A complementary approach is to take advantage of the memory during the tracking by checking time-consistencies as measurements cannot suddenly change.

Fig. 6.7 (b) shows the (empirical) Cumulative Density Function (CDF) of the localization error. For the last tag position (indicated with  $p_{tag,11}$ ), we can see that the localization error is below 2 cm in 50 % of the cases. Now we consider the first position (namely,  $p_{tag,1}$ ) which is the one experiencing the outlier effect. The corresponding CDF is shown in Fig. 6.7 (b) using a continuous black line. Because the number of outliers (three outliers were present in this set-up) is negligible with respect to the total number of measurements, it can be observed that the overall localization error still remains below 10 cm in 95 % of cases. Experiments with  $34 \times 34 \text{ cm}^2$  metallic obstacles between transmitter and two of the receivers were also carried out and exhibited good performance. It was also shown that the localization works properly when the tags are placed inside cardboard boxes, i.e. in conditions where optical line-of-sight would not be ensured.

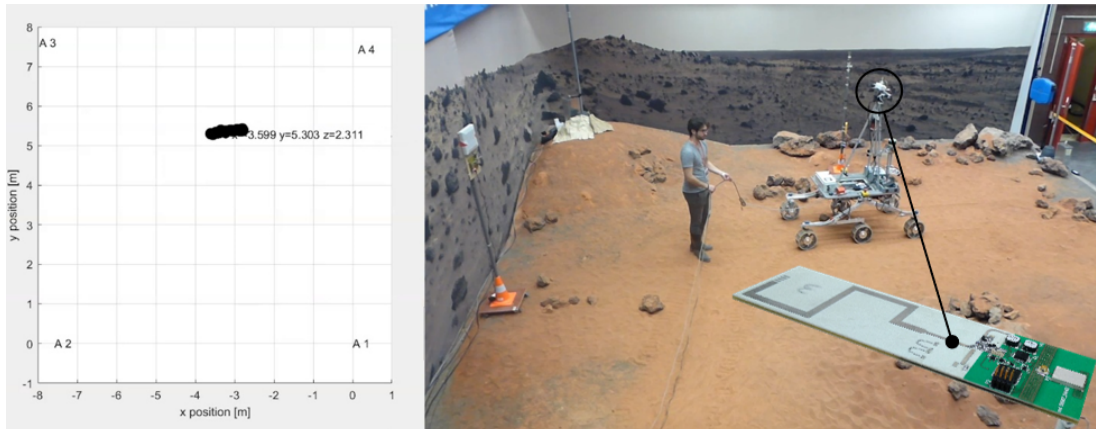


Figure 6.6: (Left) Screenshot of the GUI as taken during the demo at ESA/ESTEC (Right) Robotics Lab with the Mars Rover prototype equipped with the UHF-UWB tag [183][184][185].

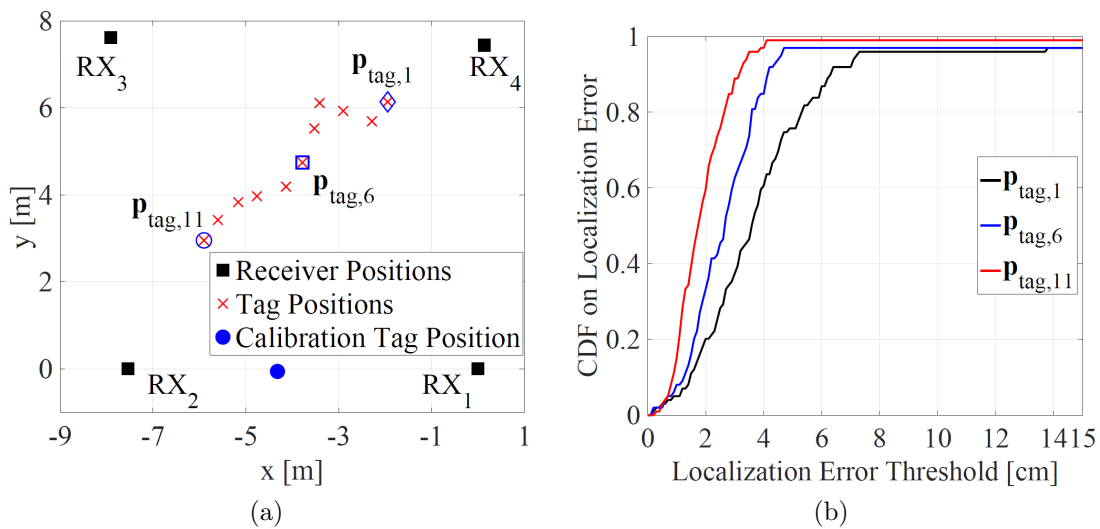


Figure 6.7: (a) Measurement scenario with positions of four receivers (corners), calibration tag (bottom) and 11 test positions of the tag in 2D plane; (b) Empirical CDF of the localization error in three tag test positions [184].

## 6.2 UWB-RFID backscattering Tag Application

In the system overview [186], the backscattering tag to be localized is placed in the middle of the indoor environment under test, Fig. 6.8. Once the node has been energized and identified, through the RFID commercial reader Impinj R420, the latter starts to generate a trigger to the Arbitrary Waveform Generator (Tektronix AWG7122C) in order to release at the same time:

1. the UWB transmission based on a pulses sequence of 200  $\mu\text{s}$ ;
2. the *SYNC* signal for a fine synchronization of the external oscilloscope (LeCroy WavePro 804HD) used as receiver ADC interface (after proper analog filtering and amplification implemented with Mini-Circuits ZX60-83LN12+) and processor for signal processing performed in MATLAB.

The UWB TX signal is emitted, within the UWB mask limitations. Then, the scattered signal from the node, received by RX1 and RX2, is amplified and subsequently processed with the signal processing algorithm embedded in the oscilloscope.

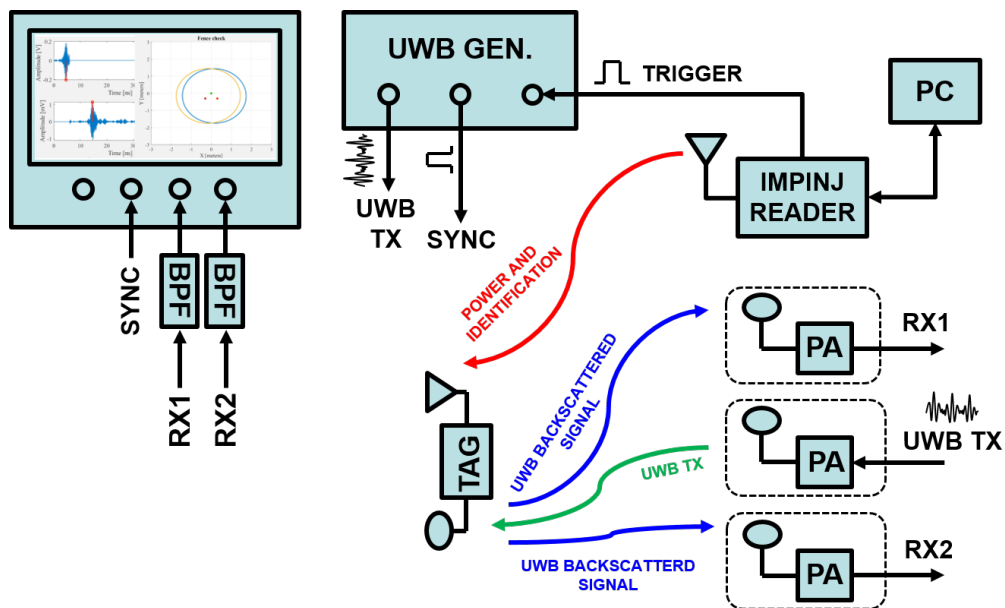


Figure 6.8: Backscattering Tags localization scenario.

The time diagram of the tag operation is represented in Fig. 6.9. During the UHF link communication, the tag has a random access to the channel, through the RN16 packet. When the tag receives back the Acknowledge, it replies with the electronic product code (EPC) which represents its unique identifier. Since the idea

is to merge the UHF-RFID with the UWB technology for positioning, in parallel with the release of the EPC, the MCU starts modulating the impedance of the UWB antenna, with a clock sequence of few milliseconds at 1 MHz. Subsequently, once the reader recognizes the tag identifier, it sends a trigger to the UWB generator (latency of 2 ms), which is in charge of performing a double task, firstly the fine synchronization with the receivers and secondly the transmission of UWB interrogation pulses. In particular, a burst of 4000 UWB pulses is emitted with a pulse repetition period of 50 ns, organized in frames of 10 pulses.

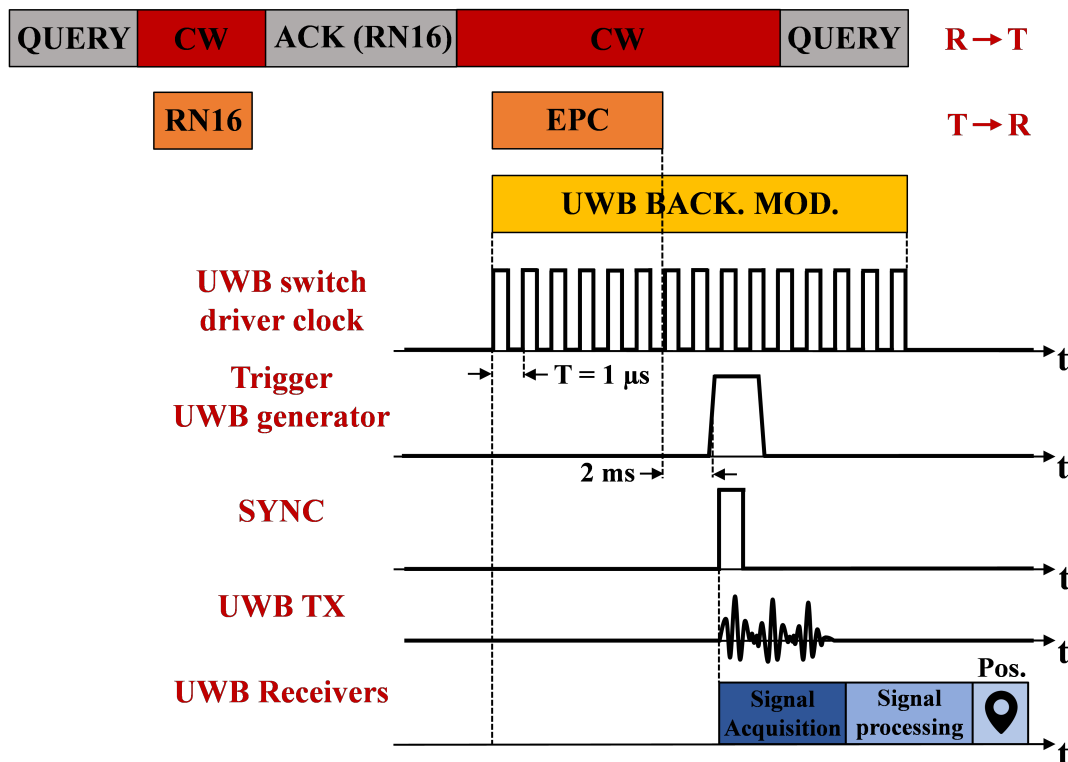


Figure 6.9: Backscattering Tag operation.

### 6.2.1 Basic concepts on signal processing

The receiving chain is reported in Fig. 6.10. In particular, the receivers include an UWB band-pass filter to attenuate the out-of-band contributions before the analog-to-digital conversion at 10 Gsamples/s. The samples obtained include three contributions: the direct UWB signal from the transmitter (coupling), the backscattered signal from the tag and clutter due to the presence of obstacles. The acquired set of samples is divided into frames which are subsequently multiplied

by the tag code (in our case an alternating sequence of +1 and -1) and summed (de-spreading). The de-spreading operation, thanks to the use of a balanced code, allows to significantly mitigate the presence of clutter and to increase the SNR [8]. The de-spreading operation is repeated for different time shifts of the code in order to synchronize with the tag's local oscillator. The processed signal is then given as an input to a filter matched to the template of the transmitted signal. The delay of its maximum corresponds to the estimated TOA, which is then used as input for the localization engine, as mentioned before.

The tag positioning system is depicted in Fig. 6.11 where one UWB transmitter and two receivers have been placed in known positions for providing the tag positioning. By referring to receiver 1 (namely, RX1), once the TOA is computed, the localization engine can evaluate the sum of distances for the tag-transmitter and tag-receiver links, respectively, that is  $d_{Tx} + d_1$ , corresponding to the round-trip time of the UWB signal. From a geometrical point-of-view, the computed sum distance is constant, and it describes an ellipse of potential tag positions whose foci are the transmitter and the considered receiver, i.e., RX1. This ellipse is depicted in blue in Fig. 6.11. Since the tag can be in any location belonging to the blue ellipse, in order to estimate its position, ambiguity must be solved. For this reason, there is another receiver (RX2), that together with the transmitter and by repeating the same steps as before, can create a second ellipse of potential tag positions, indicated as a green ellipse in Fig. 6.11, that intercepts the first one in just two locations. Hence, in this example, two intersection points can be found and can be associated to the tag position. By exploiting a prior knowledge of the considered indoor environment (for example, a map of the room), it is possible to disambiguate between the two points and to keep only one of them as tag estimate.

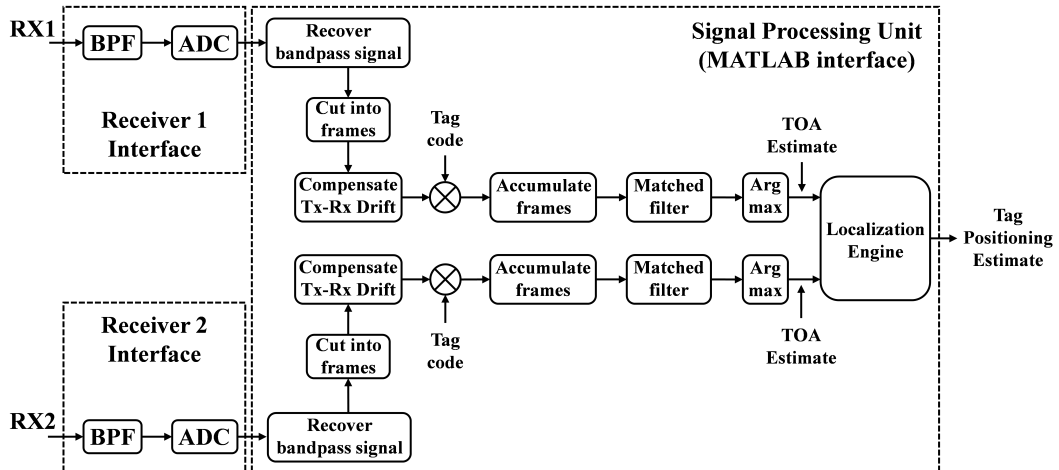


Figure 6.10: Signal processing algorithm.

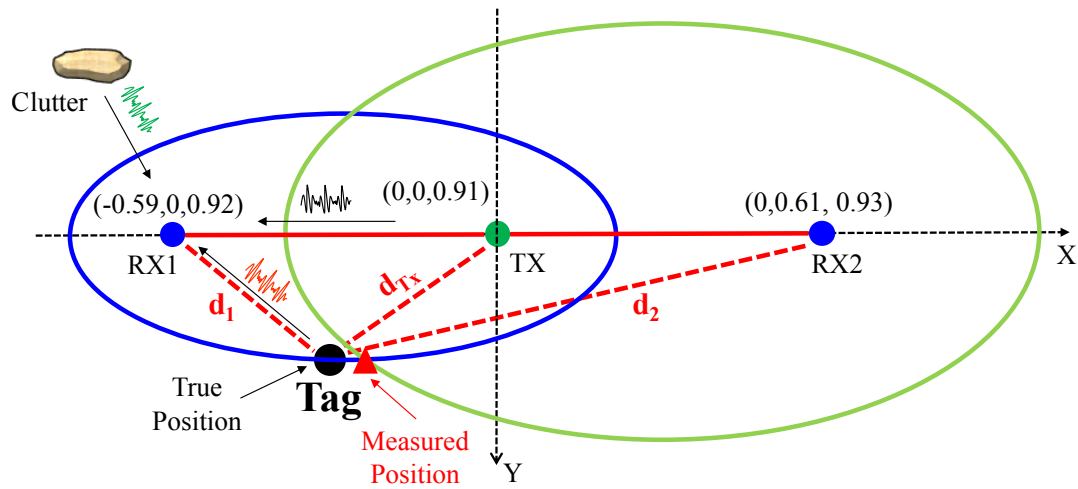


Figure 6.11: Positioning of backscattering tags.

### 6.2.2 Localization performance

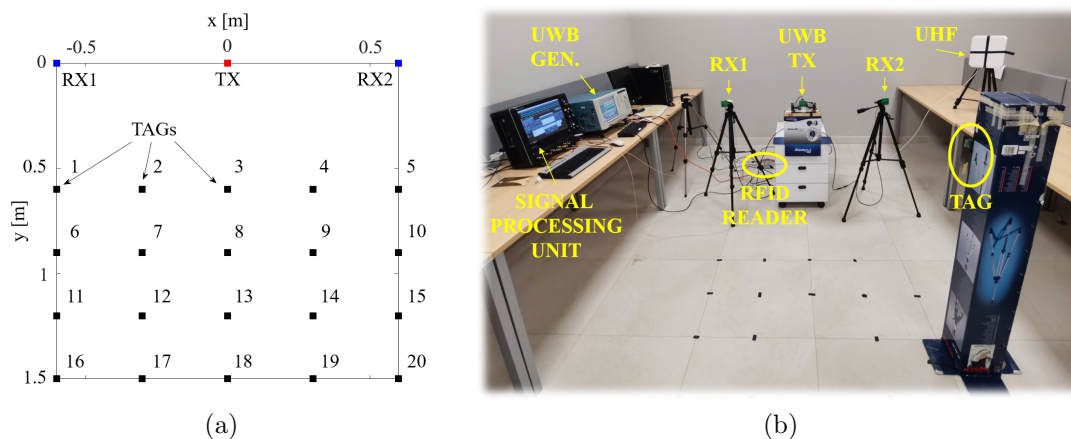


Figure 6.12: Localization of backscattering tags. (a) Scenario of 20 tags position (b) Test bench for measurements.

The Localization scenario is depicted in Fig. 6.12(a) and physically represented in Fig. 6.12(b). The UWB transmitting antenna was located at the origin of the reference coordinate system, and the receiving antennas along the x-axis both with a distance of 60 cm from the transmitter. A tag was moved in a grid of 20 points spaced of 30 cm and represented as black squares. The considered tag was deployed at the same height of the circularly polarized UWB transmitting/receiving

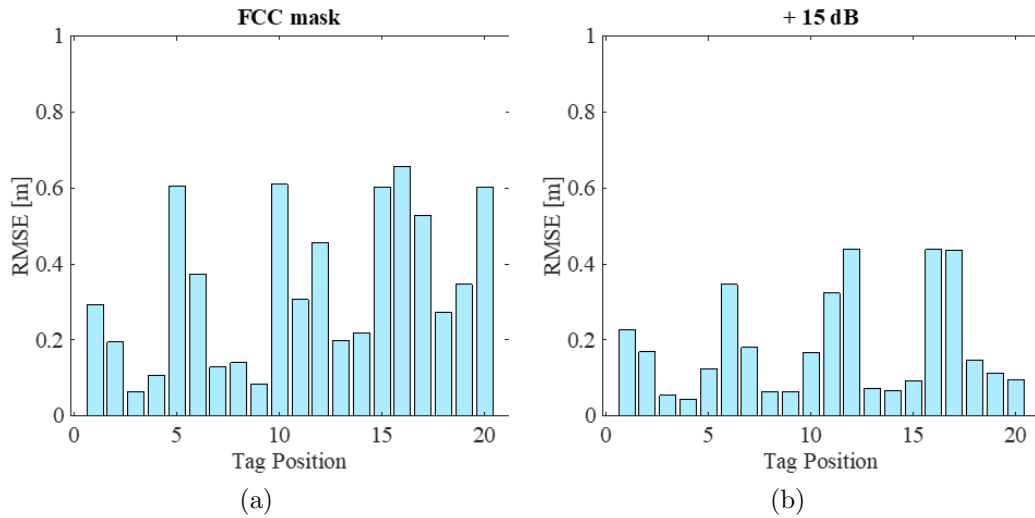


Figure 6.13: Tag Localization Root Mean Square Error (RMSE) for both measurements (a) FCC compliant and (b) power boost of +15 dB over the mask.

antennas and it was oriented parallel to the XZ-plane. All the tag positions have been characterized in terms of localization estimation error.

In particular, the root mean squared error (RMSE) is reported (Fig. 6.13) as a function of the tag position in the FCC compliant case (-41.3 dBm/MHz) or with an extra power boost of +15 dB over the mask. The error was averaged over 20 measurements for all positions and for some of them it is lower than 10 cm. Results indicate that an overall good localization accuracy can be obtained.

To better characterize the system performance, It has been computed the empirical cumulative density function (Fig. 6.14) as a function of the localization error. It was averaged over the number of measurements and number of tag positions. Here, It is possible to notice that for the 70 % of cases the error is below 40 cm, when FCC mask is respected, and lower than 20 cm with 15 dB over the mask. The overall accuracy achieves good results in both cases. The node can be wirelessly switched on and localized from the UWB source, up to 1.5 m (within the FCC mask limitation) and up to 2.5 m (with the extra boost of power).

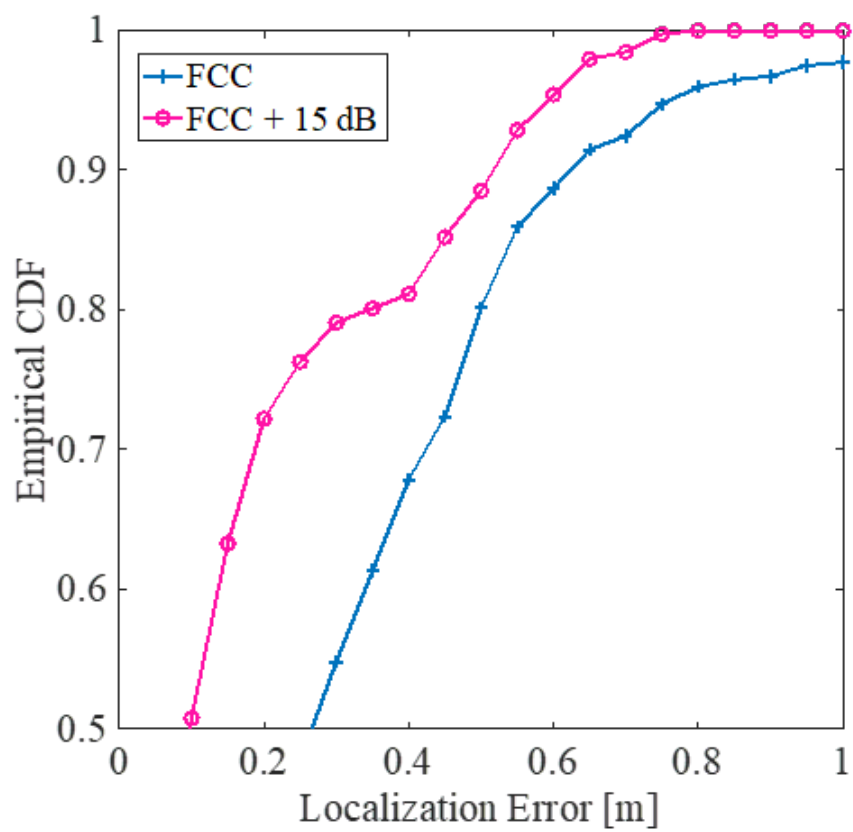


Figure 6.14: Empirical CDF.



# Chapter 7

## Conclusion and final remarks

The thesis work led to the study of the state of the art on energy harvesting topologies available and suitable in literature, in order to build Energy Autonomous devices, mainly with the purpose of serving battery-free applications for the environmental safeguard. Hence, to properly cover most of the possible real scenarios, radio-frequency and light sources have been hardly investigated to propose concrete solutions for building energy-efficient nodes.

In this sense, as shown in the second Chapter, low power strategies and policies are necessary conditions for the implementation of passive tags where only few  $\mu\text{W}$  are available as power source. Starting from these considerations the dissertation presented PV passive tags specifically designed for Wireless Sensor Networks which are used in both indoor and outdoor environments.

However, for all of those applications where Non-Line-Of-Sight conditions have to be satisfied, UHF radio-frequency source can be introduced for developing UHF battery-free tags, for sensing and localization applications. In recent years we have assisted to an increasing interest in localizing objects and persons equipped with low-cost tags in indoor environments. The targeted applications are in the fields of logistics, retail, security, etc. Hence, according to the requirements and specifications, UHF single-monopole passive tags have been built, following two configurations based on UWB transmitting solution and UWB backscattering technology. The former can be energized and localized up to 10 meters with a Mean square error of 3.5 cm. Instead, the latter (based on UWB-RFID solution) achieves a localization distance of 2.5 meters, in the best case of extra-boost of power (+15 dB), with an error around 20 cm (70 % of cases). Obviously, the results obtained with the backscattering tag are affected by a poor power budget of the UWB link, which strongly reduces the localization performance, making this type of nodes suitable for shorter range applications compared to UWB transmitting tags.

On the other hand, from the energy harvesting point of view, the double-monopole have introduced several improvements allowing to reach a maximum

working distance of 21.9 meters (compared to 10.8 meters achieved by the single-monopole rectenna). These results confirm that the energy scavenging chain does not represent the main bottle-neck when localization systems are considered. However, significant updates can be actuated in the future steps. In principle, an ASIC implementation of the overall hardware architecture, besides new low-power input DC/DC converters, leads to have lower node leakage current consumption and thus, wider working distances. Moreover, since the transmitting tags have been designed through a UHF custom protocol, a multi-tag localization engine can be easily performed. In fact, all nodes can be addressed consecutively avoiding the presence of ambiguities. On the contrary, the multi-tag localization for UWB-RFID hybrid solution, represents a critical aspect, still not implemented. The tag to reader communication is managed by the EPC Gen 2 standard with a random access to the channel. Hence, the RFID readers have to issue not only the trigger for synchronizing the external UWB generator, but also provides the nodes identification code to the receiver interface, in order to perform the localization data to tag ID association. Unfortunately, RFID commercial readers used for nodes identification are closed systems with a limited number of allowed operations and not able to execute a strong customization. Thus, they will be replaced with open-source Software-Defined-Radio (SdR) which permits low-level design suitable for the required application.

# List of Figures

1.1	Electronic devices powered through Energy Harvesters. . . . .	2
1.2	General scenario of Radio-Frequency and Ambient Light Energy Autonomous systems. . . . .	6
1.3	Typical hardware architecture of RF Energy Autonomous nodes. . .	7
1.4	Typical hardware architecture of PV Energy Autonomous nodes. . .	10
1.5	Localization techniques for UHF-RFID tags. . . . .	12
1.6	UWB tag implementation based on (a) transmitting and (b) backscattering techniques. . . . .	14
2.1	Typical radio-frequency front-end for energy harvesting purposes. .	17
2.2	Multi-Stage Rectifier topology and performances. . . . .	18
2.3	Equivalent model of a rectifying antenna. . . . .	19
2.4	General scheme of a Wake-up radio system integrated with an energy harvesting interface. . . . .	20
2.5	Wake-up Radio architecture. . . . .	21
2.6	Correlator principle scheme. . . . .	23
2.7	Power management unit block scheme. . . . .	25
2.8	Dickson charge pump scheme and working principle. . . . .	26
2.9	Typical Buck-Boost convert scheme. . . . .	27
2.10	RF battery-less architecture with load power gating feature. . . . .	29
2.11	Duty-cycled operation mode. . . . .	30
2.12	Voltage monitor architecture. . . . .	31
2.13	Tag operation in Stand-by mode and off mode. . . . .	31
2.14	Tag hardware architecture with stand-by mode and off mode implementation. The solution is <i>Tag oriented complexity</i> . . . . .	32
2.15	Tag hardware architecture for optimized low power policies. The solution is <i>Reader oriented complexity</i> . . . . .	34
3.1	PV Tag hardware architecture for Wireless Sensor Networks. . . . .	36
3.2	Microcontroller firmware operation. . . . .	38
3.3	SPI data exchange followed by the RF packet transmission. . . . .	38

3.4	Measured load current consumption during the operation phases. . . . .	39
3.5	Multi energy harvesting source power conversion unit. . . . .	40
3.6	PCB design of the PV multi-source PMU with indoor solar cell. . . . .	41
3.7	PMU Start-up and duty-cycle operation with 200 Lux of light exposure. . . . .	41
3.8	Single energy harvesting source power conversion unit. . . . .	42
3.9	PCB design of the PV single-source PMU with outdoor solar cell. . . . .	43
3.10	Wireless sensor network of PV passive Tags for outdoor (Top) and indoor (Bottom) applications. . . . .	44
3.11	Outdoor measured temperature and humidity. . . . .	45
4.1	UHF battery-less transmitting tag. . . . .	48
4.2	UHF dual path rectenna. . . . .	49
4.3	Rectenna conversion efficiency and rectified voltage as function of the received power. . . . .	50
4.4	UHF-UWB passive Tag operation. . . . .	51
4.5	TI bq25570 power management unit configuration scheme. . . . .	53
4.6	Test scheme for power management unit characterization. . . . .	55
4.7	TI bq25570 PMU operation. . . . .	55
4.8	Maximum power point tracking (MPPT) of 50% of the input source, represented with a <i>red</i> color, while the rectified voltage is in <i>black</i> . . . . .	56
4.9	Tag addressed power consumption. . . . .	58
4.10	Tag not addressed power consumption. . . . .	58
4.11	Double-monopole Tag hardware architecture [180]. . . . .	59
4.12	Schematic view of the double-monopole rectenna [180]. . . . .	60
4.13	Radiation pattern of the horizontal monopole: (a) in absence, (b) in presence of the decoupling network [180]. . . . .	61
4.14	Test bench for measurements. . . . .	62
4.15	Graphical User Interface for Tag identification. . . . .	63
4.16	Wireless power transfer hardware scheme. . . . .	63
4.17	UHF wireless power transfer PCB board (realized within the collaboration activity with UCLouvain). . . . .	64
4.18	PCB design of the single-monopole tag. . . . .	65
4.19	Working distances of the UHF single monopole tag. . . . .	65
4.20	PCB design of the double-monopole tag. . . . .	66
4.21	Comparison between single and double-monopole working distances. . . . .	68
5.1	UHF-RFID tag hardware scheme [54]. . . . .	70
5.2	RFID Tag protocol operation. . . . .	71
5.3	Tag Inventory-round with $Q = 0$ , and Tag population set to 1, since there is only one node to identify [54]. . . . .	72
5.4	Reader to Tag communication parameters [54]. . . . .	72

5.5	Tag energy consumption profile. It has been supposed that the reader performs a Single Target Inventory in Session 0 [54]. . . . .	74
5.6	Test bench for the UHF-RFID tag performance measurements [54]. . . . .	77
5.7	Comparison between modelled and measured Tag duty-cycle and charge time [54]. . . . .	78
5.8	Comparison between measured and modelled battery-less tag read-rate as a function of the distance from the reader [54]. . . . .	79
5.9	Room temperature recording with UHF-RFID tag [54]. . . . .	79
5.10	Typical scenarios of RFID tags confined in a certain area (a) without localization (b) with RSSI-based localization and (c) with UWB-based localization. . . . .	80
5.11	Micro-power architectures for backscattering subsections of the tag based on (a) quartz oscillator (b) transistor oscillator and (c) MCU clock generation. . . . .	81
5.12	UWB-RFID backscattering tag scheme. . . . .	83
5.13	UWB-RFID backscattering tag PCB design. . . . .	83
6.1	ESA-LOST Tags localization scenario. . . . .	86
6.2	The double-correlation synchronization scheme [183][184]. . . . .	88
6.3	Signal processing scheme [183][184]. . . . .	90
6.4	Multi-tag quasi-real time localization performed at UCLouvain . In white characters, the main components of the system. . . . .	91
6.5	Cumulative error versus sorted experiment index for different integration times $T_w$ [183][184]. . . . .	91
6.6	(Left) Screenshot of the GUI as taken during the demo at ESA/ESTEC (Right) Robotics Lab with the Mars Rover prototype equipped with the UHF-UWB tag [183][184][185]. . . . .	93
6.7	(a) Measurement scenario with positions of four receivers (corners), calibration tag (bottom) and 11 test positions of the tag in 2D plane; (b) Empirical CDF of the localization error in three tag test positions [184]. . . . .	93
6.8	Backscattering Tags localization scenario. . . . .	94
6.9	Backscattering Tag operation. . . . .	95
6.10	Signal processing algorithm. . . . .	96
6.11	Positioning of backscattering tags. . . . .	97
6.12	Localization of backscattering tags. (a) Scenario of 20 tags position (b) Test bench for measurements. . . . .	97
6.13	Tag Localization Root Mean Square Error (RMSE) for both measurements (a) FCC compliant and (b) power boost of +15 dB over the mask. . . . .	98
6.14	Empirical CDF. . . . .	99



# Bibliography

- [1] Sravanthi Chalasani and J. M. Conrad, "A survey of energy harvesting sources for embedded systems", IEEE SoutheastCon 2008, Huntsville, AL, 2008, pp. 442-447, <http://dx.doi.org/10.1109/SECON.2008.4494336>.
- [2] C. R. Valenta and G. D. Durgin, "Harvesting Wireless Power: Survey of Energy-Harvester Conversion Efficiency in Far-Field, Wireless Power Transfer Systems", IEEE Microwave Magazine, vol. 15, no. 4, pp. 108-120, June 2014, <http://dx.doi.org/10.1109/MMM.2014.2309499>.
- [3] D. Ma, G. Lan, M. Hassan, W. Hu and S. K. Das, "Sensing, Computing, and Communications for Energy Harvesting IoTs: A Survey", IEEE Communications Surveys & Tutorials, vol. 22, no. 2, pp. 1222-1250, Secondquarter 2020, <http://dx.doi.org/10.1109/COMST.2019.2962526>.
- [4] S. Sudevalayam and P. Kulkarni, "Energy Harvesting Sensor Nodes: Survey and Implications", IEEE Communications Surveys & Tutorials, vol. 13, no. 3, pp. 443-461, Third Quarter 2011, <http://dx.doi.org/10.1109/SURV.2011.060710.00094>.
- [5] G. Frantz, "Digital signal processor trends", IEEE Micro, vol. 20, no. 6, pp. 52-59, Nov.-Dec. 2000, <http://dx.doi.org/10.1109/40.888703>.
- [6] R. R. Schaller, "Moore's law: past, present and future", IEEE Spectrum, vol. 34, no. 6, pp. 52-59, June 1997, <http://dx.doi.org/10.1109/6.591665>.
- [7] Jeong Min Baik and Jin Pyo Lee, "Strategies for ultrahigh outputs generation in triboelectric energy harvesting technologies: from fundamentals to devices, Science and Technology of Advanced Materials", Science and Technology of Advanced Materials, 20:1, 927-936, 2019, <http://dx.doi.org/10.1080/14686996.2019.1655663>.
- [8] Mclean, Alexandria Virginia, Marin S. Halper and J. Ellenbogen. "Supercapacitors : A Brief Overview.", Materials Science, 2006.

- [9] ITU-T Rec. Y.2060, "*Overview of the Internet of Things*", 2012, <http://handle.itu.int/11.1002/1000/11559>
- [10] S. Singh and N. Singh, "*Internet of Things (IoT): Security challenges, business opportunities & reference architecture for E-commerce*", International Conference on Green Computing and Internet of Things (ICGCIoT), Noida, 2015, pp. 1577-1581, <http://dx.doi.org/10.1109/ICGCIoT.2015.7380718>.
- [11] Chen Min, Wan Jiafu, and Li Fang, "*Machine-to-Machine Communications: Architectures, Standards and Applications*", KSII Transactions on Internet and Information Systems, 2012, <http://dx.doi.org/10.3837/tiis.2012.02.002>.
- [12] Vullers R.J.M., van Schaijk R., Doms, I., van Hoof C., and Mertens R., "*Micropower energy harvesting*", Solid-State Electron, 2009, 53, 684–693, <https://dx.doi.org/10.1016/j.sse.2008.12.011>.
- [13] Lu X., Wang P., Niyato D., Kim D.I. and Han Z, "*Wireless networks with RF energy harvesting: A contemporary survey*", IEEE Commun. Surv. Tutor. 2015, 17, 757–789, <https://dx.doi.org/10.1109/COMST.2014.2368999>.
- [14] Mario W. Cardullo, *Transponder apparatus and system*, U.S. Patent 3713148A, Jan. 23, 1973, <https://patents.google.com/patent/US3713148A/en>.
- [15] Charles Walton, *Portable radio frequency emitting identifier*, U.S. Patent 4384288A, May 17, 1983, <https://patents.google.com/patent/US4384288A/en>.
- [16] J. Garnica, R. A. Chinga, and J. Lin, "*Wireless Power Transmission: From Far Field to Near Field*", Proc. IEEE, vol. 101, pp. 1321–1331, June 2013, <https://dx.doi.org/10.1109/JPROC.2013.2251411>.
- [17] A. W. Green and J. T. Boys, "*10 kHz inductively coupled power transfer-concept and control*", Fifth International Conference on Power Electronics and Variable-Speed Drives, pp. 694–699, Oct 1994, <https://dx.doi.org/10.1049/cp:19941049>.
- [18] S. Y. R. Hui and W. W. C. Ho, "*A new generation of universal contactless Battery Charging platform for portable Consumer Electronic equipment*" IEEE Trans. Power Electron., vol. 20, pp. 620–627, May 2005, <https://dx.doi.org/10.1109/PESC.2004.1355823>.
- [19] G. A. Covic and J. T. Boys, "*Inductive Power Transfer*", Proc. IEEE, vol. 101, pp. 1276–1289, June 2013, <https://dx.doi.org/10.1109/JPROC.2013.2244536>.

- [20] C.-S. Wang, O. H. Stielau, and G. A. Covic, “*Design considerations for a contactless electric vehicle battery charger*”, IEEE Trans. Ind. Electron., vol. 52, pp. 1308–1314, Oct 2005, <https://dx.doi.org/10.1109/TIE.2005.855672>.
- [21] W. C. Brown, “*An experimental low power density rectenna*”, IEEE MTT-S International Microwave Symposium Digest, pp. 197–200 vol.1, July 1991, <https://dx.doi.org/10.1109/MWSYM.1991.146961>
- [22] N. Shinohara and H. Matsumoto, “*Experimental study of large rectenna array for microwave energy transmission*”, IEEE Trans. Microw. Theory Techn., vol. 46, pp. 261–268, Mar 1998, [https://doi.org/10.1002/1520-6432\(200102\)84:2<27::AID-ECJB4>3.0.CO;2-C](https://doi.org/10.1002/1520-6432(200102)84:2<27::AID-ECJB4>3.0.CO;2-C)
- [23] J. A. Hagerty, F. B. Helmbrecht, W. H. McCalpin, R. Zane, and Z. B. Popovic, “*Recycling ambient microwave energy with broadband rectenna arrays*”, IEEE Trans. Microw. Theory Techn., vol. 52, pp. 1014–1024, March 2004, <https://doi.org/10.1109/TMTT.2004.823585>.
- [24] M. Piñuela, P. D. Mitcheson, and S. Lucyszyn, “*Ambient RF Energy Harvesting in Urban and Semi-Urban Environments*”, IEEE Trans. Microw. Theory Techn., vol. 61, pp. 2715–2726, July 2013, <https://doi.org/10.1109/TMTT.2013.2262687>.
- [25] Tanim M M Zaman, “*How does passive RFID works, briefly explained*”, 2016, <https://dx.doi.org/10.13140/RG.2.2.12361.34402>.
- [26] EN 300 330 V2.1.1, “*Short Range Devices (SRD); Radio equipment in the frequency range 9 kHz to 25 MHz and inductive loop systems in the frequency range 9 kHz to 30 MHz; Harmonised Standard covering the essential requirements of article 3.2 of Directive 2014/53/EU*”, 2016, [https://www.etsi.org/deliver/etsi\\_en/300300\\_300399/300330/02.01.01\\_30/en\\_300330v020101v.pdf](https://www.etsi.org/deliver/etsi_en/300300_300399/300330/02.01.01_30/en_300330v020101v.pdf).
- [27] ISO/IEC 18000-2, “*Information technology — Radio frequency identification for item management — Part 2: Parameters for air interface communications below 135 kHz*”, 2009, <https://www.iso.org/standard/46146.html>.
- [28] ISO/IEC 18092, “*Information technology — Telecommunications and information exchange between systems — Near Field Communication — Interface and Protocol (NFCIP-1)*”, 2013, <https://www.iso.org/standard/56692.html>.
- [29] TR 103 059 V1.1.1, “*Electromagnetic compatibility and Radio spectrum Matters (ERM); Short-Range Devices (SRD) for operation in the 13,56*

- MHz band; System Reference Document for Radio Frequency Identification (RFID) equipment*", 2012, [https://www.etsi.org/deliver/etsi\\_tr/103000\\_103099/103059/01.01.01\\_60/tr\\_103059v010101p.pdf](https://www.etsi.org/deliver/etsi_tr/103000_103099/103059/01.01.01_60/tr_103059v010101p.pdf)
- [30] ISO/IEC 15693-1, "*Cards and security devices for personal identification — Contactless vicinity objects — Part 1: Physical characteristics*", 2018, <https://www.iso.org/standard/70837.html>
- [31] ISO/IEC 15693-2, "*Cards and security devices for personal identification — Contactless vicinity objects — Part 2: Air interface and initialization*", 2019, <https://www.iso.org/standard/73601.html>.
- [32] ISO/IEC 15693-3, "*Cards and security devices for personal identification — Contactless vicinity objects — Part 3: Anticollision and transmission protocol*", 2019, <https://www.iso.org/standard/73602.html>.
- [33] ISO/IEC 14443-1, "*Cards and security devices for personal identification — Contactless proximity objects — Part 1: Physical characteristics*", 2018, <https://www.iso.org/standard/73596.html>.
- [34] ISO/IEC 14443-2, "*Cards and security devices for personal identification — Contactless proximity objects — Part 2: Radio frequency power and signal interface*", 2020, <https://www.iso.org/standard/73597.html>.
- [35] ISO/IEC 14443-3, "*Cards and security devices for personal identification — Contactless proximity objects — Part 3: Initialization and anticollision*", 2018, <https://www.iso.org/standard/73598.html>.
- [36] ISO/IEC 14443-4, "*Cards and security devices for personal identification — Contactless proximity objects — Part 4: Transmission protocol*", 2018, <https://www.iso.org/standard/73599.html>.
- [37] ISO/IEC 18000-7, "*Information technology — Radio frequency identification for item management — Part 7: Parameters for active air interface communications at 433 MHz*", 2014, <https://www.iso.org/standard/57336.html>.
- [38] EN 300 220-1 V2.4.1, "*Electromagnetic compatibility and Radio spectrum Matters (ERM); Short Range Devices (SRD); Radio equipment to be used in the 25 MHz to 1000 MHz frequency range with power levels ranging up to 500 mW; Part 1: Technical characteristics and test methods*", European Telecommunications Standards Institute (ETSI), 2012, [https://www.etsi.org/deliver/etsi\\_en/300200\\_300299/30022001/02.04.01\\_40/en\\_30022001v020401o.pdf](https://www.etsi.org/deliver/etsi_en/300200_300299/30022001/02.04.01_40/en_30022001v020401o.pdf)

- [39] EN 302 208 V3.2.0, "Radio Frequency Identification Equipment operating in the band 865 MHz to 868 MHz with power levels up to 2 W and in the band 915 MHz to 921 MHz with power levels up to 4 W; Harmonised Standard for access to radio spectrum", European Telecommunications Standards Institute (ETSI), 2018, [https://www.etsi.org/deliver/etsi\\_en/302200\\_302299/302208/03.02.00\\_20/en\\_302208v030200a.pdf](https://www.etsi.org/deliver/etsi_en/302200_302299/302208/03.02.00_20/en_302208v030200a.pdf)
- [40] EPC Gen 2 v 2.1, "EPC™ Radio-Frequency Identity Protocols Generation-2 UHF RFID Standard: Specification for RFID Air Interface Protocol for Communications at 860 MHz – 960 MHz", 2018, [https://www.gs1.org/sites/default/files/docs/epc/g1-epc-gen2v2-uhf-airinterface\\_i21\\_r\\_2018-09-04.pdf](https://www.gs1.org/sites/default/files/docs/epc/g1-epc-gen2v2-uhf-airinterface_i21_r_2018-09-04.pdf).
- [41] EN 300 328 V2.2.2, "Wideband transmission systems; data transmission equipment operating in the 2,4 GHz band; Harmonised Standard for access to radio spectrum", European Telecommunications Standards Institute (ETSI), 2019, [https://www.etsi.org/deliver/etsi\\_en/300300\\_300399/300328/02.02.02\\_60/en\\_300328v020202p.pdf](https://www.etsi.org/deliver/etsi_en/300300_300399/300328/02.02.02_60/en_300328v020202p.pdf)
- [42] ISO/IEC 18000-4, "Information technology — Radio frequency identification for item management — Part 4: Parameters for air interface communications at 2,45 GHz", 2018, <https://www.iso.org/standard/68145.html>.
- [43] Zeng Lei, Grau David and Xiao Yang, "Assessing the Feasibility of Passive and BAP RFID Communications on Construction Site Scenarios", IEEE Systems Journal. PP. 1-11, 2015, <https://dx.doi.org/10.1109/JSYST.2014.2369413>.
- [44] Ashwin Amanna, Wireless@vt Virginia, Agrawal Ambuj and Manteghi Majid, "Active RFID for Enhanced Railway Operations", American Society of Mechanical Engineers, Rail Transportation Division, 2010, <https://dx.doi.org/10.1115/RTDF2010-42006>.
- [45] D. Zhang, L. T. Yang, M. Chen, S. Zhao, M. Guo and Y. Zhang, "Real-Time Locating Systems Using Active RFID for Internet of Things", IEEE Systems Journal, vol. 10, no. 3, pp. 1226-1235, Sept. 2016, <https://dx.doi.org/10.1109/JSYST.2014.2346625>.
- [46] J. R. Smith, B. Jiang, S. Roy, M. Philipose, K. Sundara-Rajan and A. Mamishev, "ID Modulation: Embedding Sensor Data in a RFID Time-series", International Workshop on Information Hiding, Vol. 3727, Nov. 2005, [https://dx.doi.org/10.1007/11558859\\_18](https://dx.doi.org/10.1007/11558859_18).

- [47] A. P. Sample, D. J. Yeager, P. S. Powledge, J. R. Smith, “*Design of Passively-Powered, Programmable Sensing Platform for UHF RFID Systems*”, IEEE International Conference on RFID, Grapevine (TX, USA), March 2007, <https://dx.doi.org/10.1109/RFID.2007.346163>.
- [48] A. P. Sample, D. J. Yeager, P. S. Powledge, A. V. Mamishev, J. R. Smith, “*Design of an RFID-Based Battery-Free Programmable Sensing Platform*”, IEEE Transaction on Instrumentation and Measurement, Vol. 57, No. 11, Nov. 2008, <https://dx.doi.org/10.1109/TIM.2008.925019>.
- [49] Luca Catarinucci, Riccardo Colella and Luciano Tarricone, “*A Cost-Effective UHF RFID Tag for Transmission of Generic Sensor Data in Wireless Sensor Networks*”, IEEE Transactions on Microwave Theory and Techniques, (57)5, 1291 - 1296, 2009, <https://dx.doi.org/10.1109/TMTT.2009.2017296>.
- [50] N. Gay and W. Fischer, “*Ultra-low-power RFID-based sensor mote*”, IEEE SENSORS, 2010, pp. 1293-1298, <https://dx.doi.org/10.1109/ICSENS.2010.5690586>.
- [51] D. D. Donno, L. Catarinucci and L. Tarricone, “*RAMSES: RFID Augmented Module form Smart Environmental Sensing*”, IEEE Transaction on Instrumentation and Measurement, Vol. 63, No. 7, July 2014, <https://dx.doi.org/10.1109/TIM.2014.2298692>.
- [52] Monza X-2K Dura, “*UHF Gen2 RFID IC*”, <https://support.impinj.com/hc/en-us/articles/202756848-Monza-X-2K-Dura-Product-Brief-Datasheet>.
- [53] D. Fabbri, M. Pizzotti and A. Romani, “*Micropower Design of an Energy Autonomous RF Tag for UWB Localization Applications*”, IEEE International Symposium on Circuits and Systems (ISCAS), Florence, 2018, pp. 1-5, <https://dx.doi.org/10.1109/ISCAS.2018.8351353>.
- [54] D. Fabbri, E. Berthet-Bondet, D. Masotti, A. Costanzo, D. Dardari and A. Romani, “*Long Range Battery-Less UHF-RFID Platform for Sensor Applications*”, IEEE International Conference on RFID Technology and Applications (RFID-TA), Pisa, Italy, 2019, pp. 80-85, <https://dx.doi.org/10.1109/RFID-TA.2019.8892187>.
- [55] Fantuzzi M., Paolini G., Shanawani M., Costanzo A. and Masotti D., “*An orientation-independent UHF rectenna array with a unified matching and decoupling RF network*”, International Journal of Microwave and Wireless Technologies, 11(5-6), 490-500, <https://dx.doi.org/10.1017/S1759078719000229>.

- [56] Pizzotti M., Perilli L., Del Prete M., Fabbri D., Canegallo R., Dini M., Masotti D., Costanzo A., Franchi Scarselli E. and Romani A., "A Long-Distance RF-Powered Sensor Node with Adaptive Power Management for IoT Applications", *Sensors* 2017, 17, 1732, <https://doi.org/10.3390/s17081732>.
- [57] UHF RFID Gen 2 SL900A Sensory Tag IC, 2013, Available on: <https://ams.com/>.
- [58] EasyToLog RFID Tag, 2013, Available on: <https://www.caenrfid.com/en/>.
- [59] EVAL01-Fenix-RM temperature sensor board, Available on: <https://www.farsens.com>.
- [60] SPS1M002, Smart Passive Sensor for Direct Moisture Sensing, 2017, Available on: <https://www.onsemi.com>.
- [61] Smartrac DogBone sensor node, Available on: <https://www.smartrac-group.com/>.
- [62] G. Zhang, D. Wu, J. Jia, W. Gao, Q. Cai, W. Xiao, L. Yu, S. Tao and Qi Chu, "Architecture Characteristics and Technical Trends of UHF RFID Temperature Sensor Chip", *Active and Passive Electronic Components*, Article ID 9343241, 2018, <https://dx.doi.org/10.1155/2018/9343241>.
- [63] Narrijun Cho, Seong-Jun Song, Jae-Youl Lee, Sunyoung Kim, Shiho Kim and Hoi-Jun Yoo, "A  $8\text{-}\mu\text{W}/\text{W}$ ,  $0.3\text{-mm}/\text{sup } 2/$  RF-powered transponder with temperature sensor for wireless environmental monitoring", *IEEE International Symposium on Circuits and Systems*, Kobe, 2005, pp. 4763-4766 Vol. 5, <https://dx.doi.org/10.1109/ISCAS.2005.1465697>.
- [64] Magnus S, UHF-RFID chip with sensing capabilities, Available on: <https://axzon.com/>.
- [65] AS321X series, battery-less UHF-RFID chips with embedded sensors, Available on: <https://asygn.com/>.
- [66] J. Yin et al., "A System-on-Chip EPC Gen-2 Passive UHF RFID Tag With Embedded Temperature Sensor", *IEEE Journal of Solid-State Circuits*, vol. 45, no. 11, pp. 2404-2420, Nov. 2010, <https://dx.doi.org/10.1109/JSSC.2010.2072631>.
- [67] B. Wang, M. Law, J. Yi, C. Tsui and A. Bermak, "A  $-12.3\text{ dBm}$  UHF Passive RFID Sense Tag for Grid Thermal Monitoring", *IEEE Transactions on Industrial Electronics*, vol. 66, no. 11, pp. 8811-8820, Nov. 2019, <https://dx.doi.org/10.1109/TIE.2019.2891447>.

- [68] H. Lyu, Z. Wang and A. Babakhani, "A UHF/UWB Hybrid RFID Tag With a 51-m Energy-Harvesting Sensitivity for Remote Vital-Sign Monitoring", IEEE Transactions on Microwave Theory and Techniques, 2020, <https://dx.doi.org/10.1109/TMTT.2020.3017674>.
- [69] C. Tamburini, M. Pizzotti, M. Dini, M. Crescentini, M. Tartagni, A. Romani, F. Alimenti, M. Virili, P. Mezzanotte, L. Roselli, "A CMOS RF-Powered Tag with Sensing and Localization Capabilities", IEEE 23rd International Workshop on Computer Aided Modeling and Design of Communication Links and Networks (CAMAD), Barcelona, 2018, pp. 1-5, <https://dx.doi.org/10.1109/CAMAD.2018.8514974>.
- [70] Yang Li, Rida A., Vyas Rushi and Tentzeris Manos, "RFID Tag and RF Structures on a Paper Substrate Using Inkjet-Printing Technology", IEEE Transactions on Microwave Theory and Techniques, 55(12), pp. 2894-2901, 2008, <https://dx.doi.org/10.1109/TMTT.2007.909886>.
- [71] K. Koski, L. Sydänheimo, Y. Rahmat-Samii and L. Ukkonen, "Fundamental Characteristics of Electro-Textiles in Wearable UHF RFID Patch Antennas for Body-Centric Sensing Systems", IEEE Transactions on Antennas and Propagation, vol. 62, no. 12, pp. 6454-6462, Dec. 2014, <https://dx.doi.org/10.1109/TAP.2014.2364071>.
- [72] S. Shao, A. Kiourti, R. J. Burkholder and J. L. Volakis, "Broadband Textile-Based Passive UHF RFID Tag Antenna for Elastic Material", IEEE Antennas and Wireless Propagation Letters, vol. 14, pp. 1385-1388, 2015, <https://dx.doi.org/10.1109/LAWP.2015.2407879>.
- [73] D. Dardari, N. Decarli, A. Guerra, and F. Guidi, "The future of ultrawideband localization in RFID", Proc. IEEE Int. Conf. RFID (RFID), Orlando, FL, USA, May 2016, pp. 1-7, <https://dx.doi.org/10.1109/RFID.2016.7487998>.
- [74] D. Van Krevelen and R. Poelman, "A survey of augmented reality technologies, applications and limitations", Int. J. Virtual Real., vol. 9, no. 2, pp. 1-20, 2010, <https://dx.doi.org/10.20870/IJVR.2010.9.2.2767>.
- [75] D. Dardari, A. Conti, U. Ferner, A. Giorgetti, and M. Z. Win, "Ranging with ultrawide bandwidth signals in multipath environments", Proc. IEEE, vol. 97, no. 2, pp. 404-426, Feb. 2009, <https://dx.doi.org/10.1109/JPROC.2008.2008846>.
- [76] IEEE 802.15.4a, "IEEE Standard for Information technology- Local and metropolitan area networks- Specific requirements- Part 15.4: Wireless Medium

- Access Control (MAC) and Physical Layer (PHY) Specifications for Low-Rate Wireless Personal Area Networks (WPANs): Amendment 1: Add Alternate PHYs*", 2007, [https://standards.ieee.org/standard/802\\_15\\_4a-2007.html](https://standards.ieee.org/standard/802_15_4a-2007.html).
- [77] IEEE 802.15.4f, "*IEEE Standard for Local and metropolitan area networks—Part 15.4: Low-Rate Wireless Personal Area Networks (LR-WPANs) Amendment 2: Active Radio Frequency Identification (RFID) System Physical Layer (PHY)*", 2012, [https://standards.ieee.org/standard/802\\_15\\_4f-2012.html](https://standards.ieee.org/standard/802_15_4f-2012.html).
- [78] M. A. K. Jazairli and D. Flandre, "A 65 nm CMOS Ultra-Low-Power Impulse Radio-Ultra-Wideband Emitter for Short-Range Indoor Localization", *J. Low Power Electron.*, vol. 11, no. 3, pp. 349–358, Sep. 2015, <https://dx.doi.org/10.1166/jolpe.2015.1393>.
- [79] D. Dardari, R. D'Errico, C. Roblin, A. Sibille, and M. Z. Win, "Ultrawide bandwidth RFID: The next generation?", *Proc. IEEE*, vol. 98, no. 9, pp. 1570–1582, Sep. 2010, <https://dx.doi.org/10.1109/JPROC.2010.2053015>.
- [80] D. Dardari, E. Falletti, and M. Luise, "*Satellite and terrestrial radio positioning techniques—A signal processing perspective*", London, U.K.: Elsevier Ltd., 2011, p. 464.
- [81] D. Dardari, P. Closas, and P. M. Djurić, "*Indoor tracking: Theory, methods, and technologies*", *IEEE Trans. Veh. Technol.*, vol. 64, no. 4, pp. 1263–1278, Apr. 2015, <https://dx.doi.org/10.1109/TVT.2015.2403868>.
- [82] R. Miesen et al., "Where is the tag?", *IEEE Microw. Mag.*, vol. 12, no. 7, pp. S49–S63, Dec. 2011. <https://dx.doi.org/10.1109/MMM.2011.942730>.
- [83] M. Scherhäufel, M. Pichler, and A. Stelzer, "UHF RFID localization based on evaluation of backscattered tag signals", *IEEE Trans. Instrum. Meas.*, vol. 64, no. 11, pp. 2889–2899, Nov. 2015, <https://dx.doi.org/10.1109/TIM.2015.2440554>.
- [84] R. Miesen, F. Kirsch, and M. Vossiek, "Holographic localization of passive UHF RFID transponders", *Proc. IEEE Int. Conf. RFID*, Orlando, FL, USA, 2011, pp. 32–37, <https://dx.doi.org/10.1109/RFID.2011.5764633>.
- [85] L. Qiu, Z. Huang, N. Wirström, and T. Voigt, "3DinSAR: Object 3D localization for indoor RFID applications", *Proc. IEEE Int. Conf. RFID (RFID)*, Orlando, FL, USA, 2016, pp. 1–8, <https://dx.doi.org/10.1109/RFID.2016.7488026>.

- [86] P. V. Nikitin et al., “Phase based spatial identification of UHF RFID tags”, Proc. IEEE Int. Conf. RFID, Orlando, FL, USA, Apr. 2010, pp. 102–109, <https://dx.doi.org/10.1109/RFID.2010.5467253>.
- [87] R. Miesen, F. Kirsch, and M. Vossiek, “UHF RFID localization based on synthetic apertures”, IEEE Trans. Autom. Sci. Eng., vol. 10, no. 3, pp. 807–815, Jul. 2013. <https://dx.doi.org/10.1109/TASE.2012.2224656>.
- [88] E. DiGiampaolo and F. Martinelli, “sMobile robot localization using the phase of passive UHF RFID signal”, IEEE Trans. Ind. Electron., vol. 61, no. 1, pp. 365–376, Jan. 2014, <https://dx.doi.org/10.1109/TIE.2013.2248333>.
- [89] A. Buffi, P. Nepa, and F. Lombardini, “A phase-based technique for localization of UHF-RFID tags moving on a conveyor belt: Performance analysis and test-case measurements”, IEEE Sensors J., vol. 15, no. 1, pp. 387–396, Jan. 2015, <https://dx.doi.org/10.1109/JSEN.2014.2344713>.
- [90] D. Arnitz, K. Witrisal, and U. Muehlmann, “Multifrequency continuouswave radar approach to ranging in passive UHF RFID”, IEEE Trans. Microw. Theory Tech., vol. 57, no. 5, pp. 1398–1405, May 2009, <https://dx.doi.org/10.1109/TMTT.2009.2017320>.
- [91] D. Arnitz, U. Muehlmann, and K. Witrisal, “UWB ranging in passive UHF RFID: Proof of concept” IEEE Electron. Lett., vol. 46, no. 20, pp. 1401–1402, Sep. 2010, <https://dx.doi.org/10.1049/el.2010.1703>.
- [92] Impinji. (2017). Xarray RAIN RFID Gateway. [Online]. Available on: <https://www.impinj.com/products/readers/impinj-xseries-gateways>.
- [93] G. Hislop, N. Sakar, and C. Craeye, “Direction finding with MUSIC and CLEAN”, IEEE Trans. Antennas Propag., vol. 61, no. 7, pp. 3839–3849, Jul. 2013, <https://dx.doi.org/10.1109/TAP.2013.2255854>.
- [94] G. Hislop, D. Lekime, M. Drouguet, and C. Craeye, “A prototype 2D direction finding system with passive RFID tags”, Proc. EUCAP Conf., Barcelona, Spain, Apr. 2010, pp. 1–5, <https://ieeexplore.ieee.org/document/5505218>.
- [95] M. B. Nejad, “Ultra wideband impulse radio for wireless sensing and identification”, Ph.D. dissertation, Electron. Comput. Syst., KTH—Royal Inst. Technol., Stockholm, Sweden, Dec. 2008.
- [96] Z. Zou et al., “Design and demonstration of passive UWB RFIDs: Chipless versus chip solutions”, Proc. IEEE Int. Conf. RFID-Technol. Appl. (RFID-TA), Nice, France, Nov. 2012, pp. 6–11, <https://dx.doi.org/10.1109/RFID-TA.2012.6404570>.

- [97] J. Kang, S. Rao, P. Chiang, and A. Natarajan, “*Design and optimization of area-constrained wirelessly powered CMOS UWB SoC for localization applications*”, IEEE Trans. Microw. Theory Techn., vol. 64, no. 4, pp. 1042–1054, Apr. 2016, <https://dx.doi.org/10.1109/TMTT.2016.2536663>.
- [98] A. Ramos, A. Lazaro, and D. Girbau, “*Semi-passive time-domain UWB RFID system*”, IEEE Trans. Microw. Theory Techn., vol. 61, no. 4, pp. 1700–1708, Apr. 2013, <https://dx.doi.org/10.1109/TMTT.2013.2247056>.
- [99] F. Guidi, C. Roblin, A. Sibille, V. Casadei, and D. Dardari, “*Analysis of UWB tag backscattering and its impact on the detection coverage*”, IEEE Trans. Antennas Propag., vol. 62, no. 8, pp. 4292–4303, Aug. 2014, <https://dx.doi.org/10.1109/TAP.2014.2326179>.
- [100] A. Mallat et al., “*Testbed for IR-UWB based ranging and positioning: Experimental performance and comparison to CRLBs*”, Proc. 5th IEEE Int. Symp. Wireless Pervasive Comput. (ISWPC), Modena, Italy, May 2010, pp. 163–168, <https://dx.doi.org/10.1109/ISWPC.2010.5483707>.
- [101] F. Guidi et al., “*A low complexity scheme for passive UWB-RFID: Proof of concept*”, IEEE Commun. Lett., vol. 20, no. 4, pp. 676–679, Apr. 2016, <https://dx.doi.org/10.1109/LCOMM.2016.2530658>.
- [102] N. Decarli et al., “*The GRETA architecture for energy efficient radio identification and localization*”, Proc. Int. EURASIP Workshop RFID Technol. (EURFID), Rosenheim, Germany, Oct. 2015, pp. 1–8, <https://dx.doi.org/10.1109/EURFID.2015.7332377>.
- [103] N. Decarli, F. Guidi, and D. Dardari, “*Passive UWB RFID for tag localization: Architectures and design*”, IEEE Sensors J., vol. 16, no. 5, pp. 1385–1397, Mar. 2016, <https://dx.doi.org/10.1109/JSEN.2015.2497373>.
- [104] A. Mallat, S. Gezici, D. Dardari, C. Craeye, and L. Vandendorpe, “*Statistics of the MLE and approximate upper and lower bounds—Part I: Application to TOA estimation*”, IEEE Trans. Signal Process., vol. 62, no. 21, pp. 5663–5676, Nov. 2014, <https://dx.doi.org/10.1109/TSP.2014.2355771>.
- [105] J. Essel, D. Brenk, J. Heidrich, and R. Weigel, “*A highly efficient UHF RFID frontend approach*”, Proc. IEEE MTT-S Int. Microw. Workshop Wireless Sensing Local Position. RFID, Cavtat, Croatia, 2009, pp. 1–4, <https://dx.doi.org/10.1109/IMWS2.2009.5307866>.

- [106] C. R. Valenta, M. M. Morys, and G. D. Durgin, “*Theoretical energy-conversion efficiency for energy-harvesting circuits under power-optimized waveform excitation*”, IEEE Trans. Microw. Theory Techn., vol. 63, no. 5, pp. 1758–1767, May 2015, <https://dx.doi.org/10.1109/TMTT.2015.2417174>.
- [107] Quddious Abdul, Antoniadis Marco and Nikolaou Symeon, “*Voltage-Doubler RF-to-DC Rectifiers for Ambient RF Energy Harvesting and Wireless Power Transfer Systems*”, Wireless Energy Transfer Technology (Book), Publisher: IntechOpen, 2019, <https://dx.doi.org/10.5772/intechopen.89271>.
- [108] Colaiuda Davide, Ulisse Iolanda and Ferri Giuseppe. “*Rectifiers’ Design and Optimization for a Dual-Channel RF Energy Harvester*”, Journal of Low Power Electronics and Applications, 2020, <https://dx.doi.org/10.11.10.3390/jlpea10020011>.
- [109] C. Chung, Y. Kim, T. Ki, K. Bae and J. Kim, “*Fully integrated ultra-low-power 900 MHz RF transceiver for batteryless wireless microsystems*”, 18th IEEE International Conference on Electronics, Circuits, and Systems, Beirut, 2011, pp. 196-199, <https://dx.doi.org/10.1109/ICECS.2011.6122247>.
- [110] S. M. Noghabaei, R. L. Radin, Y. Savaria and M. Sawan, “*A High-Efficiency Ultra-Low-Power CMOS Rectifier for RF Energy Harvesting Applications*”, IEEE International Symposium on Circuits and Systems (ISCAS), Florence, 2018, pp. 1-4, <https://dx.doi.org/10.1109/ISCAS.2018.8351149>.
- [111] A. K. Moghaddam, J. H. Chuah, H. Ramiah, J. Ahmadian, P. Mak and R. P. Martins, “*A 73.9%-Efficiency CMOS Rectifier Using a Lower DC Feeding (LDCF) Self-Body-Biasing Technique for Far-Field RF Energy-Harvesting Systems*”, IEEE Transactions on Circuits and Systems I: Regular Papers, vol. 64, no. 4, pp. 992-1002, April 2017, <https://dx.doi.org/10.1109/TCSI.2016.2623821>.
- [112] M. H. Ouda, W. Khalil and K. N. Salama, “*Wide-Range Adaptive RF-to-DC Power Converter for UHF RFIDs*”, IEEE Microwave and Wireless Components Letters, vol. 26, no. 8, pp. 634-636, Aug. 2016, <https://dx.doi.org/10.1109/LMWC.2016.2586077>.
- [113] Z. Hameed and K. Moez, “*Hybrid Forward and Backward Threshold-Compensated RF-DC Power Converter for RF Energy Harvesting*”, IEEE Journal on Emerging and Selected Topics in Circuits and Systems, vol. 4, no. 3, pp. 335-343, Sept. 2014, <https://dx.doi.org/10.1109/JETCAS.2014.2337211>.

- [114] P. Saffari, A. Basaligheh and K. Moez, "An RF-to-DC Rectifier With High Efficiency Over Wide Input Power Range for RF Energy Harvesting Applications", IEEE Transactions on Circuits and Systems I: Regular Papers, vol. 66, no. 12, pp. 4862-4875, Dec. 2019, <https://dx.doi.org/10.1109/TCSI.2019.2931485>.
- [115] A. Costanzo et al., "Energy Autonomous UWB Localization", IEEE Journal of Radio Frequency Identification, vol. 1, no. 3, pp. 228-244, Sept. 2017, <https://dx.doi.org/10.1109/JRFID.2018.2792538>.
- [116] M. Fantuzzi, M. Del Prete, D. Masotti and A. Costanzo, "Quasi-isotropic RF energy harvester for autonomous long distance IoT operations", IEEE MTT-S International Microwave Symposium (IMS), Honolulu, HI, 2017, pp. 1345-1348, <https://dx.doi.org/10.1109/MWSYM.2017.8058861>.
- [117] R. Piyare, , C. Kiraly , P. Tosato, "Ultra Low Power Wake-Up Radios: A Hardware and Networking Survey", IEEE Communication Surveys & tutorials, 2017, <https://dx.doi.org/10.1109/COMST.2017.2728092>.
- [118] B. V. der Doorn, W. Kavelaars, and K. Langendoen, "A Prototype Low cost Wakeup Radio for the 868 MHz Band", International Journal of Sensor Networks, vol. 5, no. 1, pp. 22–32, 2009, <https://dx.doi.org/10.1504/IJSNET.2009.023313>
- [119] J. Oller, I. Demirkol, J. Casademont, and J. Paradells, "Design, development, and performance evaluation of a low-cost, low-power wakeup radio system for wireless sensor networks", ACM Transactions on Sensor Networks (TOSN), vol. 10, no. 1, pp. 1–24, 2013, <https://dx.doi.org/10.1145/2529452>
- [120] T. V. Prabhakar, N. S. Soumya, P. Muralidharan, and H. S. Jamadagni, "A Novel Wake-Up Radio WSN Mote", India Educators' Conference (TIIEC), 2013 Texas Instruments, April 2013, pp. 362–368, <https://dx.doi.org/10.1109/TIIEC.2013.71>.
- [121] J. Oller, E. Garcia, E. Lopez, I. Demirkol, J. Casademont, J. Paradells, U. Gamm, and L. Reindl, "IEEE 802.11-enabled wake-up radio system: design and performance evaluation", Electronics Letters, vol. 50, no. 20, pp. 1484–1486, September 2014, <https://dx.doi.org/10.1049/el.2014.2468>.
- [122] D. Spenza, M. Magno, S. Basagni, L. Benini, M. Paoli, and C. Petrioli, "Beyond duty cycling: Wake-up radio with selective awakenings for long-lived wireless sensing systems", IEEE Conference on Computer Communications (INFOCOM), April 2015, pp. 522–530, <https://dx.doi.org/10.1109/INFOCOM.2015.7218419>.

- [123] S. Bdiri and F. Derbel, “A nanowatt Wake-Up Receiver for industrial production line”, Systems, Signals Devices (SSD), 2014 11th International Multi-Conference on, Feb 2014, pp. 1–6, <https://dx.doi.org/10.1109/SSD.2014.6808911>.
- [124] J. Robert, T. Lindner, and H. Milosiu, “Sub 10  $\mu$ W wake-up-receiver based indoor/outdoor asset tracking system”, Emerging Technologies Factory Automation (ETFa), IEEE 20th Conference on, Sept 2015, pp.1–3, <https://dx.doi.org/10.1109/ETFa.2015.7301613>.
- [125] M. Magno, V. Jelcic, B. Srbinovski, V. Bilas, E. Popovici, and L. Benini, “Design, Implementation, and Performance Evaluation of a Flexible Low-Latency Nanowatt Wake-Up Radio Receiver”, IEEE Transactions on Industrial Informatics, vol. 12, no. 2, pp. 633–644, April 2016, <https://dx.doi.org/10.1109/TII.2016.2524982>.
- [126] F. Sutton, B. Buchli, J. Beutel, and L. Thiele, “Zippy: On-Demand Network Flooding”, Proceedings of the 13th ACM Conference on Embedded Networked Sensor Systems (SenSys). New York, NY, USA: ACM, 2015, pp. 45–58, <https://dx.doi.org/10.1145/2809695.2809705>.
- [127] A. S. Boaventura and N. B. Carvalho, “A Low-power Wakeup Radio for Application in WSN-based Indoor Location Systems”, International Journal of Wireless Information Networks, vol. 20, no. 1, pp. 67–73, 2013, <https://dx.doi.org/10.1007/s10776-012-0183-3>.
- [128] C. Petrioli, D. Spenza, P. Tommasino, and A. Trifiletti, “A novel wake-up receiver with addressing capability for wireless sensor nodes”, Proceedings of the 2014 IEEE International Conference on Distributed Computing in Sensor Systems (DCOSS). Washington, DC, USA: IEEE Computer Society, 2014, pp. 18–25, <https://dx.doi.org/10.1109/DCOSS.2014.9>.
- [129] J. Oller, I. Demirkol, J. Casademont, J. Paradells, G. Gamm, and L. Reindl, “Performance Evaluation and Comparative Analysis of SubCarrier Modulation Wake-up Radio Systems for Energy-Efficient Wireless Sensor Networks”, Sensors, vol. 14, no. 1, p. 22, 2014, <https://dx.doi.org/10.3390/s14010022>.
- [130] J. Petäjäjärvi, K. Mikhaylov, R. Vuhtoniemi, H. Karvonen, and J. Iinatti, “On the human body communications: wake-up receiver design and channel characterization”, EURASIP Journal on Wireless Communications and Networking, vol. 2016, no. 1, p. 179, 2016, <https://dx.doi.org/10.1186/s13638-016-0674-5>.

- [131] C. Hambeck, S. Mahlknecht, and T. Herndl, “A  $2.4 \mu W$  Wake-up Receiver for wireless sensor nodes with  $-71 dBm$  sensitivity”, IEEE International Symposium of Circuits and Systems (ISCAS). IEEE, May 2011, pp. 534–537, <https://dx.doi.org/10.1109/ISCAS.2011.5937620>
- [132] D. Y. Yoon, C. J. Jeong, J. Cartwright, H. Y. Kang, S. K. Han, N. S. Kim, D. S. Ha, and S. G. Lee, “A New Approach to Low-Power and Low-Latency Wake-Up Receiver System for Wireless Sensor Nodes”, IEEE Journal of Solid-State Circuits, vol. 47, no. 10, pp. 2405–2419, Oct 2012, <https://dx.doi.org/10.1109/JSSC.2012.2209778>
- [133] R. van Langevelde, M. van Elzakker, D. van Goor, H. Termeer, J. Moss, and A. J. Davie, “An ultra-low-power 868/915 MHz RF transceiver for wireless sensor network applications”, IEEE Radio Frequency Integrated Circuits Symposium, June 2009, pp. 113–116, <https://dx.doi.org/10.1109/RFIC.2009.5135502>.
- [134] T. Takiguchi, S. Saruwatari, T. Morito, S. Ishida, M. Minami, and H. Morikawa, “A Novel Wireless Wake-Up Mechanism for Energy-Efficient Ubiquitous Networks”, IEEE International Conference on Communications Workshops, June 2009, pp. 1–5, <https://dx.doi.org/10.1109/ICCW.2009.5208044>.
- [135] S. Drago, D. M. W. Leenaerts, F. Sebastiano, L. J. Breems, K. A. A. Makinwa, and B. Nauta, “A  $2.4 GHz$   $830 pJ/bit$  duty-cycled wakeup receiver with  $-82 dBm$  sensitivity for crystal-less wireless sensor nodes”, Solid-State Circuits Conference Digest of Technical Papers (ISSCC), IEEE International, Feb 2010, pp. 224–225, <https://dx.doi.org/10.1109/ISSCC.2010.5433955>.
- [136] Y. Zhang, S. Chen, N. F. Kiyani, G. Dolmans, J. Huisken, B. Busze, P. Harpe, N. van der Meijs, and H. de Groot, “A  $3.72 \mu W$  Ultralow Power Digital Baseband for Wake-up Radios”, VLSI Design, Automation and Test (VLSI-DAT), International Symposium on, April 2011, pp. 1–4, <https://dx.doi.org/10.1109/VDAT.2011.5783586>.
- [137] S. Tang, H. Yomo, Y. Kondo, and S. Obana, “Wake-up receiver for radio-on-demand wireless LANs”, EURASIP Journal on Wireless Communications and Networking, vol. 2012, no. 1, pp. 1–13, 2012, <https://dx.doi.org/10.1109/GLOCOM.2011.6133533>.
- [138] H. Jiang, Po-Han Peter Wang, Li Gao, Pinar Sen, Young-Han Kim, G. M. Rebeiz, D. A. Hall P. P. Mercier, “A  $4.5 nW$  Wake-Up Radio with  $-69 dBm$

- Sensitivity*”, IEEE International Solid-State Circuits Conference, ISSCC 2017, <https://dx.doi.org/10.1109/ISSCC.2017.7870438>.
- [139] S. von der Mark and G. Boeck, “*Ultra low power wakeup detector for sensor networks*”, Microwave and Optoelectronics Conference, IMOC 2007. SB-MO/IEEE MTT-S International, Oct 2007, pp. 865–868, <https://dx.doi.org/10.1109/IMOC.2007.4404394>.
- [140] C. Tzschoppe, R. Kostack, and F. Ellinger, “*A 2.4 GHz fast settling wake-up receiver frontend*”, Microelectronics and Electronics (PRIME), 10th Conference on Ph.D. Research in. IEEE, June 2014, pp. 1–4, <https://dx.doi.org/10.1109/PRIME.2014.6872707>.
- [141] H. Milosiu, F. Oehler, M. Eppel, D. Fruhsorger, S. Lensing, G. Popken, and T. Thones, “*A 3- $\mu$ W 868-MHz wake-up receiver with -83 dBm sensitivity and scalable data rate*”, ESSCIRC, 2013 Proceedings of the, Sept 2013, pp. 387–390, <https://dx.doi.org/10.1109/ESSCIRC.2013.6649154>.
- [142] S. Moazzeni, M. Sawan, and G. E. R. Cowan, “*An Ultra-Low-Power Energy-Efficient Dual-Mode Wake-Up Receiver*”, IEEE Transactions on Circuits and Systems I: Regular Papers, vol. 62, no. 2, pp. 517– 526, Feb 2015, <https://dx.doi.org/10.1109/TCSI.2014.2360336>.
- [143] S. Oh, N. E. Roberts, and D. D. Wentzloff, “*A 116 nW multi-band wake-up receiver with 31-bit correlator and interference rejection*”, Custom Integrated Circuits Conference (CICC), IEEE, Sept 2013, pp. 1–4, <https://dx.doi.org/10.1109/CICC.2013.6658500>.
- [144] S. J. Marinkovic, M. Popovici, “*Nano-Power Wireless Wake-Up Receiver With Serial Peripheral Interface*”, IEEE Journal on Selected areas in Communications, Vol. 29, No. 8, September 2011, <https://dx.doi.org/10.1109/JSAC.2011.110913>.
- [145] M. D. Prete, D. Masotti, A. Costanzo, M. Magno, and L. Benini, “*A 2.4 GHz-868 MHz dual-band wake-up radio for wireless sensor network and IoT*”, Wireless and Mobile Computing, Networking and Communications (WiMob), IEEE 11th International Conference on, Oct 2015, pp. 322–328, <https://dx.doi.org/10.1109/WiMOB.2015.7347979>.
- [146] N. E. Roberts, D.D. Wentzloff, “*A 98 nW Wake-up Radio for Wireless Body Area Networks*”, IEEE Radio Frequency Integrated Circuits Symposium, Montreal, 2012, <https://dx.doi.org/10.1109/RFIC.2012.6242302>.

- [147] M.-T. Hoang, N. Sugii, and K. Ishibashi, “A  $1.36 \mu W$  312-315 MHz Synchronized-OOK Receiver for Wireless Sensor Networks using 65 nm SOTB CMOS Technology”, *Solid-State Electronics*, vol. 117, pp. 161 – 169, 2016, <https://dx.doi.org/10.1016/j.sse.2015.11.016>.
- [148] T. Abe, T. Morie, K. Satou, D. Nomasaki, S. Nakamura, Y. Horiuchi, and K. Imamura, “An ultra-low-power 2-step wake-up receiver for IEEE 802.15.4g wireless sensor networks”, *VLSI Circuits Digest of Technical Papers, Symposium on*, June 2014, pp. 1–2, <https://dx.doi.org/10.1109/VLSIC.2014.6858382>.
- [149] S. E. Chen, C. L. Yang, and K. W. Cheng, “A  $4.5 \mu W$  2.4 GHz Wakeup Receiver Based on Complementary Current-reuse RF Detector”, *Circuits and Systems (ISCAS), IEEE International Symposium on*, May 2015, pp. 1214–1217, <https://dx.doi.org/10.1109/ISCAS.2015.7168858>.
- [150] X. Yu, J.-S. Lee, C. Shu, and S.-G. Lee, “A  $53 \mu W$  Super-regenerative Receiver for 2.4 GHz Wake-up Application”, *Asia-Pacific Microwave Conference*, Dec 2008, pp. 1–4, <https://dx.doi.org/10.1109/APMC.2008.4958320>.
- [151] P. Jean-François, B. Jean-Jules, and S. Yvon, “Modeling, design and implementation of a low-power FPGA based asynchronous wake-up receiver for wireless applications”, *Analog Integrated Circuits and Signal Processing*, vol. 77, no. 2, pp. 169–182, 2013, <https://dx.doi.org/10.1007/s10470-013-0139-2>.
- [152] C. Bryant and H. Sjoland, “A 2.45 GHz,  $50 \mu W$  wake-up receiver frontend with -88 dBm sensitivity and 250 kbps data rate”, *European Solid State Circuits Conference (ESSCIRC)*, 40th, Sept 2014, pp. 235–238, <https://dx.doi.org/10.1109/ESSCIRC.2014.6942065>.
- [153] H. Milosiu, F. Oehler, M. Eppel, D. Fruehsorger, and T. Thoenes, “A  $7 \mu W$  2.4-GHz wake-up receiver with -80 dBm sensitivity and high cochannel interferer tolerance”, *Wireless Sensors and Sensor Networks (WiSNet), IEEE Topical Conference on*. IEEE, Jan 2015, pp. 35–37, <https://dx.doi.org/10.1109/WISNET.2015.7127409>.
- [154] E. Nilsson and C. Svensson, “Ultra Low Power Wake-Up Radio Using Envelope Detector and Transmission Line Voltage Transformer” *IEEE Journal on Emerging and Selected Topics in Circuits and Systems*, vol. 3, no. 1, pp. 5–12, March 2013, <https://dx.doi.org/10.1109/JETCAS.2013.2242777>.
- [155] J. Lim, H. Cho, K. Cho, and T. Park, “High Sensitive RF-DC Rectifier and Ultra Low Power DC Sensing Circuit for Waking up Wireless System”, *Asia Pacific Microwave Conference*, Dec 2009, pp. 237–240, <https://dx.doi.org/10.1109/APMC.2009.5385395>.

- [156] M. S. Durante and S. Mahlknecht, “*An Ultra Low Power Wakeup Receiver for Wireless Sensor Nodes*”, Sensor Technologies and Applications, (SENSORCOMM '09). Third International Conference on, 2009, pp. 167–170, <https://dx.doi.org/10.1109/SENSORCOMM.2009.34>
- [157] M. Malinowski, M. Moskwa, M. Feldmeier, M. Laibowitz, and J. A. Paradiso, “*CargoNet: A Low-cost Micropower Sensor Node Exploiting Quasi-passive Wakeup for Adaptive Asynchronous Monitoring of Exceptional Events*”, Proceedings of the 5th International Conference on Embedded Networked Sensor Systems (SenSys). New York, NY, USA: ACM, 2007, pp. 145–159, <https://dx.doi.org/10.1145/1322263.1322278>.
- [158] S. Bdiri and D. Faouzi, “*An Ultra-Low Power Wake-Up Receiver for Real-time Constrained Wireless Sensor Networks*”, AMA Conferences, May 2015, pp. 612–617, <https://dx.doi.org/10.1109/SENSORCOMM.2009.34>.
- [159] Y. Ammar, S. Bdiri, and F. Derbel, “*An Ultra-low Power Wake up Receiver with Flip Flops Based Address Decoder*”, Systems, Signals & Devices (SSD), 12th International Multi-Conference on. IEEE, 2015, pp. 1–5, <https://dx.doi.org/10.1109/SSD.2015.7348127>.
- [160] D. Masotti, A. Costanzo, P. Francia, M. Filippi, and A. Romani, “*A load-modulated rectifier for RF micropower harvesting with startup strategies*”, IEEE Trans. Microw. Theory Tech., vol. 62, no. 4, pp. 994–1004, Apr. 2014, <https://dx.doi.org/10.1109/TMTT.2014.2304703>.
- [161] S. Gollakota, M. S. Reynolds, J. R. Smith, and D. J. Wetherall, “*The emergence of RF-powered computing*”, Computer, vol. 47, no. 1, pp. 32–39, Jan. 2014, <https://dx.doi.org/10.1109/MC.2013.404>.
- [162] F. Guidi, N. Decarli, S. Bartoletti, A. Conti, and D. Dardari, “*Detection of multiple tags based on impulsive backscattered signals*”, IEEE Trans. Commun., vol. 62, no. 11, pp. 3918–3930, Nov. 2014, <https://dx.doi.org/10.1109/TCOMM.2014.2363118>.
- [163] G. Papotto, F. Carrara, and G. Palmisano, “*A 90-nm CMOS threshold compensated RF energy harvester*”, IEEE J. Solid-State Circuits, vol. 46, no. 9, pp. 1985–1997, Sep. 2011, <https://dx.doi.org/10.1109/JSSC.2011.2157010>.
- [164] M. Stoopman, S. Keyrouz, H. J. Visser, K. Philips, and W. A. Serdijin, “*A self-calibrating RF energy harvester generating 1V at -26.3 dBm*”, Proc. Symp. VLSI Circuits (VLSIC), Kyoto, Japan, 2013, pp. C226–C227.

- [165] S. Oh and D. D. Wentzloff, “A  $-32\text{dBm}$  sensitivity RF power harvester in  $130\text{nm}$  CMOS”, Proc. IEEE Radio Freq. Integr. Circuits Symp., Montreal, QC, Canada, 2012, pp. 483–486. <https://dx.doi.org/10.1109/RFIC.2012.6242327>.
- [166] M. Dini, A. Romani, M. Filippi, and M. Tartagni, “A nanocurrent power management IC for low-voltage energy harvesting sources”, IEEE Trans. Power Electron., vol. 31, no. 6, pp. 4292–4304, Jun. 2016, <https://dx.doi.org/10.1109/TPEL.2015.2472480>.
- [167] A. Ballo, A. Grasso and G. Palumbo, “A Review of Charge Pump Topologies for the Power Management of IoT Nodes”, Electronics 8(5), 2019, <https://dx.doi.org/10.3390/electronics8050480>.
- [168] W. Jung et al., “An ultra-low power fully integrated energy harvester based on self-oscillating switched-capacitor voltage doubler”, IEEE J. Solid-State Circuits, vol. 49, no. 12, pp. 2800–2811, Dec. 2014, <https://dx.doi.org/10.1109/JSSC.2014.2346788>.
- [169] L. Intaschi, P. Bruschi, G. Iannaccone, and F. Dalena, “A  $220\text{-mV}$  input,  $8.6$  step-up voltage conversion ratio,  $10.45\text{-}\mu\text{W}$  output power, fully integrated switched-capacitor converter for energy harvesting”, Proc. IEEE Custom Integr. Circuits Conf. (CICC), Austin, TX, USA, 2017, pp. 1–4, <https://dx.doi.org/10.1109/CICC.2017.7993623>.
- [170] A. Romani, M. Filippi and M. Tartagni, “Micropower Design of a Fully Autonomous Energy Harvesting Circuit for Arrays of Piezoelectric Transducers”, IEEE Transactions on Power Electronics, vol. 29, no. 2, pp. 729–739, Feb. 2014, <https://dx.doi.org/10.1109/TPEL.2013.2257856>.
- [171] M. Dini, A. Romani, M. Filippi, V. Bottarel, G. Ricotti and M. Tartagni, “A Nanocurrent Power Management IC for Multiple Heterogeneous Energy Harvesting Sources”, IEEE Transactions on Power Electronics, vol. 30, no. 10, pp. 5665–5680, Oct. 2015, <https://dx.doi.org/10.1109/TPEL.2014.2379622>.
- [172] G. Zamora-Mejía, J. Martinez-Castillo, J. M. Rocha-Pérez, and A. Díaz-Sánchez, “A digitally enhanced LDO voltage regulator for UHF RFID passive tags”, IEICE Electron. Exp., vol. 13, no. 12, 2016, Art. no. 20150989, <https://dx.doi.org/10.1587/elex.13.20150989>.
- [173] G. K. Balachandran and R. E. Barnett, “A  $110\text{ nA}$  voltage regulator system with dynamic bandwidth boosting for RFID systems”, IEEE J. Solid-State Circuits, vol. 41, no. 9, pp. 2019–2028, Sep. 2006, <https://dx.doi.org/10.1109/JSSC.2006.881015>.

- [174] G. De Vita and G. Iannaccone, “Ultra-low-power series voltage regulator for passive RFID transponders with subthreshold logic” *Electron. Lett.*, vol. 42, no. 23, pp. 1350–1351, Nov. 2006, <https://dx.doi.org/10.1049/el:20062080>.
- [175] ECSEL Joint Undertaking, Horizon 2020 CONNECT Project, <https://www.ecsel.eu/projects/connect>.
- [176] Convergence (ERA-NET) Project, <https://convergence-era.org/>.
- [177] Microchip, “AN1631: Simple Link Budget Estimation and Performance Measurements of Microchip Sub-GHz Radio Modules”, 2013, <http://ww1.microchip.com/downloads/en/Appnotes/00001631A.pdf>.
- [178] M. Fantuzzi, D. Masotti and A. Costanzo, “Rectenna Array with RF-Uncoupled Closely-spaced Monopoles for Autonomous Localization”, 2018 48th European Microwave Conference (EuMC), Madrid, 2018, pp. 765–768, <https://dx.doi.org/10.23919/EuMC.2018.8541716>.
- [179] A. Costanzo and D. Masotti, “Energizing 5G: Near- and far-field wireless energy and data transfer as an enabling technology for the 5G IoT”, *IEEE Microwave Magazine*, vol. 18, no. 3, pp. 125–136, May 2017, <https://dx.doi.org/10.1109/MMM.2017.2664001>.
- [180] D. Fabbri, A. Romani, A. Costanzo and D. Masotti, “An orientation-independent UHF battery-less Tag for extended-range Applications”, *URSI GASS 2020*, Rome, Italy, 29 August - 5 September 2020, <https://dx.doi.org/10.23919/URSIGASS49373.2020.9231982>.
- [181] Wireless Identification Sensing Platform (WISP) Project repository [Online], <http://www.wispsensor.net>.
- [182] P. V. Nikitin and V. S. Rao, “Antennas and Propagation in UHF RFID Systems”, *IEEE International Conference on RFID*, Las Vegas, NV, USA, May 2008, <https://dx.doi.org/10.1109/RFID.2008.4519368>
- [183] Dardari D.; Feuillen T.; Raucy C.; Vandendorpe L.; Craeye C.; Decarli N.; Fabbri D.; Guerra A.; Fantuzzi M.; Masotti D.; Costanzo A.; Romani A.; Drouguet M., “An ultra-wideband battery-less positioning system for space applications”, *IEEE International Conference on RFID Technology and Applications (RFID-TA)*, Pisa, Italy, 2019, pp. 104–109, <https://dx.doi.org/10.1109/RFID-TA.2019.8892114>
- [184] D. Dardari, N. Decarli, A. Guerra, M. Fantuzzi, D. Masotti, A. Costanzo, D. Fabbri, A. Romani, M. Drouguet, T. Feuillen, C. Raucy, L. Vandendorpe and C.

- Craeye, "*An Ultra-low Power Ultra-wide Bandwidth Positioning System*", IEEE JOURNAL OF RADIO FREQUENCY IDENTIFICATION, 2020, <https://dx.doi.org/10.1109/JRFID.2020.3008200>.
- [185] LOST Project demonstration, ESA-ESTEC Planetary Robotics Laboratory, Noordwijk (Holland), <https://youtu.be/iLLhID7Q08k>.
- [186] D. Fabbri, N. Decarli, A. Guerra, A. Romani and D. Dardari, "*High-accuracy positioning of battery-less hybrid Gen2 UHF-UWB tags*", Asilomar Signals, Systems and Computer Conference, 2020, [Accepted]